

國 立 交 通 大 學

材 料 科 學 與 工 程 學 系

博 士 論 文

新穎記憶體及生物感測器元件結構設計、製造與
應用

**Design, Fabrication and Application of the Flash
Memory and Biosensing Devices Based on
Nanotechnology**

研究生：吳其昌

Chi-Chang Wu

學號： 9418837

指導教授：柯富祥 博士

Dr. Fu-Hsiang Ko

中 華 民 國 九 十 八 年 十 月

國 立 交 通 大 學

材 料 科 學 與 工 程 學 系

博 士 論 文

新穎記憶體及生物感測器元件結構設計、製造與

應用

**Design, Fabrication and Application of the Flash
Memory and Biosensing Devices Based on
Nanotechnology**



研究生：吳其昌

Chi-Chang Wu

學號： 9418837

指導教授：柯富祥 博士

Dr. Fu-Hsiang Ko

中 華 民 國 九 十 八 年 十 月

新穎記憶體及生物感測器元件結構設計、製造與
應用

**Design, Fabrication and Application of the Flash
Memory and Biosensing Devices Based on
Nanotechnology**

研究生：吳其昌

Chi-Chang Wu

指導教授：柯富祥 博士

Dr. Fu-Hsiang Ko



A Dissertation

Submitted to

Department of Materials Science and Engineering

College of Engineering

National Chiao Tung University

in Partial Fulfillment of the Requirements

for the Degree of

Doctor of Philosophy in

Materials Science and Engineering

October 2009

Hsinchu, Taiwan, Republic of China

中華民國九十八年十月

新穎記憶體及生物感測器元件結構設計、製造與應用

學生：吳其昌

指導教授：柯富祥 教授

國立交通大學 材料科學與工程學系博士班

摘要

奈米科技的發展對於現代的科學、工業、甚至是我們的生活都是一項重要的改革。由於尺寸的微小化，使得物質的物理、化學、及生物特性都與原本相異。本論文係以奈米的技術與材料應用在現今的電子及生物領域，期望能夠讓不同領域的結合迸出火花。本論文分為三個部分，我們將其內容摘要說明如後。

第一部分我們探討矽化鎳薄膜於接面二極體的製程改善。由於電子元件的縮小已達奈米尺度，金屬-半導體接面的工程更形重要。我們研究不同的金屬覆蓋層於矽化鎳薄膜上對於接面二極體的電氣特性影響。我們發現無覆蓋及氮化鈦覆蓋的元件比鈦覆蓋的特性較好，這是由於在鈦覆蓋的樣品中會生成一高阻值的鎳-鈦-矽化合物，而影響元件特性。我們也研究矽化鎳在矽鍺上的熱穩定性。我們發現使用矽/矽鍺堆疊結構會改善矽化鎳薄膜的熱穩定性。另外，矽化鎳於奈米尺度的矽鍺線上會有所謂的窄線效應，但若是在矽/矽鍺堆疊結構的奈米線上則相對穩定。此結果歸因於矽/矽鍺疊層結構的應力作用限制矽化鎳的晶粒成長而延緩其退化。

本論文第二部分探討以溶膠-凝膠法成長奈米微晶粒的機制。我們研究不同的回火溫度對於形成奈米微晶粒的影響。我們發現薄膜於600 °C開始形成島狀，並在900 °C完全轉換成微晶粒。我們提出一個模型來解釋此轉變機制。我們並將奈米微晶粒應用於快閃記憶體的載子補陷層，成功的製作出特性良好的記憶體，

其在125 °C、10⁶秒的資料保存力其電荷流失可以小於30%。另外，我們也研究溶劑對於形成奈米微晶粒的影響。我們發現以乙醇為溶劑所形成的奈米微晶粒為分離狀，而以異丙醇為溶劑則為連續狀。此原因歸咎為以乙醇為溶劑所旋轉塗佈而形成的薄膜較薄，此現象有助於形成分離狀的奈米微晶粒。以乙醇系統形成的奈米微晶粒記憶體其記憶視窗比異丙醇系統來的要大，且其資料保存力也較好。我們並製作出一鈦-鋯-矽-氧的化合物奈米微晶粒記憶體，並以新穎的熱電洞作為寫入方式。此記憶體具有4.3伏的記憶視窗、高的資料保存力等特色。此優異的特性歸因於高密度的奈米微晶粒與深井缺陷，因此不會有嚴重的橫向與縱向漏電流。

最後，我們探討以奈米線/奈米帶場效電晶體作為生物分子的感測元件。我們發展一矽奈米線場效電晶體來偵測與癌症相關的 BRAF^{V599E} 變異基因。我們發現當變異基因接到晶片上時，此奈米線場效電晶體的啟始電壓會變大，而當變異基因脫離時，啟始電壓又會回復到原來的地方。此感測元件也具有分辨一個及五個錯配基因的能力。我們更利用了局部氧化的技術製作一矽奈米帶場效電晶體，並用它來早期偵測肝癌相關的生物記號。此技術的優點是完全相容於互補式金氧半場效電晶體製程，同時又可避免使用較為昂貴的微影設備。為了增加肝癌偵測的精確性及避免假陽性問題，我們分別偵測了甲型胎兒蛋白的抗原、B型肝炎的 DNA 片段及溶液的酸鹼值-這些都可以當作肝癌偵測的指標。結合微流道系統，我們的奈米帶感測器可以即時、免標定以及高靈敏度的偵測這三種生物指標，或許未來可作為肝癌的早期偵測工具。

Design, Fabrication and Application of the Flash Memory and Biosensing Devices Based on Nanotechnology

Student: Chi-Chang Wu

Advisor: Prof. Fu-Hsiang Ko

Department of Materials Science and Engineering
National Chiao Tung University

Abstract

The development of nanotechnology is an important revolution to science, industry, and even our life. Because of size-miniaturization, the physical, chemical, and biological properties of the materials are apparently different to original ones. In this thesis, nano-technology and nano-materials are applied to the electronic and biology fields. This thesis is divided into three sections, and is described below briefly.

In the first section, the improvement of nickel silicide on the junction diode was demonstrated. Because the device continues to shrink to nano size, the issue about metal-semiconductor interface becomes more and more important. The effects of capping layers on formation and electrical properties of Ni-silicided junctions were investigated. The uncapped and TiN-capped samples were shown to exhibit better thermal stability than the Ti-capped samples. A high-resistivity $\text{Ni}_x\text{Ti}_y\text{Si}_z$ compound layer is formed on the surface during silicidation for the Ti-capped sample. In addition, the thermal and morphological stability of NiSi on SiGe film was also investigated. We found that NiSi films formed on poly-Si/poly-SiGe stack layers possessed

continuous, smooth structures. Moreover, nickel germanosilicide [Ni(Si,Ge)] line formed on the poly-SiGe exhibited a fine-line effect, whereas NiSi line formed on the poly-Si/poly-SiGe stack layer was very stable. A model for the stress-confined grain growth and recrystallization is proposed to explain the improved properties of the poly-Si-buffered film.

In the second section, the formation of nanocrystal by using sol-gel spin-coating method was studied. The formation of the nanocrystals at various annealing temperatures was demonstrated. We found the film started to form the islands at 600 °C anneal, and finally transferred into NCs at 900 °C. A model was proposed to explain the transformation of thin film. The retention for 900 °C annealed nanocrystal memory exhibited less than 30% charge loss after 10^6 sec at 125 °C measurement. The solvent effect on the formation of nanocrystal was also investigated. The morphology of the nanocrystals for precursors in ethanol system was isolated type, while was interconnected form in IPA system. Ethanol as preparation solvent formed a thinner sol-gel film for spinodal decomposition, and was benefit for formation of isolated nanocrystals. The ethanol system derived NC memory demonstrated a large memory window (9.8 V) than IPA system (3.8 V) due to the isolated NCs. The ethanol system derived NC memory also exhibited better memory performance of retention times for < 5% and < 10% charge loss at 25 °C and 85 °C measurement, respectively. Moreover, a $Ti_xZr_ySi_zO$ nanocrystal memory was operated by a novel hot hole trapping method. The memory window of the nanocrystal memory by hot hole trapping can be up to 4.3 V; long retention times are extrapolated up to 10^6 sec with about 8%, 11%, and 25% charge loss at 25, 85, and 125 °C measurement, respectively. The good electrical performance is attributed to the effects of the high-density isolated nanocrystals and hole-trapped into the deep trap energy level, hence no significant lateral and vertical charge leakage occurs.

Finally, high-sensitivity nanowire/nanobelt field effect transistor (FET) was fabricated and for biosensing application. We developed a silicon nanowire FET that allows deoxyribonucleic acid (DNA) biosensing. We employed the BRAF^{V599E} mutation gene, which correlates to the occurrence of cancers, as the target DNA sequence. The threshold voltage of the NWFET increased when the mutation gene was hybridized with the capture DNA strands on the nanowire, and decreased to the original level after de-hybridization of the gene. The detection results of mismatched DNA sequences, including one- and five-base-mismatched DNA strands, could be distinguished from complementary DNA gene by this sensor. Furthermore, we used the local oxidation of silicon (LOCOS) process to fabricate a silicon nanobelt field effect transistor (NB FET). This approach is completely compatible with complementary metal oxide semiconductor (CMOS) technology, yet it avoids the need for expensive lithography tools to define the nanoscale pattern. We employed the fabricated NB FET as a biomolecular sensor for the early, real-time, label-free screening of hepatocellular carcinoma (HCC). To increase the accuracy of HCC screening and prevent false positive identification, we tested the ability of our NB FET to determine alpha-fetoprotein (AFP) as a cancer marker, a DNA fragment from hepatitis B virus (HBV), and the solution pH—all of which can be used as markers for the onset of HCC. This multiplex sensing of AFP, HBV, and the solution pH suggests that our direct, label-free, ultrasensitive biosensor in a microfluidic chip might be applicable as an HCC detector in real samples.

致 謝

本論文能夠順利完成首先要感謝我的指導教授柯富祥博士，除了專業知識與研究精神所給我的殷殷指導之外，其平時的言教與身教也讓我獲益良多，更是我努力學習的好榜樣。在待人處事上面，柯教授是一位完全沒有架子的人，和柯教授的相處沒有任何壓力；而在學術研究上，柯教授深思遠慮及精益求精的態度，卻又讓人欽佩不已。今雖即將畢業，深感尚有許多需向柯教授學習之處，在此亦致上無限的感激。

另外也要感謝實驗室各位伙伴的打拼與幫忙。感謝銘清、品麟和貞志熬夜陪我共度許多通宵的實驗；感謝依臻化學方面的幫忙與努力；感謝奕儂、德玲、柏軒與丁香給我在生物知識的諸多建議與討論。當然也要謝謝實驗室其他在不同領域中共同努力過及患難與共的夥伴們：俊淇、佳典、中書、志威、建文、敬雅、志杰、群芳、美榕，因為有你們，讓我的學生生活平添了許多色彩。

感謝游信強博士與謝明山博士在我研究遇到瓶頸與苦悶的時候，給我及時的開導與建議，讓我閉塞的心豁然開朗。感謝李政則博士給我的一些人生及研究上的建議。感謝國家奈米元件實驗室的各位工程師們給我實驗上的幫助及建議，讓我能夠順利的進行研究。感謝俊淇、旭君及鶯玲在我們的午餐會報中聽我訴苦。感謝淑芬、嘉琳、佩玲在行政事務上給我的幫助。

感謝潘扶民教授、韋光華教授、楊裕雄教授、楊文祿教授、潘同明教授、劉福鯤教授及吳劍侯教授在百忙之中參加我的論文口試，並給予我許多珍貴的意見及論文上的指導，使我的論文能夠更完整而嚴謹。

四年的博士班研究生生活有苦有甜，點點滴滴在心頭。我要特別感謝我的妻子-蕙茹，這些年來給我的包容與體諒，讓我能心無旁騖的專注在我的研究上面，沒有你的支持，這本論文肯定無法如期完成。也要謝謝蕙茹幫我生下可愛的兒子-祥輔，讓我們的家及人生有了更多的色彩。

最後僅將此論文獻給我在天之靈的父親，雖然您無法親眼目睹，但我相信您在天上也會感到與有榮焉。

謹以此文感謝你們的幫忙，並祝你們順心如意。

Contents

Abstract (Chinese)	I
Abstract (English)	III
Acknowledgments	VI
Contents	VII
Figure captions and Table lists	X
Chapter 1: Introduction	001
1.1 Introduction to nanotechnology.....	001
1.2 Motivation.....	006
1.3 Thesis organization.....	012
Chapter 2: Research on nickel silicide process	022
2.1 Introduction.....	022
2.2 Study on the capping layer for the formation of nickel silicide junctions.....	023
2.2.1 Experiments.....	024
2.2.2 Results and discussion.....	025
2.3 Study on morphological stability of the nickel silicide formed on polycrystalline Si/SiGe substrate.....	029
2.3.1 Experiments.....	030
2.3.2 Results and discussion.....	031
2.4 Summary.....	034
Chapter 3: Study on the sol-gel derived nanocrystal memories	047
3.1 Introduction.....	047
3.2 Effect of annealing temperature for the formation of nanocrystals.....	050
3.2.1 Experiments.....	051
3.2.2 Results and discussion.....	052
3.3 Effect of solvent for the formation of nanocrystals.....	056

3.3.1 Experiments.....	058
3.3.2 Results and discussion.....	060
3.4 Hot hole trapping characteristic of the Ti-based nanocrystal memory.....	064
3.4.1 Experiments.....	065
3.4.2 Results and discussion.....	066
3.5 Summary.....	069
Chapter 4: Research on the real-time, label-free and ultrasensitive nanowire and nanobelt FET biosensors for cancer marker analysis.....	096
4.1 Introduction.....	096
4.2 A silicon NWFET biosensor to detect a gene mutation.....	099
4.2.1 Fabrication of NWFET Sensors.....	100
4.2.2 Self-assembly of capture DNA on the NWFET device.....	101
4.2.3 Target DNA hybridization and de-hybridization.....	104
4.2.4 Electrical performance of the NWFET.....	105
4.2.5 Evaluating of cleaning efficiency through fluorescence imaging.....	106
4.2.6 Using the NWFET to detect a mutated gene.....	108
4.3 A novel silicon NB FET for hepatocellular carcinoma detection.....	111
4.3.1 NB FET fabrication.....	114
4.3.2 Surface modification of the NB FET.....	116
4.3.3 AFP antibody and antigen modification.....	117
4.3.4 Preparation and detection of mice serum.....	118
4.3.5 Modification of HBV DNA probe.....	119
4.3.6 Preparation of the hydrogen ion solution.....	121
4.3.7 Nanobelts images.....	121
4.3.8 Electrical properties of the NB FET.....	122
4.3.9 AFP detection response by the NB FET.....	124

4.3.10 AFP detection from mice serum.....	127
4.3.11 HBV x gene detection by the NB FET.....	128
4.3.12 Solution pH analysis by the NB FET.....	130
4.4 Summary.....	132
Chapter 5: Conclusions and future perspective.....	162
5.1 Conclusions.....	162
5.2 Future perspective.....	164
References.....	165



Figure captions

Chapter 1

- Fig. 1.1 (a) Conventional photolithography procedure. This procedure separates into two steps, step 1 is the preparation of the mask, and step 2 is the application of the mask to manufacture replicas. (b) Typical bulk-/ film-machining method, the channel is created by etching trenches in the substrate wafer or, alternatively, in the film deposited on the substrate.....015
- Fig. 1.2 Schematic diagram of the bottom-up procedure. A chemical reaction brings together some molecular aggregate to small crystal, and the small crystals attract surroundings into a nano-particle.....016
- Fig. 1.3 Schematic representations of the contact resistance in nano-device. (a) The contact resistance is increased dramatically due to the contact area is reducing without nickel silicide, while (b) the contact resistance remain constant using nickel silicide as the contact metal.....017
- Fig. 1.4 Schematic representations of the contact resistance in shrinkage and mis-alignment problem. (a) contact hole size shrinking, and (b) contact hole mis-alignment.....018
- Fig. 1.5 Typical layout of the device. (a) without silicide process, and (b) with silicide process.....019
- Fig. 1.6 Evolution of the non-volatile memory.....020

Chapter 2

- Fig. 2.1 Sheet resistance of NiSi using different capping layer processes as a function of annealing temperature.....036
- Fig. 2.2 XRD spectra of (a) uncapped, (b) Ti 10-capped, (c) Ti 30-capped, and (d) TiN 30-capped samples after annealing at 400-700°C for 30 sec.....037
- Fig. 2.3 Cross-sectional TEM images of (a) uncapped, (b) TiN 30-capped, (c) Ti 5-capped, (d) Ti 10-capped, (e) Ti 20-capped, and (f) Ti 30-capped samples after annealing at 650°C for 30 sec.....038
- Fig. 2.4 EDX spectra of (a) the upper layer and (b) the lower layer formed on the Ti 30-capped sample.....039
- Fig. 2.5 Cumulative distribution of reverse-biased leakage current densities for the Ni-silicided n^+ -p junction diodes annealed at 500°C for 30 sec.....040
- Fig. 2.6 SIMS depth profiles of As^+ for samples annealed at 500°C for 30 sec.....041

Fig. 2.7 Sheet resistances of the nickel (germano)silicide films formed on poly-Si (sample (i)), poly-SiGe (sample (ii)), and poly-Si/poly-SiGe stack layers (sample (iii)) as a function of the annealing temperature.....	042
Fig. 2.8 Sheet resistances of the nickel (germano)silicide lines annealed at 600 °C as a function of the line width.....	043
Fig. 2.9 Cross-sectional TEM micrographs of the nickel (germano)silicide films formed on (a) poly-Si (sample (i)), (b) poly-SiGe (sample (ii)), and (c) poly-Si/poly-SiGe stack layers (sample (iii)) after annealing at 850 °C...	044
Fig. 2.10 Schematic representations of silicide agglomeration process.....	045
Fig. 2.11 Schematic models of nickel (germano)silicide formation at high annealing temperature: (a) on poly-Si (sample (i)) and poly-SiGe (sample (ii)); (b) on poly-Si/poly-SiGe stack layers (sample (iii)).....	046

Chapter 3

Fig. 3.1 Cross-sectional TEM micrographs of the thin film transformation after (a) 400 °C, (b) 600 °C, and (c) 900 °C annealing.....	071
Fig. 3.2 EDS spectra of the sol-gel derived nanocrystals.....	072
Fig 3.3 (a) Si 2 <i>p</i> , (b) Zr 3 <i>d</i> , (c) Hf 4 <i>f</i> , and (d) O 1 <i>s</i> XPS spectra of the sol-gel thin films after different annealing temperatures.....	073-074
Fig. 3.4 Interfacial tension of the sol-gel thin film as a function of annealing temperature.....	075
Fig. 3.5 Transformation processes of the sol-gel thin film into NC after different annealing temperatures.....	076
Fig 3.6 Retention characteristics of the NC memories annealed at (a) 600 and (b) 900 °C at measurement temperatures of 25, 85, and 125 °C. Inset of Fig. 4(b): the I_d-V_g curves of the NC memory in the programmed/erased state.....	077
Fig. 3.7 Disturbance characteristics of the 900°C annealed NC memory. (a) Drain disturbance, (b) Gate disturbance, and (c) Read disturbance.....	078
Fig. 3.8 Schematic diagram of the NC memory at 2-bit operation.....	079
Fig 3.9 Electrical characteristic of the NC memory at 2-bit operation.....	080
Fig. 3.10 Schematic diagram of the device structure for the spin coating charge trapping film/nanocrystal memories.....	082
Fig. 3.11 (a) The pseudo-binary ZrO_2-SiO_2 phase diagram. (b) The metastable extensions of the liquid miscibility gap and spinodals to lower temperatures in ZrO_2-SiO_2	083
Fig. 3.12 Cross-sectional TEM images for the morphology from (a) ethanol system (inset: lattice fringe of nanocrystal), and (b) IPA system.....	084

Fig. 3.13 Phase separation mechanism of the sol-gel-derived film from (a) ethanol system, and (b) IPA system.....	085-086
Fig. 3.14 I_D - V_G characteristics of the NC memories in (a) ethanol system, and (b) IPA system at flash, program, and erase state, respectively.....	087
Fig. 3.15 Charge retention characteristics of the NC memories in (a) ethanol system, and (b) IPA system at measurement temperatures of 25 and 85°C.....	088
Fig. 3.16 Endurance characteristics of the NC memories in ethanol and IPA system, respectively. The measured condition for programming is: $V_G = 10$ V, $V_D = 10$ V, 10 ms, and erasing is: $V_G = -6$ V, $V_D = 10$ V, 10 ms.....	089
Fig. 3.17 Plan-view TEM image of the sol-gel derived NC.....	090
Fig. 3.18 (a) Si 2 <i>p</i> , (b) Zr 3 <i>d</i> , (c) Hf 4 <i>f</i> , and (d) O 1 <i>s</i> XPS spectra of the sol-gel derived $Ti_xZr_ySi_zO$ nanocrystals.....	091
Fig. 3.19 I_D - V_g characteristics of the NC memory at flash, program, and erase state, respectively.....	092
Fig. 3.20 (a) Retention characteristics of the NC memories at measurement temperatures of 25, 85, and 125 °C. (b) Endurance characteristic of the nanocrystal memory device.....	093
Fig. 3.21 (a) Program and (b) erase characteristics of the nanocrystal memory device under different conditions.....	094
Fig. 3.22 Inferential energy band diagram of the sol-gel derived $Ti_xZr_ySi_zO$ NC memory under thermal-equilibrium.....	095

Chapter 4

Fig. 4.1 Schematic representation for the fabrication of the NWFET sensors. (a) A 6-in. SOI wafer (50 nm intrinsic Si; 150 nm buried oxide) was employed as the device substrate. (b) NWs were patterned using an e-beam direct writing and dry etching system. (c) Source/drain implantation and annealing. (d) Contact pad (500 nm Al-Si-Cu film) was deposited at the source/drain region. (e) Passivation layer formed, followed by etching back the detection region for DNA immobilization (red circle). (f) Cross-sectional representation of the completed NWFET sensor and its electrical connection for the detection of DNA strands.....	134
Fig. 4.2 Self-assembly processes for the immobilization of capture DNA and hybridization of target DNA. (1) The Si NW presenting a native oxide on its surface was coated with APTES. (2) Glutaraldehyde was linked to the amino groups. (3) Terminal 3'-amino groups of the capture DNA strands were reacted with the aldehyde groups. (4) Complementary target DNA was hybridized to the capture DNA on the Si NW surface.....	135

Fig. 4.3 Plots of drain current versus gate voltage for the NWFET sensor, measured at values of V_D of 0.1 (black line) and 1 V (red dotted line). Inset: Scanning electron microscopy image of the 60 nm-wide Si NW.....	136
Fig. 4.4 (a) Schematic representation of the SiO_2 line structure used to test the immobilization efficiency. The underlying Si_3N_4 film was used to define the selectivity, because of the higher DNA immobilization efficiency of SiO_2 relative to that of the Si_3N_4 surface. (b) Fluorescence images of the (I) uncleaned (control) sample and (II–V) the samples cleaned with (II) DI, (III) piranha, (IV) IPA, and (V) ACE.....	137
Fig. 4.5 Electrical responses of the NWFET sensor with capture DNA immobilized after using various cleaning methods. The I_D – V_G curves were recorded at a constant drain voltage ($V_D = 0.1$ V). The base line curve was recorded for the sample prior to cleaning but after treatment with PBS (black line). Curves were recorded for the DNA-immobilized NWFET sensors after washing with DI (green dotted line), IPA (gray dotted line), and ACE (blue dotted line). The curve recorded for the sample after ACE cleaning but without DNA immobilization (red dotted line) was recorded to confirm the influence of the cleaning process.....	138
Fig. 4.6 Concentration-dependent electrical response of the capture DNA–modified NWFET sensor when detecting target DNA. The I_D – V_G curve of the base line was obtained in PBS buffer (black line); PBS buffer solutions containing target DNA at various concentrations (10 fM, 1 pM, 100 pM, 10 nM) were injected, respectively, and the I_D – V_G curves recorded. The de-hybridized samples were obtained after treatment of the dsDNA with hot DI water (90 °C); the I_D – V_G curves were then measured (red dotted line). Inset (I): Fluorescence image of 10 nM FITC-labeled target DNA bound to the capture DNA. Inset (II): Fluorescence image of the FITC-labeled target DNA after de-hybridization.....	139
Fig. 4.7 Voltage shift (from $n=4$) of the NWFET sensor plotted with respect to the target DNA concentration. The voltage shift was extracted from Figure 5(a) at a constant drain current ($I_D = 1$ nA).....	140
Fig. 4.8 Electrical response of the capture DNA–modified NWFET sensor when detecting mismatched target DNA. The I_D – V_G curve of the base line was recorded in PBS buffer (black line); PBS buffer solution containing one- or five-base–mismatched target DNA strands (10 nM) was injected and the I_D – V_G curves were recorded.....	141
Fig. 4.9 Schematic representation of the NB FET fabrication process.....	142
Fig. 4.10 Fabrication of the silicon nanobelt. (a, b) Schematic representations of the structures (a) before and (b) after performing the LOCOS process.....	143

Fig. 4.11 Cross-sectional TEM images of the nanobelt after performing (a) 150 and (b) 240 nm-thick oxidation steps, respectively. (c) Cross-sectional SEM image of the nanowire after improved LOCOS process.....	144-145
Fig. 4.12 Schematic representation of the NB surface modification process.....	146
Fig. 4.13 Schematic representation of AFP antibody and antigen modification process.....	147
Fig. 4.14 Electrical response of PBS injected into the detection region of the NB FET sensor.....	148
Fig. 4.15 Schematic representation of the DNA modification process.....	149
Fig. 4.16 Cross-sectional TEM image of the nanobelt. Inset: enlarged TEM image of the nanobelt to show its thickness.....	150
Fig. 4.17 Schematic representation of the microfluidic holder.....	151
Fig. 4.18 Schematic representation of completed NB FET sensor with microfluidic channel.....	152
Fig. 4.19 Electrical performance of the NB FET. (a) I_D - V_G dependence for $V_D = 0.5$ (red) and 1 V (blue). Inset: Subthreshold swing in the subthreshold regime. (b) I_D - V_D for varying V_G (-2 to +5 V; $\Delta V = 1$ V).....	153
Fig. 4.20 Electrical properties of the NB FET sensors. (a) I_D - V_G curve and transconductance of the NB FET sensor. (b) Detection responses of the NB FET, biased at $g_{m,max}$, toward various AFP concentrations. (c) I_D - V_G curves of the NB FET before and after injection of 500 pg/mL AFP.....	154-155
Fig. 4.21 (a) Detection response toward AFP concentrations ranging from 3 to 600 ng/mL. (b) Normalized current shift plotted as a function of AFP concentration.....	156
Fig. 4.22 Detection response of AFP concentration from adult and infant mice.....	157
Fig. 4.23 Plot of light absorption with respect to AFP concentration, determined using an ELISA kit.....	158
Fig. 4.24 Electrical response of the NB FET sensor toward a 15-mer DNA fragment from HBV. (a) Detection response toward DNA concentrations ranging from 1 fM to 1 pM. (b) Normalized current shift plotted as a function of DNA concentration; the linear range of calibration curve extended from 10 fM to 1 pM.....	159
Fig. 4.25 Detection responses toward complementary and one-, five-, and 15-base-mismatched target DNA samples.....	160
Fig. 4.26 Electrical response of the NB FET sensor toward the solution pH. (a) Detection response at values of pH ranging from 6.40 to 7.39. (b) Drain current plotted as a function of the pH.....	161

Table captions

Chapter 1

Table 1.1 Comparison of various disease detection and diagnosis methods.....021

Chapter 3

Table 3.1 Dependence of viscosity and film thickness as a function of compositional molar ratio of sol-gel solutions.....081



Chapter 1

Introduction

1.1 Introduction to nanotechnology

There's plenty of room at the bottom! -- A famous lecture given by physicist Richard Feynman, who was awarded the Nobel Prize in physics in 1965, at an American Physical Society meeting at Caltech on December 29, 1959 [1]. Feynman described a process by which the ability to manipulate individual atoms and molecules might be developed, using one set of precise tools to build and operate another proportionally smaller set, and so on down to the needed scale. He was particularly interested in the possibilities of denser computer circuitry, and microscopes which could see things much smaller than is possible with scanning electron microscopes.

Feynman concluded his talk with challenges to build a tiny motor and to write the information from a book page on a surface $1/25,000$ smaller in linear scale. Feynman offered prizes of \$1000 for each challenge. Amazingly, his motor challenge was quickly met by a meticulous craftsman, using conventional tools. In 1985, Tom Newman, a Stanford graduate student, successfully reduced the first paragraph of *A Tale of Two Cities* by $1/25,000$, and collected the second Feynman prize.

After that, the technology is toward smaller thing, and even to nano-size. Owing to this famous talk, Richard Feynman is called the father of nanotechnology. Feynman's "Plenty of room" gave nanotechnology a packaged history that provided an early date of December 1959, plus a connection to the charisma and genius of Richard Feynman.

Nanotechnology is a revolution in science and technology. It distinguishes itself from all previous scientific and industrial revolutions in many ways. Through the new technology, we can not only change the fundamental properties of matter as well as a tailor make materials with desirable attributes, but also manipulate the nanoscale objects that conventional technique is impossible to do. Generally nanotechnology deals with structures of the size 100 nanometers or smaller, and involves developing materials or devices within that size. Nanotechnology is very diverse, ranging from extensions of conventional device physics, to completely new approaches based upon self-assembly method, to developing new materials with dimensions on the nanoscale, even to speculation on whether we can directly control matter on the atomic scale. Nanotechnology has the potential to create many lots materials and devices with applications, such as in electronics, biology, and chemistry field.

A large number of methods for nanofabrication technology have been reported. In general, these methods can be divided into two categories, that is, top-down and

bottom-up approaches [2]. The top-down methods start with patterns that have a large scale, and shrink their lateral dimensions to form nanostructures. In contrast, the bottom-up methods built from atoms or molecules which assemble themselves chemically by principles of molecular recognition. The bottom-up researches attempt to build nano-devices on one molecule at a time, rather like the way that living organisms synthesize macromolecules [3]. The two approaches are described in detail below.

(1) Top-down approach

The top-down approach seeks to fabricate nano-devices by using advanced lithography method. In fact, many technologies that descended from conventional solid-state silicon methods for fabricating microprocessors are now capable of creating features smaller than 100 nm, falling under the definition of nanotechnology.

Similar to the micromachining, top-down approach can be divided into bulk-/film-machining, surface-machining, and mold-machining (Fig. 1-1). In bulk-/film-machining, the pattern is created by etching trenches in the substrate. This is done typically by conventional photolithography followed by etching process of the substrate. [4-5] In surface-machining, a bottom layer is deposited on the substrate followed by the deposition of the sacrificial layer. After patterning, the top layer is deposited on top of the sacrificial layer and then pattern [6]. The nano-pattern is

finally formed by removing the sacrificial layer. In mold-machining, the mold in the inverse shape of the desired pattern is fabricated. This is filled with a structural material and then, the mold can be removed from the desired structure.

The top-down approach is able to fabricate a high-density nanostructure by using the advanced lithography and etching system. The cost is, however, expensive due to these high-priced systems and complex process steps. How to reduce the running cost is an urgent issue in developing nanotechnology.

(2) Bottom-up approach

The bottom-up approach seeks to assemble the atoms or molecules into the smallest nanostructure by controlling the chemical reaction. The typically dimension for this approach is about 2~10 nm. Fig. 1-2 shows the schematic diagram of the bottom-up approach. This approach is cheaper than top-down approach, and hence the cost can be down. However, the controlling of bottom-up approach is still a challenge. Most existing studies based on “bottom-up” nanostructures have been limited by complex integration techniques that require precise transfer and positioning of individual nanostructures to provide reliable and superior ohmic contacts.

Self-assembly is the most used bottom-up approach to fabricated nanostructure. Currently, the mastery of self-assembly is limited to its relatively simple systems. To achieve complex systems hierarchical self-assembly can assist, where the products of

one self-assembly step is a base for the next one. The formation of self-assembled monolayers, that are produced when a substance spontaneously forms a molecular monolayer on a surface, could be successfully combined with standard lithographical methods to achieve large-scale and better controlled structures.

Although the two methods seem to develop by opposite strategy, they are not conflict with each other. In fact, a promising and ideal approach is the combination of both methods, where the smallest nanostructures can be achieved by bottom-up methods and the interconnection can be done by top-down lithographical methods. H.Zhu et al. [7] proposed CNTs grown by chemical vapor deposition (CVD) within the anodic aluminum oxide (AAO) template. Through this method, good uniformity and naturally perpendicular growth can be achieved without the need of extra process step.

1.2 Motivation

In this thesis, nano-technology and nano-materials are applied to the electronic and biology fields. This thesis is divided into three sections, and is described below briefly.

(1) Research on nickel silicide process

Because the device continues to shrink to a nano-size dimension, the issue about metal-semiconductor interface becomes more and more important. The contact resistance increases dramatically due to the contact area of the Source/Drain is decreasing, and hence the driving force of the nano-device is degraded [8]. Through the silicide technique, the contact resistance and layout area can be decreased. Fig. 1-3 shows the dramatic representations of the silicide technique used in the nano-device. Without silicide film, the contact hole is decreased dramatically when the device shrinks, and hence the contact resistance is increases [Fig. 1-3(a)]. On the other hand, the contact resistance of Source/Drain is a constant when device is shrinking by using the silicide technique due to the contact area is almost the same [Fig. 1-3(b)]. Even the situation of contact hole decreasing or mis-alignment problem are occurred, the contact resistance remain constant (Fig. 1-4). Therefore, the layout area can be retrenched due to less contact hole is necessary (Fig. 1-5).

However, as the device shrinks to nano scale, the silicide material and process suffers from many challenges such as resistance matching and interaction between the SiGe Gate [9]. In this thesis, effects of capping layers on formation and electrical properties of Ni-silicided junctions were investigated. A high-resistivity $\text{Ni}_x\text{Ti}_y\text{Si}_z$ compound layer is formed on the surface during silicidation for the Ti-capped sample. In addition, the thermal and morphological stability of NiSi on SiGe film was

investigated. We found that NiSi films formed on poly-Si/poly-SiGe stack layers possessed continuous, smooth structures.

(2) Study on the sol-gel derived nanocrystal memories

The flash memory devices are increasing interest for portable electronic productions because of its high data retention, low cost, and low power consumption characteristics. The basic concepts and the functionality of a floating gate (FG) device are easily understood if it is possible to determine the FG potential. If a charge is forced into the well, it cannot move without applying an external force: the FG stores charge. However, the FG type flash memory suffers the electron migration problem in the charge trapping layer, and will cause the charge loss and data retention degradation [10]. This interest arises from the inherent advantages of isolated nanocrystal acting as discrete floating gate nodes. The nanocrystal memory can keep the trapped charge tightly to avoid the charge loss problem found in conventional thin film storage memory (Fig. 1-6). Various materials have been used to form nanocrystals, such as silicon [11], germanium [12] and metal [13], as the charge storage layer for nonvolatile memories.

We proposed a novel sol-gel spin coating method to fabricate a compound material thin film, and transformed into nanocrystal after annealing. The sol-gel solution provided colloidal solvents or precursor compounds when metal halides were

hydrolyzed under controlled conditions in a beaker. In the sol-gel reaction, hydrolysis, condensation, and polymerization steps occurred to form metal-oxide networks in the colloid liquid. The most interesting feature of sol-gel processing in the solution is its ability to synthesize new types of materials that were known as “inorganic-organic hybrids” [14]. The sol-gel spin coating method was a simple method to deposit thin film as compared to ALD, PVD, or CVD technologies due to its cheaper precursors and tools. In addition, the film can be fabricated in the normal pressure environment instead of high vacuum system. However, to the best of our knowledge, there is no literature reported concerning to the formation mechanism of the sol-gel derived nanocrystal. In this thesis, we demonstrated the effects of annealing temperature and solvent to the nanocrystal formation. We found the film started to form the islands at 600 °C anneal, and finally transferred into NCs at 900 °C. The morphology of the nanocrystals for precursors in ethanol system was isolated type, while was interconnected form in IPA system. Ethanol as preparation solvent formed a thinner sol-gel film for spinodal decomposition, and was benefit for formation of isolated nanocrystals. In addition, Ti-based nanocrystal memory programmed by hot hole trapping method was also proposed.

(3) Research on the real-time, label-free and ultrasensitive nanowire/nanobelt

FET biosensors for cancer marker analysis

The detection of specific nucleic acid sequence has recently attracted much attention because more than 4000 inherited diseases are known [15]. Efforts are needed to identify these mutation genes, and it is desirable to explore more simple and rapid methods for biomolecule detection [16-19]. In general, the traditional techniques in detecting the biomolecule include optical and electrochemical measurements. For the optical characterization, a fluorescent group with emitting specific light of interest is labelled on the target DNA molecule. The DNA sequence is then determined by analyzing the fluorescence by an optical scanner [20]. The optical method requires the technique for fluorescent material labeling and tedious polymerase chain reaction to amplify the DNA concentration. Additionally, the electrochemical characterization uses a conventional cell embedded with three electrodes [21-22]. The electrochemical measurement requires an indicator that can selectively bind to the double-stranded DNA and a couple of surface preparation procedures thereafter. Table 1.1 lists the comparison of various disease detection and diagnosis methods.

Many advanced biological sensors, such as nanowires (NWs) and nanotubes (NTs), have recently received much attention due to their excellent characteristics for the detection of biomolecules [23-26]. In contrast to the conventional biosensing techniques, the nanowire's field-effect transistor (NW FET) sensors exhibit highly sensitive and label free detection for the biomolecules [27]. The fabrication of

nanowire-based biosensor includes the proper integration of “bottom-up” and “top-down” approach [28-29]. The “top-down” fabrication uses the state-of-the-art integrated circuit technology to scale down the designed linewidth and is compatible with the standard semiconductor process. The “bottom-up” fabrication aims to precisely tether the molecule onto the NWs or NTs. The charge carrier of the NWs or NTs can be affected by the immobilized molecule, and the variation of electrical signal can be used as the sensing indicator. The reaction capability of the molecule with the nano-scale surface and the defect formation during molecular self-assembly can seriously influence the fabrication yield, which results in the difficult integration and hinders the widespread application for the sensors.

Therefore, we fabricated NW/NB FET biosensors located on a silicon-on-insulator substrate by using the top-down complementary metal-oxide semiconductor technology. We applied the NW FET sensor as an ultrahigh-sensitivity molecular probe for the detection of a cancer-related BRAF^{V599E} mutation gene. The presence of BRAF^{V599E} mutation genes was correlated to the occurrence of melanomas, colorectal cancers, gliomas, lung cancers, sarcomas, ovarian carcinomas, breast cancers, papillary thyroid carcinoma, and liver cancers [30]. This mutation is believed to mimic phosphorylation in the activation segment by insertion of an acidic residue close to a site of regulated phosphorylation at serine 598. BRAF^{V599E} exhibits

elevated basal kinase activity and has diminished responsiveness toward oncogenic stimulation. BRAF^{V599E} also transforms NIH3T3 cells (murine embryonic fibroblasts) with higher efficiency than does the wild-type form of the kinase, consistent with its functioning as an oncogene [31]. Therefore, characterization of the BRAF^{V599E} mutation genes at the molecular level is significant for early tumor identification.

We also applied the NB FET as the biomolecular sensor in detecting the hepatocellular carcinoma (HCC). HCC is the most common primary cancer of the liver in the world. The diagnosis and treatment methods of HCC have been developed many years, while the recurrence and mortality of HCC is still high, hence the five-year survival rate of this disease is less than 5 % [32]. This vital disease is prevalent in Asia and sub-Saharan Africa. The incidence of HCC in Taiwan is steadily raising in the past years, resulting in an increase in the mortality rate from 22.7 per 100,000 population in year 1986 to 28.1 in year 2007, and it is now the first and second most common cancer in men and in women, respectively [33]. Clinical studies have shown that HCC can be cured by surgical resection in the early stage. However, since very few neurons spread in the liver, patients with HCC in the early state are asymptomatic. Most patients are diagnosed in the late-stage or metastasis state, that patients are not suitable for surgical resection. Moreover, erroneous diagnosis is another problem to be consideration due to the false positive issue by conventional

method [34]. Therefore, characterization of the HCC for early tumor identification, as well as multiplex detection with diversified cancer markers to increase the accuracy, are significant to allow the possibility of aggressive and specific therapy to save human lives.

1.3 Thesis organization

In this thesis, we applied the nano-technology to the electronic and biology fields. In chapter 2, research on nickel silicide process was demonstrated. Firstly, we investigated the effects of capping layers on formation and electrical properties of Ni-silicided junctions. We found that Ti-capped silicide sample exhibited poorer thermal stability in comparison with uncapped and TiN-capped sample due to a high-resistivity NiTiSi compound formed on the surface of Ti-capped samples, which resulted in the increase of silicide thickness and junction leakage problem. Next, the improvement of morphological stability of NiSi on Si/SiGe film was proposed. Moreover, nickel silicide formed on the nano-sized line was also investigated. A model for the stress-confined grain growth and recrystallization is proposed to explain the improved properties of the poly-Si-buffered film.

In the second section, a nanocrystal memory by a novel sol-gel method was studied. In chapter 3, the mechanism of the nanocrystal formation at different annealing temperatures and solvent were investigated. We demonstrated the sol-gel

film started to have-changing property from 600°C annealing, and finally transformed into NCs at 900°C. As to the solvent effect, the morphology of the nanocrystals for precursors in ethanol system was isolated type, while was interconnected form in IPA system. Ethanol as preparation solvent formed a thinner sol-gel film for spinodal decomposition, and was benefit for formation of isolated nanocrystals. The ethanol system derived nanocrystal memory demonstrated a large memory window (9.8 V) than IPA system (3.8 V) due to the isolated nanocrystals. Moreover, we proposed a Ti-based nanocrystals memory by utilizing the hot hole trapping to program. With the merits of high-density nanocrystals and hot hole trapping, this nanocrystal memory exhibited excellent electrical performance in terms of the large memory window, high data retention, exceptional endurance, and high program speed.

In the third section, the nanowire and nanobelt field effect transistor (FET) was fabricated for biosensing application. In chapter 4, a single crystalline silicon nanowire FET was fabricated for deoxyribonucleic acid (DNA) biosensing. We employed the BRAF^{V599E} mutation gene, which correlates to the occurrence of cancers, as the target biomolecule.

In addition, a silicon nanobelt (NB) FET was also fabricated by using the local oxidation of silicon (LOCOS) process. This approach prevents the need for expensive lithography tools to define the nanoscale pattern. The NB FET was applied as the

real-time, label-free screening of hepatocellular carcinoma (HCC). We detected alpha-fetoprotein (AFP), hepatitis B virus (HBV) DNA fragment, and solution pH, respectively, to prevent the false positive issue. This multiplex sensing of AFP, HBV, and the solution pH suggests that our direct, label-free, ultrasensitive biosensor with the microfluidic chip might be applicable as an HCC detector in real samples.



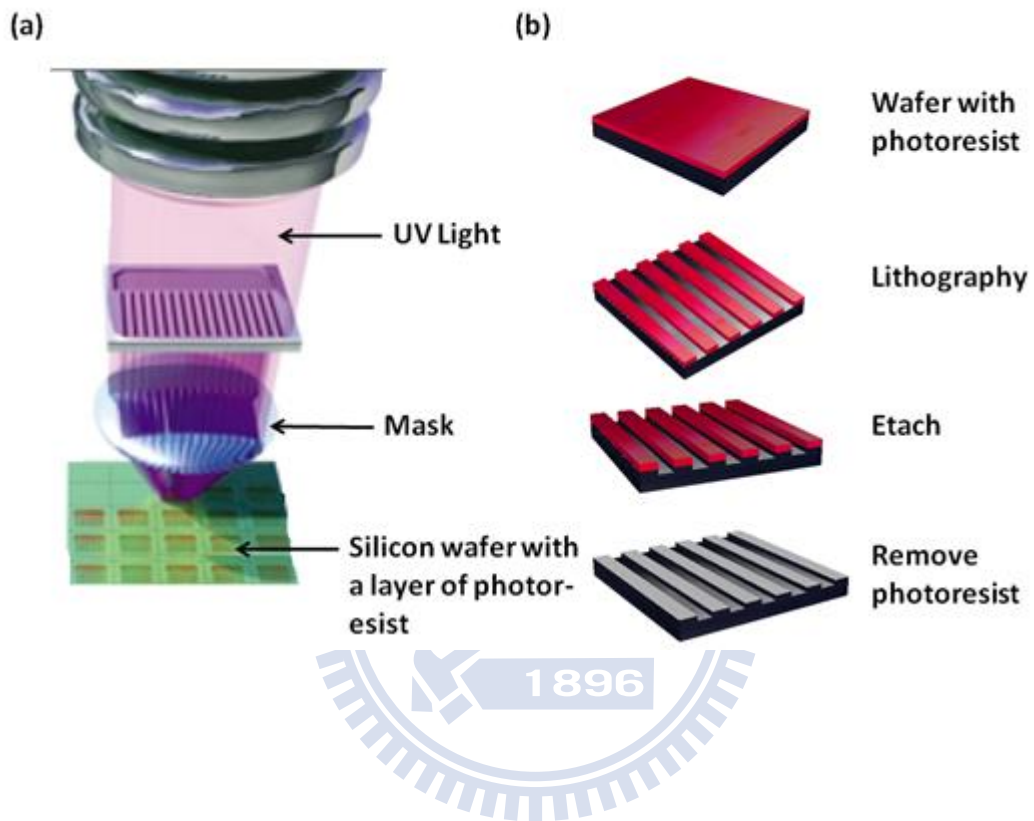


Fig. 1-1 (a) Conventional photolithography procedure. This procedure separates into two steps, step 1 is the preparation of the mask, and step 2 is the application of the mask to manufacture replicas. (b) Typical bulk-/ film-machining method, the channel is created by etching trenches in the substrate wafer or, alternatively, in the film deposited on the substrate.

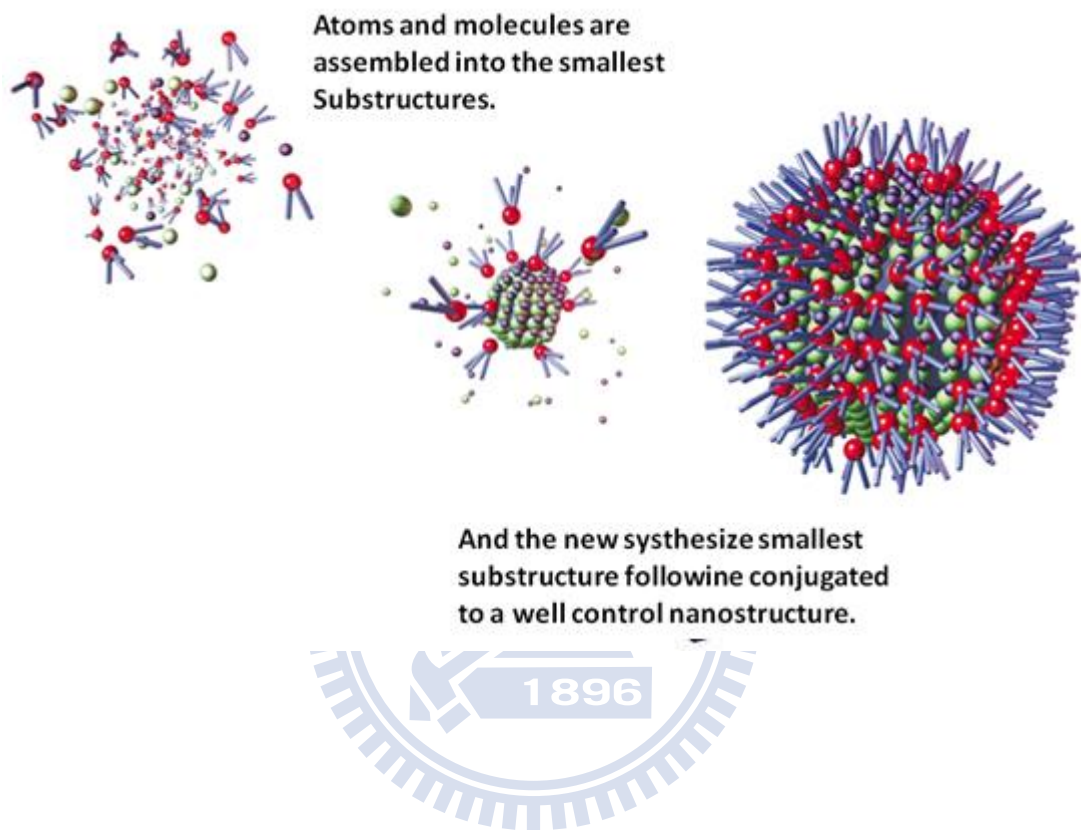
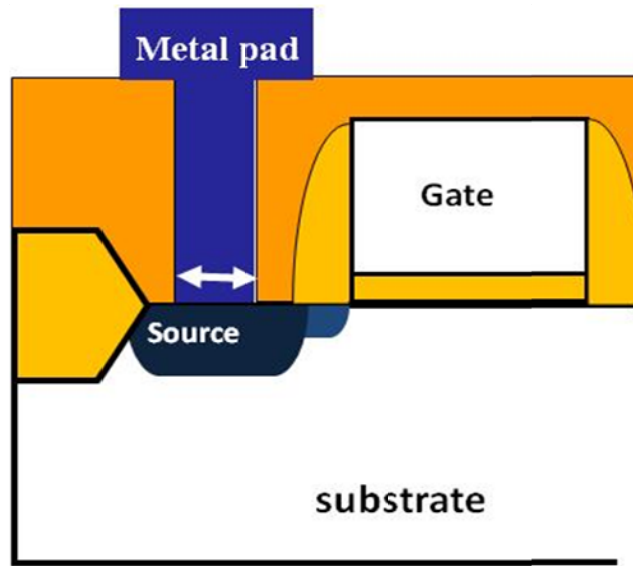
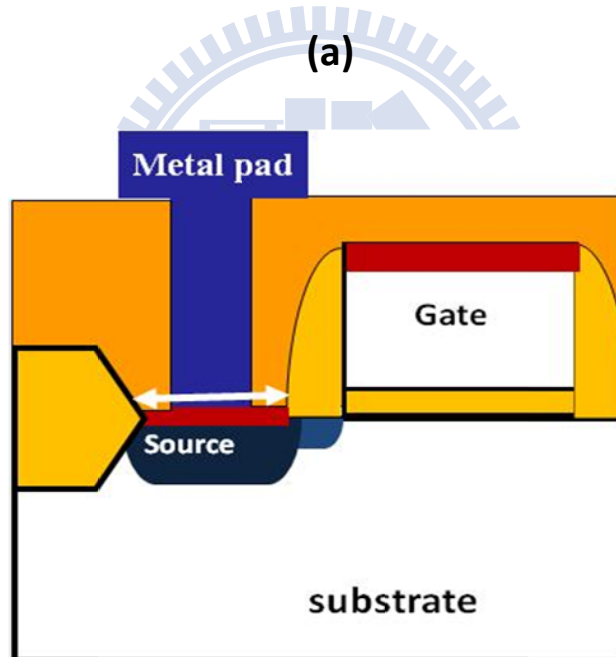


Fig. 1-2 Schematic diagram of the bottom-up procedure. A chemical reaction brings together some molecular aggregate to small crystal, and the small crystals attract surroundings into a nano-particle.



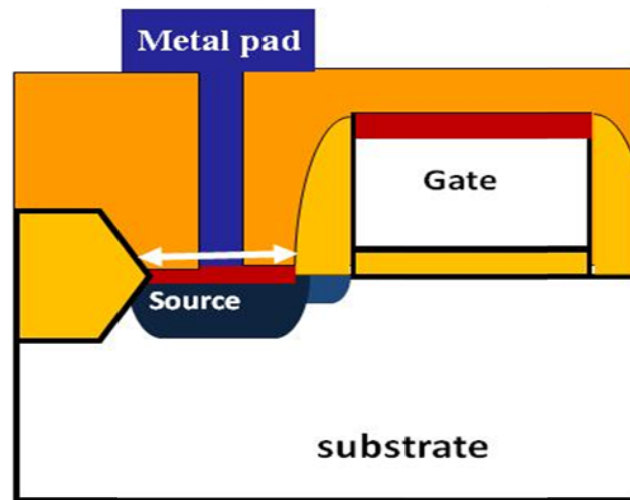
Without nickel silicide



With nickel silicide

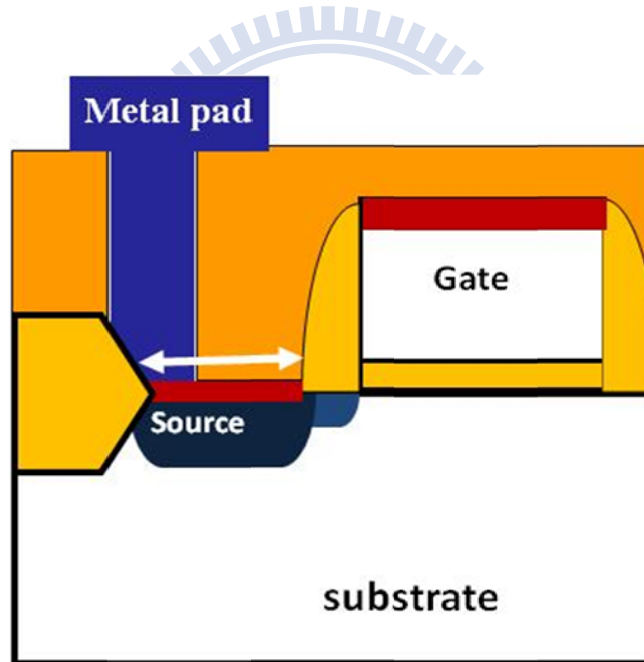
(b)

Fig. 1-3 Schematic representations of the contact resistance in nano-device. (a) The contact resistance is increased dramatically due to the contact area is reducing without nickel silicide, while (b) the contact resistance remain constant using nickel silicide as the contact metal.



Device shrinkage

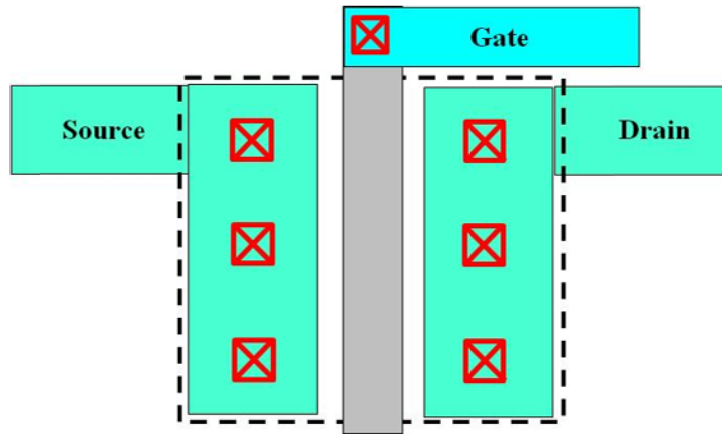
(a)



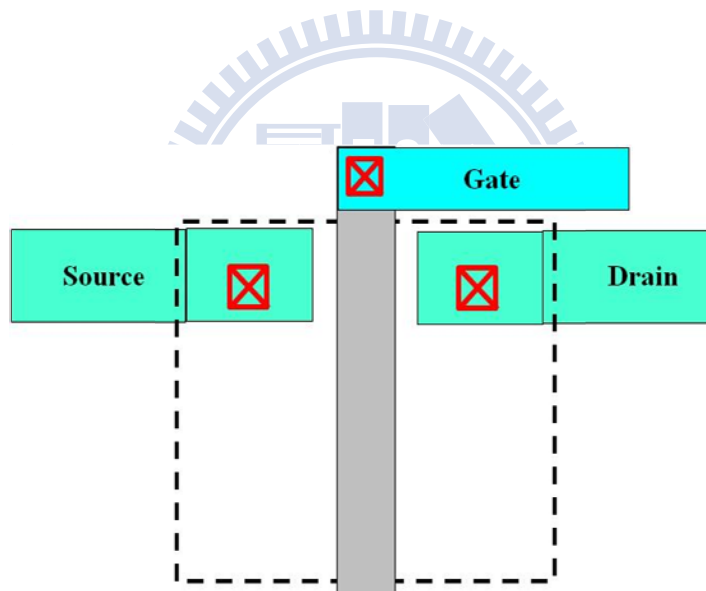
Mis-alignment

(b)

Fig. 1-4 Schematic representations of the contact resistance in shrinkage and mis-alignment problem. (a) contact hole size shrinking, and (b) contact hole mis-alignment.



Without nickel silicide



With nickel silicide

Fig. 1-5 Typical layout of the device. (a) without silicide process, and (b) with silicide process.

Floating Gate and TFS Nonvolatile Memories

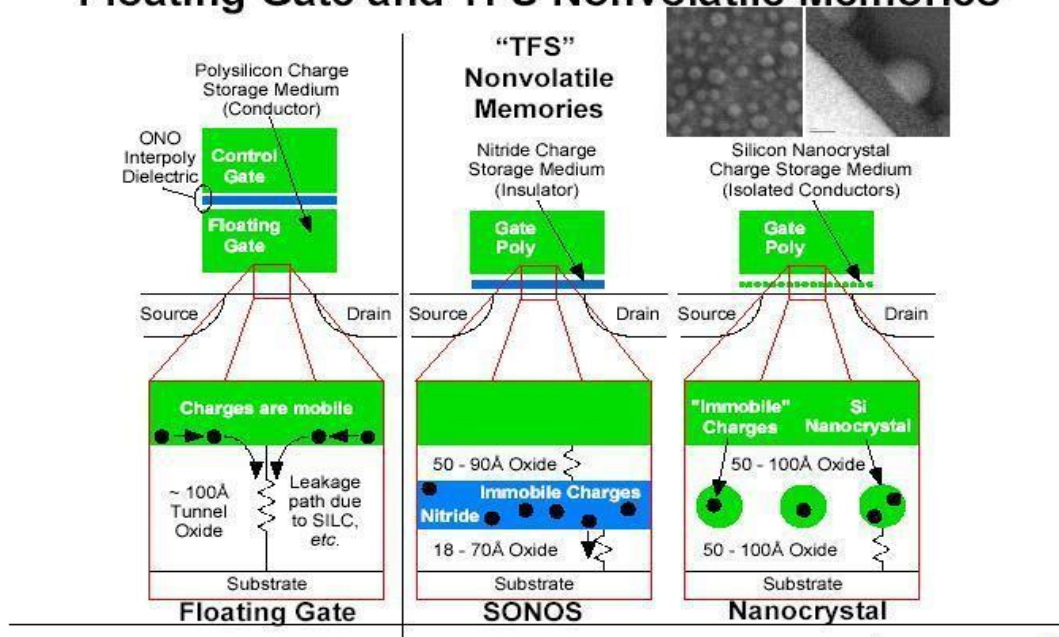



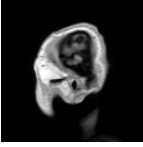



Fig. 1-6 Evolution of the non-volatile memory.

Table 1.1 Comparison of various disease detection and diagnosis methods.

Detection and diagnosis of disease					
Method	Traditional Surgery	Optics & Sonics	Bio-chemistry	Nuclear Medicine	Biotronic
					
Period	Prehistorical	Early 1900s	1980s	1990s	2000s
Advantage	<ol style="list-style-type: none"> 1. Fast 2. Mature tech 	<ol style="list-style-type: none"> 1. Fast 2. Clear image 3. Non-invasive 	<ol style="list-style-type: none"> 1. Relatively sensitive 2. Cheaper 	<ol style="list-style-type: none"> 1. Real-time 2. Clear image 	<ol style="list-style-type: none"> 1. Highly sensitive 2. Label-free 3. Real-time 4. Integration
Disadvantage	<ol style="list-style-type: none"> 1. Imprecise 2. Invasive 3. Highly risk 	<ol style="list-style-type: none"> 1. Highly risk 2. Experience requirement 	<ol style="list-style-type: none"> 1. Time-consuming 2. Indirectly 3. False positive 	<ol style="list-style-type: none"> 1. Highly risk 2. High-cost 	<ol style="list-style-type: none"> 1. Developing tech. 2. False positive

Chapter 2

Research on nickel silicide process

2.1 Introduction

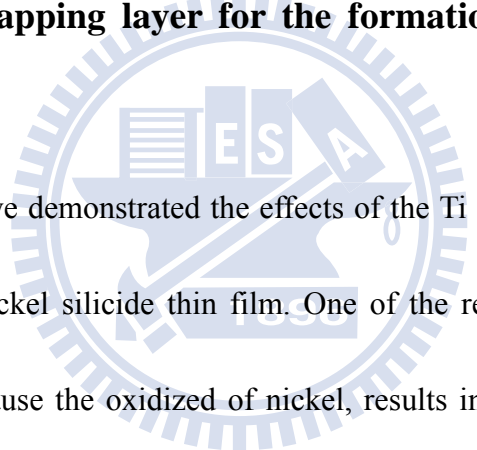
The self-aligned silicidation (SALICIDE) process is one of the critical techniques for ultra large scale integrated (ULSI) circuits, and is more emphasized as the device dimensions is towards nanometer scale. By using this technology, the contact resistance of silicide-Si interface at poly-Si gate and source/drain regions will be decreased, thereby increasing the driving current and the transconductance (G_m) of the Metal Oxide Semiconductor Field Effect Transistor (MOSFET) devices [1].

$TiSi_2$ is widely used as the silicide material for several years [2]. However, it has been found that the transformation of $TiSi_2$ from high resistivity C49 phase to low resistivity C54 phase is restricted by the linewidth, causing higher sheet resistance for lines narrower than $0.35 \mu m$ [3]. Neither $CoSi_2$ nor $NiSi$ has such linewidth dependence effects as observed in $TiSi_2$ [4]. On the other hand, with the continuously decreasing junction depth, the silicide thickness is being shrunk to decrease silicon consumption at the expense of a higher sheet resistance [5,6]. For this reason, $NiSi$ is being considered as a potential candidate for deep sub-100 nm devices because the

same sheet resistance can be obtained with less Si consumption as compared to CoSi_2 [7-9].

Although NiSi have many merits, there are obstacles to be overcome such as large junction leakage current and thermal stability related degradation. Moreover, the reaction between nickel silicide and poly-SiGe is unstable. For these reasons, the improvement of nickel silicide process was demonstrated in this chapter.

2.2 Study on the capping layer for the formation of nickel silicide junctions



In this section, we demonstrated the effects of the Ti or TiN-capped layers on thermal stabilities of nickel silicide thin film. One of the reasons of nickel silicide thermal stability is because the oxidized of nickel, results in the increase of silicide resistivity. Therefore, a capping layer on top of nickel thin film is necessary to prevent oxidant. Here we used various capping layers and compared their thermal stabilities. The results showed that there was higher leakage current for NiSi sample with the Ti-capped layer than that of the uncapped layer. Further studies identified that the excess junction leakage current was due to the Ti-Ni-Si compounds layer formed on the nickel silicide surface.

2.2.1 Experiments

The n⁺-p junctions were formed by As⁺ implantation at an energy of 20 keV with a dose of $5 \times 10^{15} \text{ cm}^{-2}$ followed by the rapid thermal annealing (RTA) process. After wafers were cleaned, they were introduced to a cluster sputtering system to deposit the metal films. Prior to the film deposition, Ar presputter cleaning was further carried out to remove the thin native oxide layer. Ni films of 20 nm and Ti or TiN films were sputtered, respectively. The thickness of Ti thin film was 10 or 30 nm, and the TiN thin film was 30 nm.

After deposition of metal films, nickel silicidation was done in a RTA (AG 610) system, followed by a H₂SO₄ + H₂O₂ mixture to selectively remove the unreacted metal. Finally, TiN /AlSiCu /TiN was deposited and patterned as the metal pad. For easy identification, the uncapped silicide sample, Ti 10 nm-capped silicide sample, Ti 30 nm-capped silicide sample, and TiN 30 nm-capped silicide sample are denoted herein as uncapped, Ti 10-capped, Ti 30-capped, and TiN 30-capped, respectively.

The leakage currents of junction diodes were determined at a reverse bias of 5V by a HP4156 semiconductor parameter analyzer. For the unpatterend sample, sheet resistance of the silicide film was measured by a four-point probe. Microstructures of the silicide films and interfaces were examined using transmission electron microscopy (TEM). The compositions and the phase identification of silicide films were carried out by energy dispersive spectroscopy (EDS) and x-ray diffraction

(XRD) analysis, respectively. Compositional depth profiles were characterized by secondary ion mass spectroscopy (SIMS).

2.2.2 Results and discussion

Fig. 2.1 compares the sheet resistance of Ni silicide using different capping layer processes after annealing at 300-800°C for 30 sec in an N₂ ambient. At temperatures below 450°C, all samples exhibit large sheet resistance and it is attributed to the formation of nickel-rich Ni₂Si phase, as analyzed in XRD spectra of Fig. 2.2. NiSi with low sheet resistance (about 4~5 Ω/□) are shown for temperatures ranging from 450 up to 600°C. At higher than 600°C, the silicide thin films start to degrade with slight increase in sheet resistance, especially for the Ti-capped samples, as shown in the inset of Fig. 2.1. The degradation for nickel silicide film annealed at higher temperature is attributed to either the phase transformation from low-resistivity NiSi to high-resistivity NiSi₂ or the agglomeration of the silicide film caused by local energy equilibrium at the intersection of grain boundaries [10].

So far as the result of sheet resistance is concerned, the uncapped and TiN 30-capped samples exhibit better thermal stability than the Ti 10-capped and Ti 30-capped samples. Obviously, it does not conduce to relevant shift of the Ni-silicided transformation temperature by using either Ti or TiN capping layer on Ni-silicidation process. This result is distinct from the phenomenon of Co-silicidation process. It has been demonstrated that the transformation point of Co₂Si to CoSi was shifted towards lower temperature by a Ti capping layer, which is arose from that the Ti capping layer lowers the activation energy for CoSi formation by eliminating the formation of SiO₂ between the growing CoSi and the Co [11]. The fact that Ti capping layer does not

play an active role for Ni silicidation process is ascribed to the lower reaction temperatures for Ni and Si.

The XRD spectra for samples annealed at 400, 450, 600 and 700°C are shown in Figs. 2.2 (a)-(d). All samples annealed at 400°C exhibit nickel-rich Ni₂Si preferred orientation. After 450°C annealing, the NiSi phase predominated, and no NiSi₂ phase was detected even the annealing temperature is up to 800°C (not shown here). This finding is consistent with the sheet resistance result that Ti-capped sample does not lead to a significant shift of the nickel silicide transformation temperature. It is more noteworthy that there are two peaks (about 40.6 and 43.3 degree) detected from the Ti 30-capped and Ti 10-capped samples (peaks from Ti 10-capped sample are unapparent, but still visible), while the uncapped and TiN 30-capped samples are not. The intensity of the two peaks that were detected from the Ti 10-capped and Ti 30-capped samples increase with increasing either the annealing temperature or the Ti thickness, which indicate that there may be a Ti-compound layer formed on silicide thin film.

To verify the composition of the Ti-compound layer, samples were further analyzed by TEM. Figs 2.3 (a)-(f) show the cross-sectional TEM images of the uncapped, TiN 30-capped, Ti 5-capped, Ti 10-capped, Ti 20-capped, and Ti 30-capped samples annealed at 650°C for 30 s, respectively. As shown in the figures, there are two layers formed on the Ti 5-capped, Ti 10-capped, Ti 20-capped and Ti

30-capped sample, while only a single layer are found on the uncapped and TiN 30-capped samples. For the Ti-capped samples, the thickness of the upper layer increased upon increasing the thickness of Ti capping. The two layers formed on the Ti 30-capped sample were also analyzed by EDS to confirm their compositions. Figures 2.4a and b show the EDS analyses of the upper layer and the lower layer formed on the Ti 30-capped sample, respectively. It is clearly seen that the upper layer is composed of a high-resistivity $Ni_xTi_ySi_z$ compound and could not be removed by etchant, while the lower layer is a relatively low-resistivity Ni-Si compound. Oxygen signal was not detected at either upper layer or lower layer in TEM and EDS results, which is distinct from the result of the previous report about $CoSi_2$ study. It was reported that a Ti cap or alloying layer is capable of gettering oxygen that is incorporated into the deposited Co, and reducing interfacial oxide in the silicidation process by forming a TiO_2 layer in the silicide surface [12]. The similar results are also found in the NiSi studies [13-14]. No detectable oxygen in this study is possibly due to the pre-etching process so that native oxide was completely removed and a clean surface was showed up to form silicide. Furthermore, it is found from Figs. 2.3b and 2.3c that the overall thickness of the silicide layers, as well as the $Ni_xTi_ySi_z$ layer, increase with increasing the Ti capping layer thickness. This result is harmful to the electrical properties of the Ni silicided device because both thinner silicide layer and

lower sheet resistance are the main demand for the ULSI technology. The thicker silicide layer will cause excessive leakage current of the source/drain region, and result in degradation in properties of the devices.

Fig. 2.5 illustrates the cumulative distributions of reverse-biased leakage current densities (J_R) for the Ni-silicided n⁺-p junction diodes annealed at 500°C for 30 sec. Twenty five randomly chosen diodes of area $0.1 \times 0.1 \text{ cm}^2$ was measured at room temperature. As shown in Fig. 2.5, the uncapped and TiN 30-capped samples exhibit smaller leakage current densities than that of the Ti 10-capped and Ti 30-capped samples. As mentioned above, the thickness of NiSi and Ni_xTi_ySi_z layers increase with increasing the Ti capping layer thickness, as shown in the TEM images of Fig. 2.3. This means that increasing the Ti capping layer thickness result in the more seriously consumed junction depth, and hence, caused larger junction leakage current.

Fig. 2.6 reveals the SIMS depth profiles of As⁺ for samples annealed at 500 °C for 30 sec. There are almost the same junction depth for the uncapped, Ti 10-capped, and TiN 30-capped samples (about $0.076 \mu\text{m}$ at $10^{19} \text{ atoms/cm}^3$). However, the As profile of the Ti 30-capped sample is shifted toward deeper side (about $0.091 \mu\text{m}$ at $10^{19} \text{ atoms/cm}^3$). This finding explains why the leakage current of the Ti 30-capped sample is slightly smaller than that of the Ti 10-capped sample shown in

Fig. 2.5. It has been demonstrated that As is depleted in the TiSi_2 layer and thus diffuses significantly into Si underneath [15]. Therefore, the Ti 30-capped sample with a thicker $\text{Ni}_x\text{Ti}_y\text{Si}_z$ compound layer, caused the impurity redistribution to induce a deeper junction depth. In addition, the “snowplough” effect that As accumulates at the silicide/Si interface, especially for the Ti 10-capped and Ti 30-capped samples, is found. This observation indicates that the Ti capping layer leads to the snowplough effect enhancement during the NiSi formation. Moreover, the accumulation of As is deeper for the Ti-capped sample, which is due to the formation of the thicker silicide layers, as shown in Fig. 2.3.

2.3 Study on morphological stability of the nickel silicide formed on polycrystalline Si/SiGe substrate

In this section, the stress-induced morphology and fine-line stability enhancement of NiSi on poly-SiGe with a buffer poly-Si interlayer was studied. Polycrystalline silicon-germanium (poly-SiGe) is a suitable candidate material for replacing polycrystalline silicon (poly-Si) at the gate electrode because of its lower dopant activation energy, higher carrier mobility [16-17], and good compatibility with standard silicon CMOS processing technologies, as well as the possibility of tuning its work function merely by changing the mole fraction of Ge [18]. In addition, poly-SiGe films can be deposited at temperatures lower than those required for

poly-Si films, presumably because of the lower binding energies of the Si–Ge and Ge–Ge bonds in poly-SiGe films relative to those of the Si–Si bonds in poly-Si films [19]. Unfortunately, combining nickel silicide processing with poly-SiGe materials suffers from the drawback that the direct reaction between nickel and poly-SiGe provides materials exhibiting relatively poor morphological stability relative to those obtained from poly-Si [20] because the melting point of the ternary alloy Ni(Si,Ge) is lower than that of NiSi. This problem restricts the further application of nickel silicide and poly-SiGe gate materials.

Here we compare the morphological stabilities and fine-line effects of Ni/poly-Si/SiO₂/Si-substrate, Ni/poly-SiGe/SiO₂/Si-substrate, and Ni/poly-Si/poly-SiGe/SiO₂/Si-substrate systems. We studied the effects of the silicidation temperature on the sheet resistance of various films. In addition, we examined the fine-line effects of nickel (germano) silicided narrow lines. Although it has been reported that the resistance of NiSi formed on poly-Si lines exhibits independent geometrical dimensions [21], no literature exists describing the electrical properties of Ni(Si,Ge) formed on narrow poly-SiGe lines. Thus, we evaluated the morphology and recrystallization effects of these films, and propose a model that accounts for the stress-induced grain growth suppression and recrystallization effects.

2.3.1 Experiments

These experiments employed 6-inch (100)-oriented silicon wafers. A 500-nm-thick silicon oxide film was first formed, followed by the deposition of a (1)

200-nm poly-Si film, (2) 200-nm poly-SiGe layer, or (3) 40-nm poly-Si/160 nm poly-SiGe stack layer. After RCA standard cleaning, 10-nm Ni and 4-nm TiN films were deposited through dc sputtering. After metal deposition, the Ni-silicidation reaction was performed in a rapid thermal annealing (RTA) system. Finally, a mixture of H₂SO₄ and H₂O₂ (3:1) was used to selectively remove the unreacted metal at a temperature of 120 °C. The sheet resistance of the silicide film was determined using a four-point probe system. A bridge structure was used in conjunction with an Agilent 4156A semiconductor analyzer to characterize the values of resistance of various narrow lines. The morphology of the film was examined using transmission electron microscopy (TEM). The stresses of these films were measured using a Tencor FLX-2320 instrument.

2.3.2 Results and discussion

After performing the silicidation reaction, the stacked (1) Ni/poly-Si/SiO₂/Si-substrate, (2) Ni/poly-SiGe/SiO₂/Si-substrate, and (3) Ni/poly-Si/poly-SiGe/SiO₂/Si-substrate films were transformed into (i) NiSi/poly-Si/SiO₂/Si-sub, (ii) Ni(Si_{1-x}Ge_x)/poly-SiGe/SiO₂/Si-sub, and (iii) NiSi/poly-SiGe/SiO₂/Si-sub species, respectively. The phase for sample (iii) was identified to be NiSi by XRD, since the thickness ratio of buffer poly-Si to Ni was close to the consumption ratio for forming the low-resistivity NiSi. Fig. 2.7 provides a comparison of the sheet resistances of these films as a function of the annealing temperature. The sheet resistances of samples (i) and (ii) increased slightly upon

increasing the annealing temperature over the range 500–800 °C, and then increased abruptly at temperatures higher than 850 °C. In contrast, the resistance of sample (iii) remained constant after annealing at temperatures between 500 and 850 °C. This observation suggests that the insertion of the buffer film (i.e., poly-Si) between the Ni and poly-SiGe films was beneficial to the electrical and thermal properties.

Fig. 2.8 displays the sheet resistances of various narrow lines of samples (i)–(iii) annealed at 600 °C. The sheet resistance of lines of sample (i) remained nearly constant for line widths ranging from 200 to 100 nm, which is consistent with previous findings [22]. The slight decrease in resistance that occurred after shrinking the line width from 100 to 60 nm was caused by edge effects of the recessed spacer forming a thicker silicide at the line's edge [23]. In contrast, the sheet resistance for sample (ii) increased upon reducing the line width. This phenomenon, the well-known fine-line effect, had been reported from a study of Ti silicide [24], but has never been reported for Ni(Si,Ge) lines formed on poly-SiGe. The fine-line effect vanished after insertion of poly-Si, i.e., for sample (iii). This behavior should improve the process stability of such systems, especially for sub-100-nm devices. We infer that the larger Ni(Si,Ge) grains resulting from the ready grain growth of poly-SiGe after annealing was the main cause of the increased sheet resistance in sample (ii). Similar behavior resulting from grain size effects has been described previously [25].

Fig. 2.9 displays cross-sectional TEM micrographs of the silicide films obtained after annealing at 850 °C. Samples (i) and (ii) (Figs. 2a and 2b, respectively) possessed completely agglomerated silicide structures that were responsible for the poor electrical properties observed in Fig. 2.7. These images also reveal the occurrence of layer inversion, i.e., the reversal of the positions of the silicide and poly-Si(Ge) layers, which is consistent with previous findings [26]. These

agglomerated silicide islands resulted from poly-Si(Ge) grain growth and a recrystallization effect during treatment at high temperature. Fig. 2.10 illustrates the schematic diagram of silicide agglomeration process. It has been reported that the Ge segregation effect of Ni(Si,Ge) would result in a more severe thermal stability problem for Ni(Si,Ge) formed on poly-SiGe [27]. The segregation of Ge from Ni(Si,Ge) grains is driven by the heat of formation for SiGe being more favorable than that of NiGe. In contrast, the grains in sample (iii) retained their columnar structure and a uniform interface existed between the silicide and poly-SiGe (see Fig. 2.9c and its inset), which is the same as Fig. 2.10c. The uniform interface is likely caused by the Ge, which is expelled from the Ni-Si-Ge compound, blocked the Ni diffusion paths and resulted in the delay in the formation of NiSi₂ [28-29]. Similar result were also reported for CoSi₂ formed on a SiGe layer [30]. This observation implies that the insertion of the poly-Si film in sample (iii) maintained the film's continuance and curtailed agglomeration of the silicide film.

In Fig. 2.11 we propose a model to explain the stress-induced grain growth suppression of the silicide film. In terms of thermodynamics, the driving force for the morphological transformation of a grain is the reduction of interfacial energy. Figure 2.11a displays schematically the morphology changes that occurred to samples (i) and (ii) after annealing. Increasing the annealing temperature enhances the sizes of the poly-Si and poly-SiGe grains, with the silicide migrating along the grain boundary, resulting ultimately in agglomerated island and layer inversion occurring at excessively high temperatures [31]. Figure 2.11b provides an explanation of the benefit of inserting the poly-Si film into sample (iii). The underlying poly-SiGe layer exerts a compressive stress upon the upper poly-Si film. This stress suppressed the grain growth of the poly-Si and silicide, which in turn retarded the agglomeration and

layer inversion effects. In addition, the Ge layer between the silicide and poly-SiGe film also play the role to retard layer inversion [28-30]. This model can also explain the behavior of the Ni(Si,Ge) fine lines of sample (ii). The thermal stability of silicided-narrow lines is determined by the laterally confined areas, and larger grains induce linewidth-dependent degradation [15]. Larger silicide grains readily formed columnar structures and then converted into bamboo-like structures as the line width shrank; agglomeration into islands then occurred during annealing. For sample (iii), the fine-line effect was eliminated in the presence of the inserted poly-Si layer because of suppression of the growth of silicide grains; therefore, the formation of bamboo-like structures was retarded.

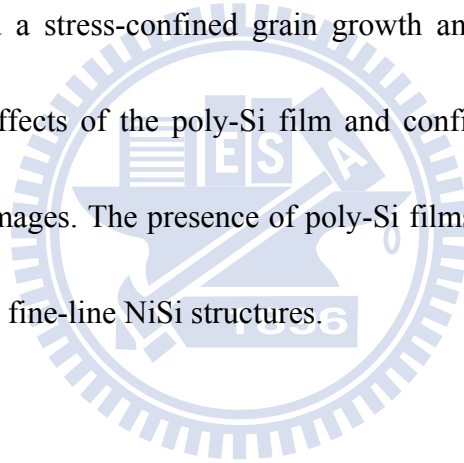
To support this model with respect to the stress effect in sample (iii), we prepared three samples having various poly-SiGe film thicknesses. We found that samples possessing smaller compressive stresses exhibited inferior electrical properties after annealing at high temperatures, especially when the annealing temperature exceeded 850 °C. This finding is consistent with our prediction that compressive stress enhances the thermal and morphological stabilities of nickel silicide samples.

2.4 Summary

In section 2.2, effects of capping layers on formation of Ni-silicided junction were investigated. With a Ti-capped layer on Ni-silicided sample, it is shown to exhibit inferior thermal stability than the uncapped and TiN-capped samples. For the silicided junctions, samples with a Ti capping layer are shown to have larger leakage

current density. A high-resistivity $\text{Ni}_x\text{Ti}_y\text{Si}_z$ compound layer formed on the NiSi surface for the Ti-capped sample, resulted in the overall silicide thickness and the junction leakage current increased. In addition, we find that the Ti capping layer enhance the snowplough effect during the NiSi formation.

In section 2.3, the thermal stability and electrical behavior of various nickel (germano) silicide structures were investigated. The insertion of a poly-Si film on poly-SiGe significantly enhances the thermal and morphological stabilities of NiSi films. We have derived a stress-confined grain growth and Ge blocking model to explain the beneficial effects of the poly-Si film and confirm the predictions made after scrutiny of TEM images. The presence of poly-Si films improved the properties of both the thin-film and fine-line NiSi structures.



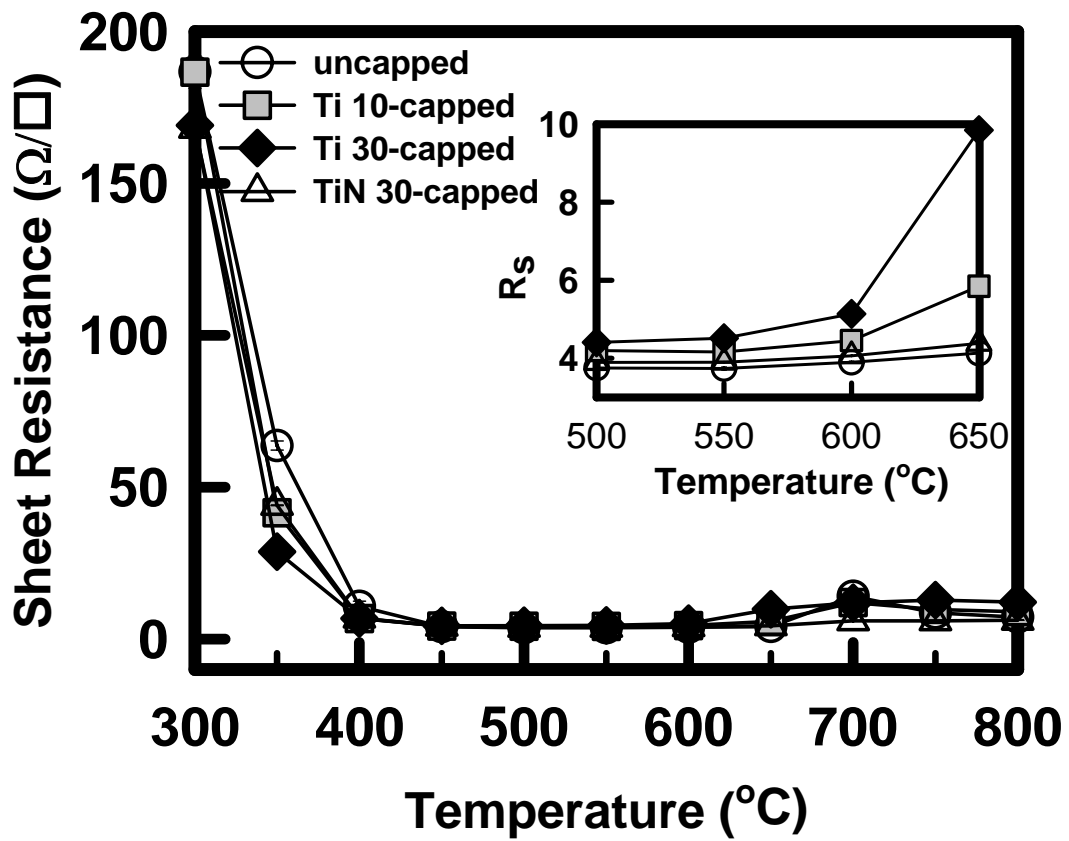


Fig. 2.1 Sheet resistance of NiSi using different capping layer processes as a function of annealing temperature.

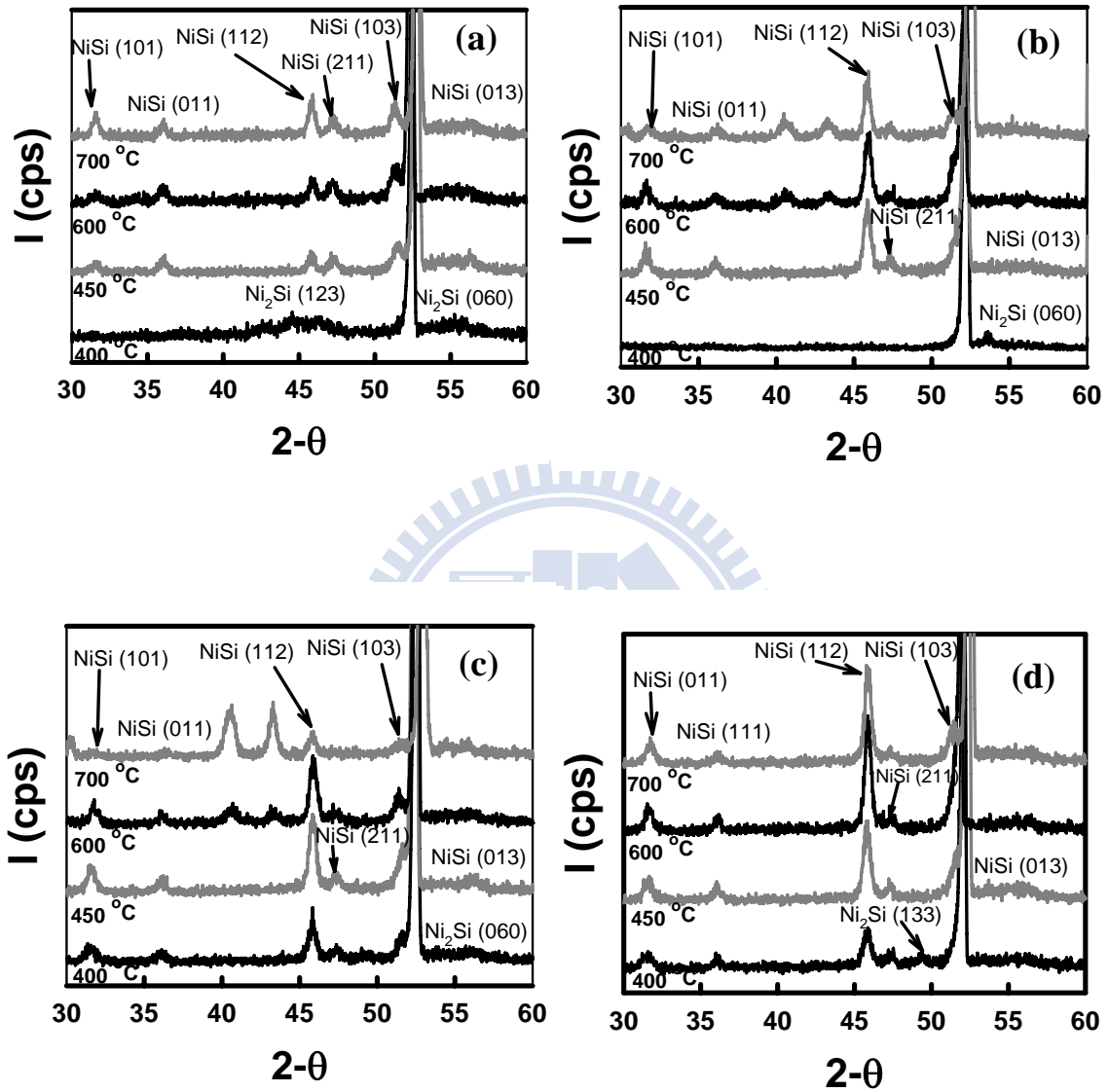


Fig. 2.2 XRD spectra of (a) uncapped, (b) Ti 10-capped, (c) Ti 30-capped, and (d) TiN 30-capped samples after annealing at 400-700°C for 30 sec.

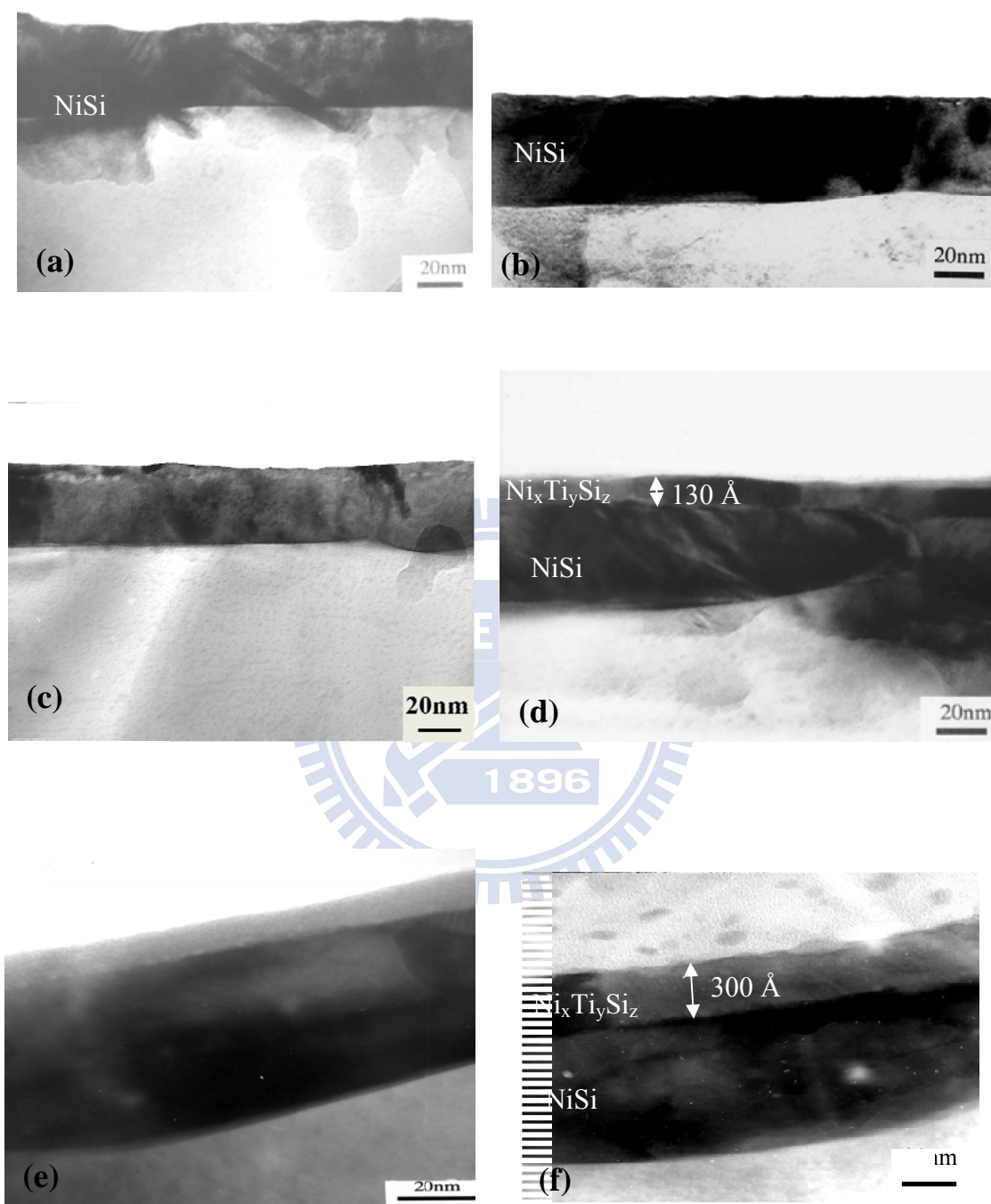
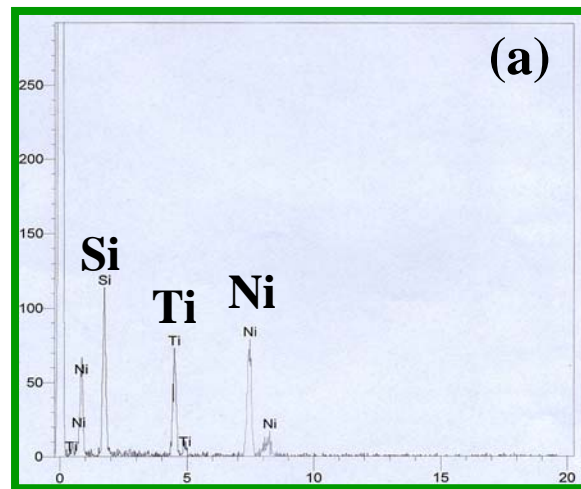
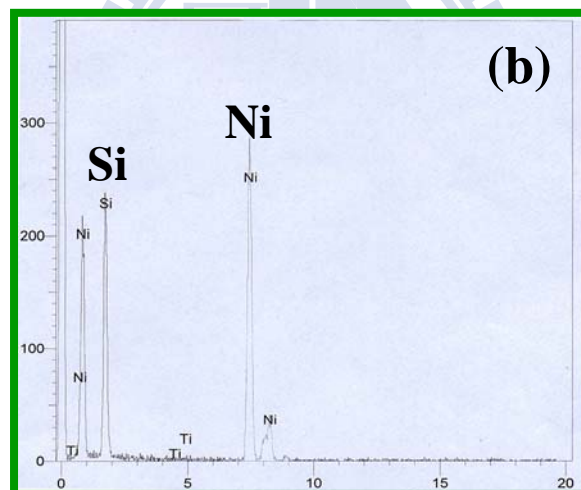


Fig. 2.3 Cross-sectional TEM images of (a) uncapped, (b) TiN 30-capped, (c) Ti 5-capped, (d) Ti 10-capped, (e) Ti 20-capped, and (f) Ti 30-capped samples after annealing at 650°C for 30 sec.



Energy (Kev)



Energy (Kev)

Fig. 2.4 EDX spectra of (a) the upper layer and (b) the lower layer formed on the Ti 30-capped sample.

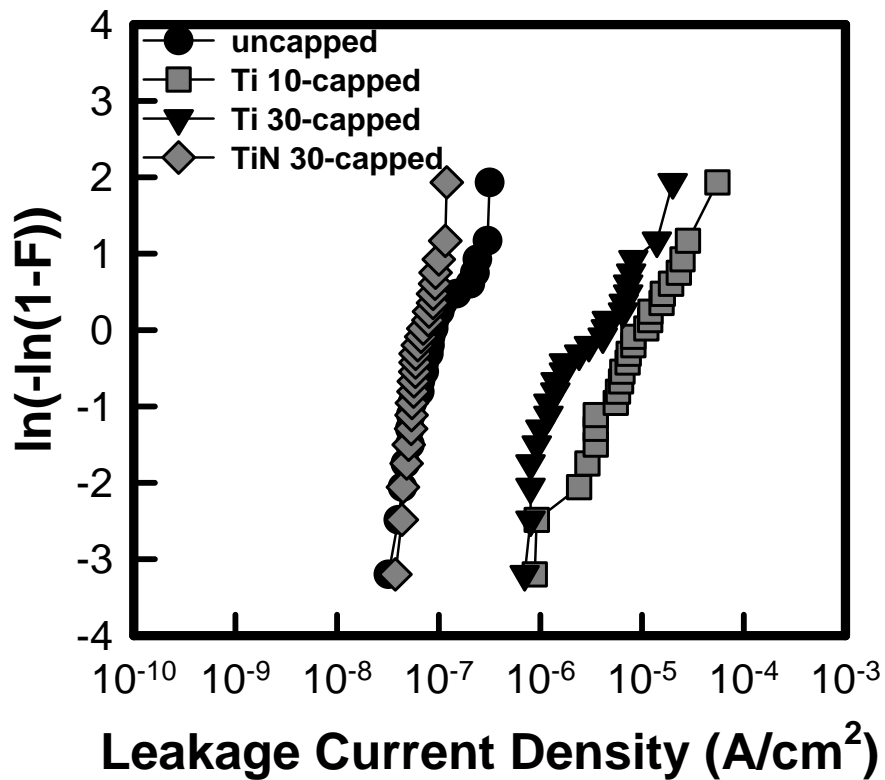


Fig. 2.5 Cumulative distribution of reverse-biased leakage current densities for the Ni-silicided n^+ -p junction diodes annealed at $500^\circ C$ for 30 sec.

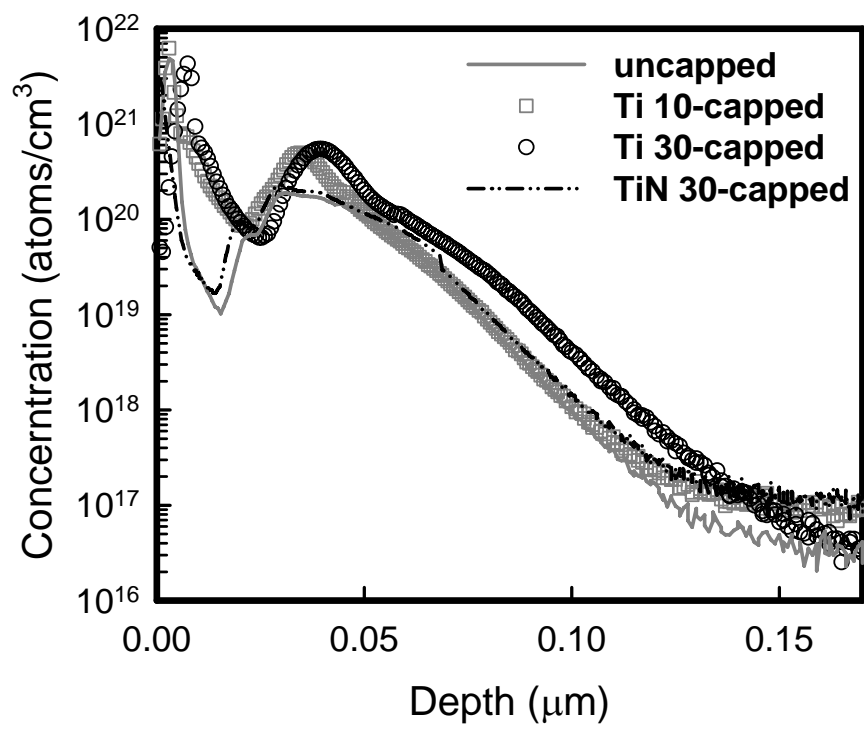


Fig. 2.6 SIMS depth profiles of As⁺ for samples annealed at 500°C for 30 sec.

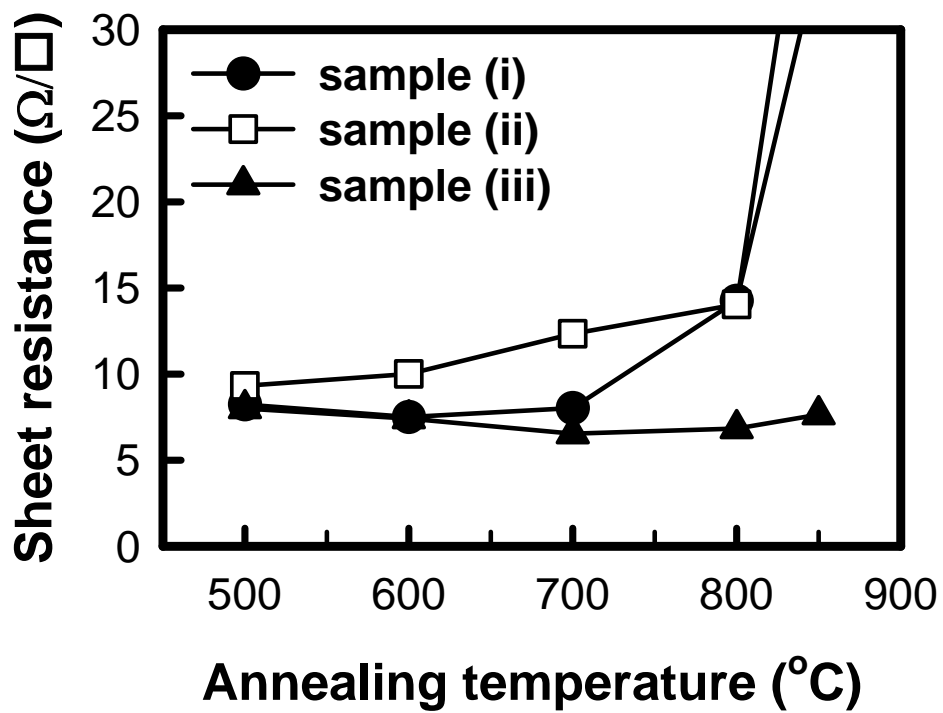


Fig. 2.7 Sheet resistances of the nickel (germano)silicide films formed on poly-Si (sample (i)), poly-SiGe (sample (ii)), and poly-Si/poly-SiGe stack layers (sample (iii)) as a function of the annealing temperature.

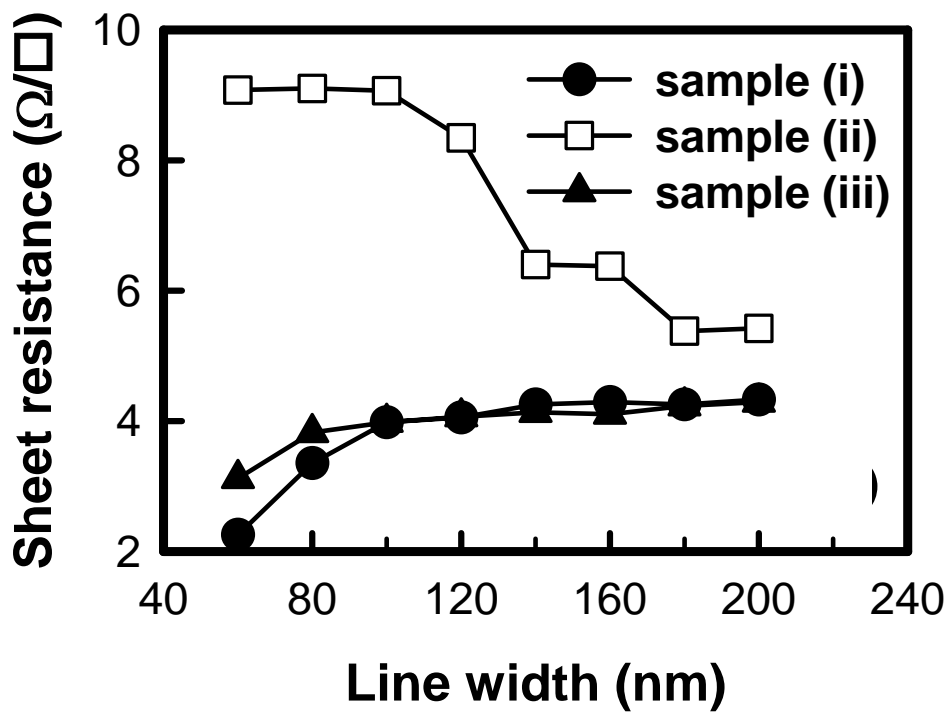


Fig. 2.8 Sheet resistances of the nickel (germano)silicide lines annealed at 600 °C as a function of the line width.

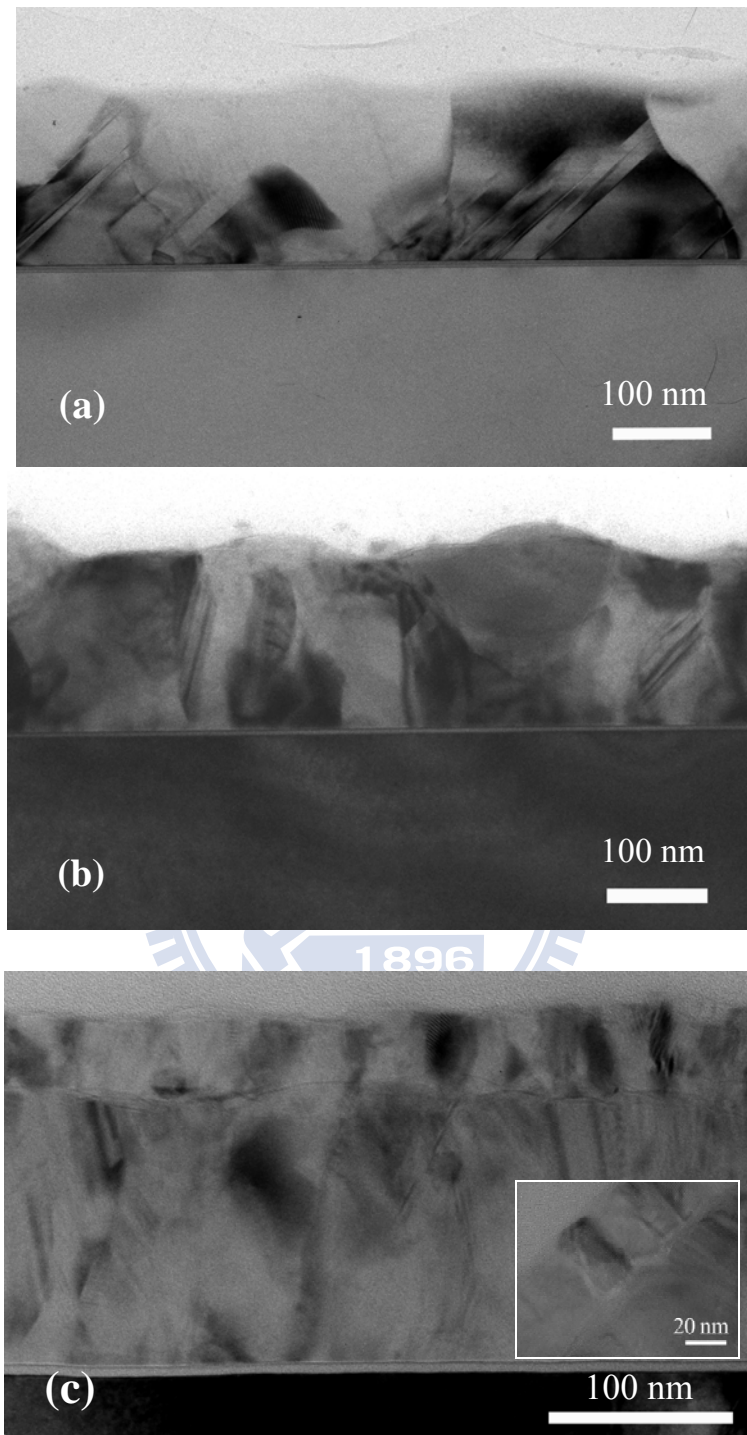


Fig. 2.9 Cross-sectional TEM micrographs of the nickel (germano)silicide films formed on (a) poly-Si (sample (i)), (b) poly-SiGe (sample (ii)), and (c) poly-Si/poly-SiGe stack layers (sample (iii)) after annealing at 850 °C.

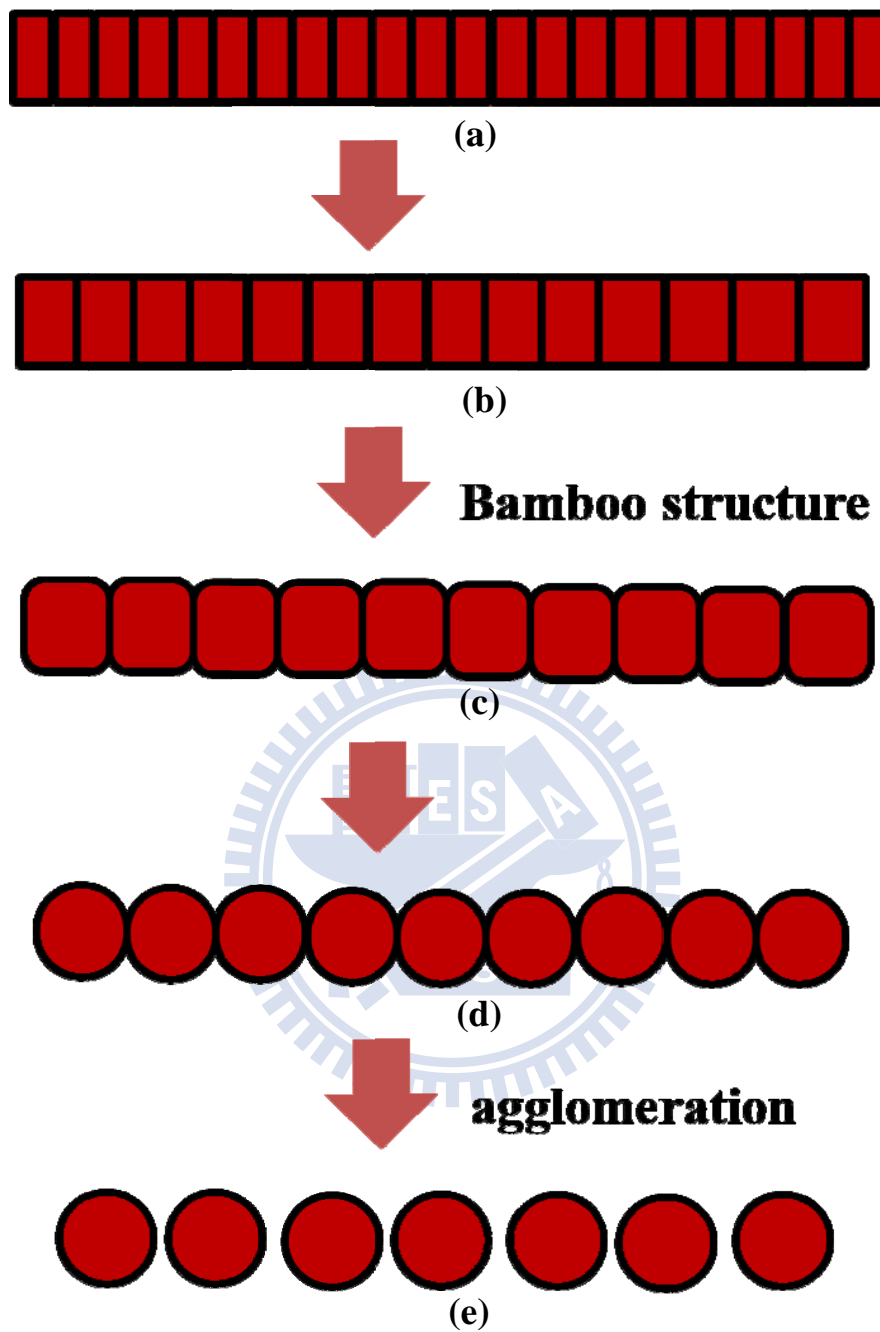


Fig. 2.10 Schematic representations of silicide agglomeration process.

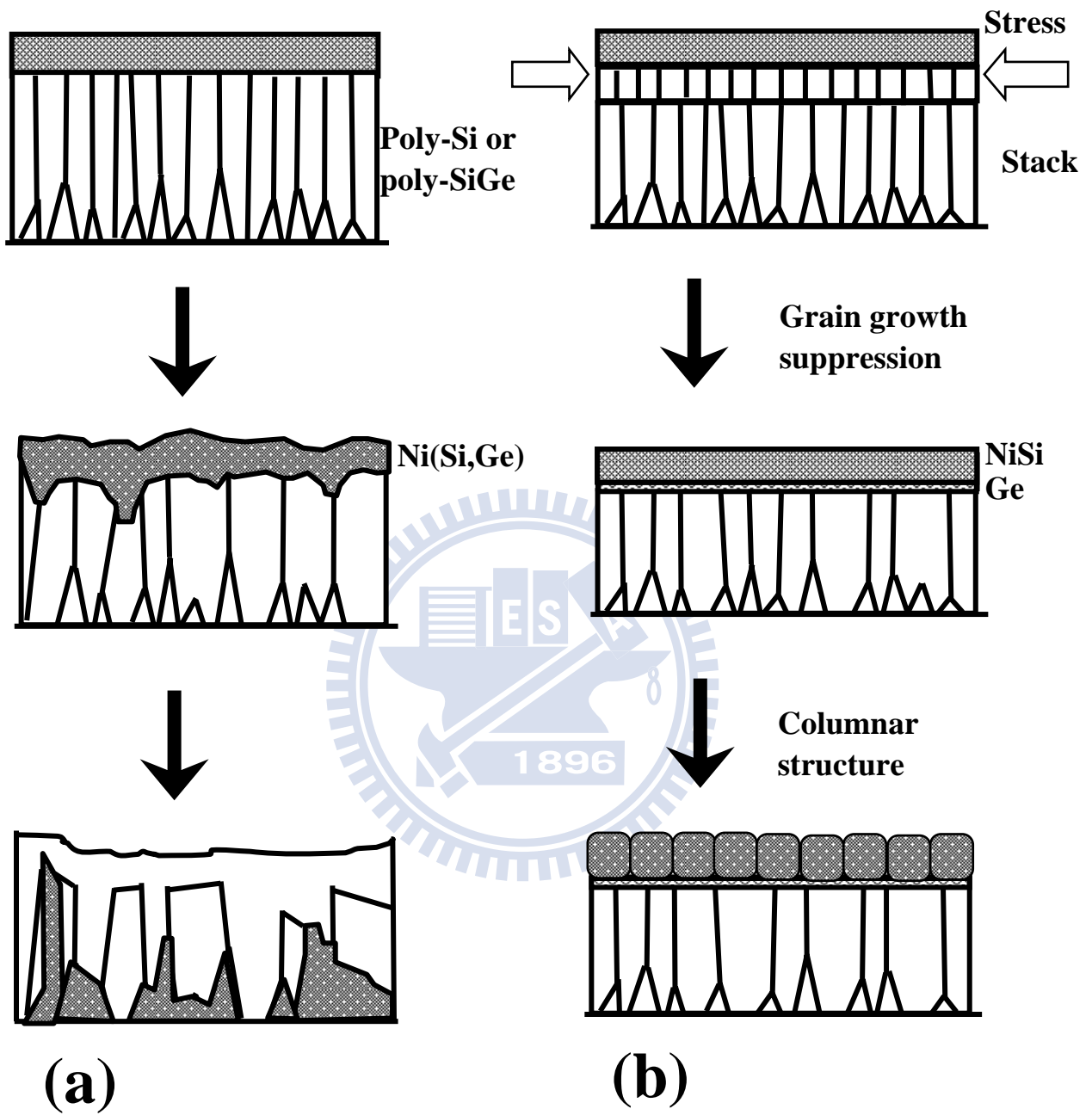


Fig. 2.11 Schematic models of nickel (germano)silicide formation at high annealing temperature: (a) on poly-Si (sample (i)) and poly-SiGe (sample (ii)); (b) on poly-Si/poly-SiGe stack layers (sample (iii)).

Chapter 3

Study on the sol-gel derived nanocrystal memories

3.1 Introduction

Memory storage is an important technology that enables the growth in the information world. With the rapid growth of the internet, wireless communication products, personal digital assistants (PDAs), digital cameras, digital camcorders, digital music players, and computers, there is continually a demand for superior information storage technology. The development of portable consumer electronics has spurred the need for high-density nonvolatile memory with low power consumption for system on-chip applications. Considering the flexibility-cost plane, it turns out that the flash memory offers the best compromise between these two parameters, since they have smaller cell size and excellent flexibility (they can be electrically written on field more than 100,000 times, with byte programming and sectors erasing)[1]. In recent years, flash memories based on charge storage in nitride traps, such as poly-silicon/SiO₂/Si₃N₄/SiO₂/semiconductor (SONOS) structures have been investigated intensively [2-3]. However, the conventional SONOS memory still suffers from erase saturation and insufficient charge-trapping efficiency, which markedly degrade its performance [4-5].

Nanocrystal nonvolatile memory (NC-NVM) has predominant advantages when it was proposed in the early 1990s by Tiwari et al.[6]. NC memory have attracted much attention as one of the strong candidates for non-volatile memory due to its scalability, electrical isolation and low charge leakage through the tunneling oxide. The demand for high-density, low-cost, low-power consumption, and fast program/erase speed NC NVM will lead the current thin film memory technologies to several revolutionary and evolutionary approaches [7-8]. The only stored charges at the nanocrystals adjacent to the defect leak through the tunneling dielectric, compared to huge charge loss of conventional flash memory due to the lateral charge transport [9-11]. The possibility of exceeding the performance limits of the conventional floating-gate device spurred many subsequent investigations on this approach. Only the electrons stored on the nanocrystal directly above the defect chain will be affected since the nanocrystals are separated from each other. The tunnel oxide thickness of the nanocrystal memory device can be reduced to allow faster programming and lower voltage operation [12].

Various methods have been employed to form the nanocrystals (NCs), including atomic layer deposition (ALD) [13], physical vapor deposition (PVD) [14-15], chemical vapor deposition (CVD) [16], and ion beam synthesis [17]. Gerardi et al.[18] employed the low pressure chemical vapour deposition (LPCVD) to fabricate Si

nanocrystals for density up to $2 \times 10^{12} \text{ cm}^{-2}$, and then, utilized Si nanocrystals as the memory cell. King et al. [19] fabricated Ge nanocrystals by oxidation of a $\text{Si}_{1-x}\text{Ge}_x$ layer formed by ion implantation, and demonstrated quasi-nonvolatile memory operation with a 0.4 V threshold-voltage shift. Lin et al. [20] reported co-sputter technique to fabricate high density HfO_2 nanocrystals and utilized to nanocrystal memories with about 4 V threshold-voltage shift. These methods usually use complicated procedures of chemical template, ultrahigh vacuum system and expensive instrumentation to fabricate the NC. In contrast, a cost-effective method to form NC by using simple sol-gel spin-coating process was first proposed by our group [21]. The sol-gel method can provide colloidal solvents or precursor compounds when metal chlorides are hydrolyzed under controlled conditions. This approach is relatively cheap, simple, and can be fabricated in a normal atmospheric pressure instead of high-vacuum system. We have successfully achieved the nanocrystal memories with superior characteristics in terms of considerably large memory window, high speed P/E, long retention time, and excellent endurance.

In this chapter, the sol-gel derived nanocrystal memory was investigated. The study was divided into three sections. In the first section, the effect of annealing temperature for the formation of nanocrystal was demonstrated. We found the nanocrystallization was correlation to the interfacial tension of sol-gel thin film. In the

second section, effect of solvent for the sol-gel derived NC memory was investigated. The solvent was an important parameter for NC formation. The ethanol system formed a thinner sol-gel film and hence led to the isolated NCs, while the interconnected morphology was observed in the IPA system. In the third section, a novel programming method by using hot hole trapping was observed for the Ti-based NC memory. The Ti-based NC memory exhibited improved data retention characteristic and excellent electrical performance because the effective mass of hole was much heavier than that of electron in silicon, therefore the hot hole could be caught into a deeper level trap when injected to the charge trapping layer.

3.2 Effect of annealing temperature for the formation of nanocrystals

The crystallization of transferring the charge trapping thin film into the nanocrystal phase during thermal annealing is dependent on the sol-gel composition, preparation solvent and annealing temperature. The formation of coexisting hafnium silicate and zirconium silicate nanocrystal memory has published previously [22]. In general, the nanocrystal formation is related to the solid phase segregation induced seeding effect [23]. However, the effect of annealing temperature that controlling the formation of nanocrystal, degree of crystallization, interfacial energy and charge retention in the sol-gel derived memory is still unclear.

3.2.1 Experiments

Prior to various annealing treatments, the sol-gel thin film was deposited by the spin-coating method from the precursors of zirconium tetrachloride, hafnium tetrachloride, and silicon tetrachloride. The above precursor was dissolved into the ethanol, and a suitable amount of hydrochloric acid serving as the catalyst for hydrolysis and condensation was added into the solution. The molar ratio for $ZrCl_4$, $HfCl_4$, $SiCl_4$, and ethanol in the sol-gel solution was 1:1:1:1000. The solution after preparation was stirred for 0.5 hr, and then spin-coating onto the Si substrate by using a TEL system (Clean Track Model-MK8). After thin film deposition, these samples were subjected to rapid thermal annealing (RTA) treatment at various temperatures for 60 s under an O_2 ambient to form the NCs.

The fabrication of sol-gel spin-coating NC memory was started with local oxidation of Si process on a p-type (100) silicon substrate. A 10 nm tunneling oxide film was thermally grown at 925 °C in a furnace. The sol-gel film was then formed through spin-coating and RTA process mentioned above. The 20 nm blocking oxide was deposited by plasma enhanced CVD tetraethylorthosilicate, followed by a 200-nm-thick poly-Si gate was deposited. Finally, gate patterning, source/drain (S/D)

implanting, and the rest of the subsequent metal-oxide-semiconductor processes were used to fabricate the NC-NVM devices.

3.2.2 Results and discussion

The cross-sectional high resolution transmission electron microscope (HRTEM) images of the sol-gel derived thin films that annealed at 400, 600, and 900°C are illustrated in Fig. 3.1. The sample in Fig. 3.1(a) after 400°C RTA exhibits a continuous and smooth film. This observation suggests the annealing at 400°C has no effect on the film's morphology. As to the sample annealed at 600°C, Fig. 3.1(b) reveals the morphology of thin film is discontinuous and uneven. The sol-gel film is gradually transferred into islands (in inset). If the annealing temperature is elevated to 900°C, the film illustrated in Fig. 3.1(c) is complete transferred into NCs. The crystal size is estimated to 6-10nm. Literature has been proposed the spinodal decomposition effect [24] to explain the annealing effect for formation of zirconium silicate. We infer the darker NCs in Fig. 3.1(c) are formed from the high-molecular-weight hafnium silicate, and the bright NCs are from the low-molecular-weight zirconium silicate [22]. To verify the composition of the nanocrystal, the sample was analyzed by Energy Dispersive Spectrometer (EDS). Fig. 3.2 shows the EDS spectra of the

sol-gel derived nanocrystals. As seen in the figure, the nanocrystal is composed of Hf, Zr, Si, and O.

The nature of the chemical bonding for the transformation of thin film into nanocrystal was characterized by using X-ray photoelectron spectroscopy (XPS) analysis. Fig. 3.3 provides a comparison of the XPS results for (a) Si 2*p*, (b) Zr 3*d*, (c) Hf 4*f*, and (d) O 1*s* bonding for samples annealed at different temperatures. Fig. 3.3(a) shows the increasing of binding energy of Si 2*p* from 100.40eV (400°C RTA) to 100.95eV (900°C RTA) with annealing temperature. This observation relates to the oxidization of Si atom toward blue shift. Both binding energies of Zr 3*d* and Hf 4*f* shown in Figs. 3.3(b) and (c) exhibit the shifting to the higher energies upon increasing the annealing temperature. This observation suggests that the oxygen atoms of Zr–O and Hf–O bonds reacted with their nearby Si atoms, forming hafnium and zirconium silicate [25]. As to the O 1*s* spectra in Fig. 3.3(d), each peak can be deconvoluted into two peaks, i.e., the higher and lower energy peaks, which are respectively attributed to the SiO₂ and metal-rich silicate [26]. If the annealing temperature is increased, the intensity ratio of lower energy peak to higher energy peak is increased. This result indicates the hafnium and zirconium silicates were toward the bonding of metal-rich silicate. This finding is also consistent with the observation of Hf 4*f* and Zr 3*d* spectra.

Fig. 3.4 shows the interfacial tension (interfacial energy per unit area) of the hafnium and zirconium silicates as a function of annealing temperature [27]. As Fig. 3.4 depicted, the interfacial energy increases abruptly from 400°C to 600°C RTA, and then slight decrease from 600°C to 1050°C. As Fig. 3.1(a) mentioned, the surface at 400°C RTA is still smooth and possesses the lowest energy. The surface morphology of 600°C RTA sample is rough in Fig. 3.1(b), implying that the surface is unstable and in higher energy state. At 900°C RTA, the interfacial energy is decreased in comparison with 600°C RTA due to the formation of nanocrystal. We proposed a model in Fig. 3.5 to describe the observed transformation phenomenon on the sol-gel film. The sol-gel film is continuous and smooth as deposited, and retains the same morphology at 400°C annealing. It becomes unstable at 600°C annealing, and phase change is then observed in order to reduce the surface energy. Upon 900°C annealing, the sol-gel film reaches a stable state due to the formation of NCs.

The sol-gel derived NC was used as the charge trapping purpose in the NVM device. Figs. 3.6(a) and (b) illustrate the retention characteristics for the devices annealed at 600 and 900°C, respectively. For both samples at 25°C measurement, the retention times can be extrapolated up to 10^6 s for only ~5% charge loss, while ~10% charge loss at 85°C measurement. As the measuring temperature increased to 125°C, a significant charge storage at 10^4 sec is observed for the 600°C annealed sample, while

the 900°C annealed sample still retain its good characteristic for <20% charge loss. This result explains the importance of NC formation for the NVM. The nanocrystal is discrete dispersion in the charge trapping layer, which alleviates the charge loss problem when defects exist in the thin tunneling oxide. The inset of Fig. 3.6(b) shows the I_D - V_G characteristic for the 900°C annealed sample. We use channel hot electron (CHE) injection to program, and band to band tunneling induced hot hole injection (BTBHH) to erase. The V_t shift after programming can be up to 9 V, which is much better than our previous reports [22, 28].

Fig. 3.7 shows the disturbance characteristics of the sol-gel derived NC memory. The Drain disturbance shown in Fig. 3.7(a) on programmed state and applied $V_D = 5$ and 10 V with $V_G = V_S = V_B = 0$ V to the device. The V_t shift after 10^4 sec operation was less than 0.3V at $V_D = 5$ V measurement, and less than 0.5 V at $V_D = 10$ V measurement. We measured the Gate disturbance on erase state devices and applied $V_G = 9$ and 10 V with $V_D = V_S = V_B = 0$ V to the device. After 10^4 sec at 25°C, small extent of less than 0.3V was found, which is shown in Fig. 3.7(b). Fig. 3.7(c) illustrates the read disturbance characteristic at 25°C measurement. We measured the read disturbance on erase state at $V_G = 4$ V, $V_D = 2$ V with $V_S = V_B = 0$ V, and the memory cell almost without any disturb. While at $V_G = 4$ V, $V_D = 4$ V operation, a visible but small disturbance less than 0.5 V were found after 10^4 sec measurement.

The multi-bit characteristic of the NC memory was also demonstrated here. The schematic representation of the 2-bit operation of NC memory is illustrated in Fig. 3.8. The charges were trapped in both Source and Drain sides, while not disturbed to each other. Fig. 3.9 demonstrates the feasibility of performing 2-bit operation with NC memories through a reverse-read scheme in a single cell. From the I_D - V_G curves, it is clear that the forward and reverse reads could be employed to detect the information stored in the programmed bit_1 and bit_2, respectively. The read operation was achieved using a reverse-read scheme.

3.3 Effect of solvent for the formation of nanocrystals

The capability of sol-gel method is to synthesize various types of NCs by mixing any material of interest [29]. However, the preparation solvent is a decisive factor on determining the sol-gel film thickness. The mutual solubility of inorganic salt and the solvent affects the solution's dispersion state and viscosity. The film's thickness has some relationship with the growth mechanism and extent of phase separation for annealed NC due to the effect of spinodal decomposition [30]. The spinodal decomposition occurs upon specific thermal annealing for transformation of the sol-gel thin film into the NCs. However, the formation mechanism of NC from

deposited sol-gel film is still unclear, especially for the relationship of thickness and NC phase separation.

Spinodal decomposition is a thermodynamically spontaneous reaction of compositional fluctuations when a homogeneous phase becomes unstable under annealing condition [31]. The morphology of the NC is continuous variation with the annealing condition. For a deposited thin film, the stress relaxation at surface or stress gradient along the film thickness causes an inhomogeneous decomposition rate and the development of alternating layers of the phases lying parallel to the surface [32]. The mechanism of spinodal decomposition induces the deposited thin film transformation into interconnected or discrete morphology of NCs. The morphology of decomposed phases depends on the deposited film thickness, annealing temperature, solvent type and the composition.

In this section, we explored the mechanism of NCs formation by sol-gel technique utilizing spinodal decomposition of zirconium silicate and hafnium silicate after sufficiently RTA treatment. We demonstrated the assumption of sol-gel solution prepared by different solvents with various viscosities effected NC formation and isolation degree. We theoretically explained this phenomenon using a model of the phase separation accompanied with the nano-crystallization, based on the experimental data of coexist Zr-silicate and Hf-silicate NCs. The sol-gel derived NCs

as charge storage layer of memory was also fabricated to demonstrate its electrical characteristic.

3.3.1 Experiments

The precursors of zirconium tetrachloride ($ZrCl_4$, 99.5%, Aldrich), hafnium tetrachloride ($HfCl_4$, 99.5%, Aldrich), and silicon tetrachloride ($SiCl_4$, 99.5%, Aldrich) were utilized for the preparation of sol-gel solution. The precursors used in sol-gel process including metal or metalloid elements were surrounded by different kinds of reactive ligands such as halides. The precursors were dissolved in solvent respectively with ice-bath and to prevent aggregation. Here we used ethanol and 2-propanol (IPA) as the solvents to disperse the precursors, respectively. Hydrochloric acid was added to the solution as the catalyst because acid-catalyzed gels were therefore aggregates of very small ultimate particles. The solution after preparation was stirred vigorously for 0.5 hr to ensure homogeneous state. Owing to the precipitation reason, we selected the concentration of 1:1:1:1000 to do the experiments following. The sol-gel solution prepared by ethanol solvent and IPA solvent were spin-coated on the silicon substrates by Tokyo Electron Limited (TEL) system (Clean Track model-MK8) apparatus to deposit sol-gel film by rotation speed of 3000 rpm for 60 sec, respectively. Due to different viscosity, different thickness of the deposited sol-gel

thin film was fabricated. After spin-coating, these samples were subjected to annealing at 900°C for 60 sec in an O₂ ambient to nano-crystallization from phase separation of spinodal decomposition.

To demonstrate its electrical performance, the sol-gel derived NCs were employed as the charge storage layer of the SONOS-type memory. Fig. 3.10 displays the structure and process flow for the preparation of the NC memories. The fabrication of the sol-gel derived memory devices involved the LOCOS isolation process on p-type, 5–10 Ω-cm, (100) 150 mm silicon substrates. After a standard RCA clean process, 10-nm-thick tunnel oxide was thermally grown at 925°C by a dry oxidation process in a furnace. Subsequently, the sol-gel film was spin-coated onto the sample, and was subjected to RTA treatment under an O₂ ambient at 900°C for 60 sec in order to form NCs. A blocking oxide of 20 nm in thickness was deposited by Plasma Enhanced Chemical Vapor Deposition (PECVD), followed by deposition of a 200-nm-thick amorphous Si as gate material. Gate lithography, gate etching, source/drain (S/D) implanting, substrate and contact patterning, followed by the rest of the subsequent standard complementary metal oxide semiconductor (CMOS) procedure, were then performed to complete the fabricating of the sol-gel derived SONOS-type memory devices.

3.3.2 Results and discussion

First of all, Brookfield viscometer to measure the viscosity of different sol-gel solutions at 20 °C was utilized. We measured the viscosity of molar ratio concentration $\text{ZrCl}_4:\text{HfCl}_4:\text{SiCl}_4:\text{solvent} = 1:1:1:1000$, $1:1:1:500$, and $1:1:1:1000$, respectively, with ethanol and IPA as solvent. The viscosity and thickness of various sol-gel solutions with respect to composition of precursor are listed in Table 3.1. Basically, the inorganic sol-gel salt in IPA solvent demonstrates the higher viscosity than in ethanol solvent. This observation suggests the better solubility of inorganic salt in ethanol solvent, and therefore, the relative thinner spin-coating film. Interestingly, the solutions of molar ratio of $\text{ZrCl}_4:\text{HfCl}_4:\text{SiCl}_4:\text{IPA} = 1:1:1:500$ and $1:1:1:100$ exhibit the precipitation effect, and the corresponding sol-gel film are not successfully achieved. This observation suggests the important issue of intrinsic solvent property for the preparation of sol-gel thin film for NVM. In general, a low viscosity fluid generates a thinner film during spin-coating process.

The pseudo-binary $\text{ZrO}_2\text{-SiO}_2$ phase diagram is illustrated in Fig. 3.11(a), and the $\text{HfO}_2\text{-SiO}_2$ system also demonstrates the similar phase diagram [33]. In meta-stable phase equilibrium, the $\text{ZrO}_2\text{-HfO}_2\text{-SiO}_2$ system is the crystalline silicate. As a function of compositional concentration with respect to the annealing temperature in Fig. 3.11(b), the phase separation of sol-gel film will occur by spinodal

decomposition. The RTA under 900°C and composition ($\text{ZrO}_2\text{:HfO}_2\text{:SiO}_2=1:1:1$) of the sol-gel film is within the region of spinodal decomposition. Seol and Hu utilized computer simulation to predict the spinodal decomposition process [34]. They suggested the morphology of decomposed phases on initially homogeneous thin film strongly depended on the film thickness and the composition. The thin film after RTA may be interconnected NC in addition to the isolated NC. In our sol-gel experiment, the initial composition of precursors was fixed to study the phase separation of spinodal decomposition. For example in Table 3.1, the film thickness can be varied by solvent type. The thickness of ethanol and IPA for $\text{ZrCl}_4\text{:HfCl}_4\text{:SiCl}_4\text{:solvent}=1:1:1:1000$ in Table 3.1 is 2.0 and 3.2 nm, respectively.

Structural characterization for the evaluation of spinodal decomposition of charge trapping layer is achieved by the high-resolution transmission electron microscopy (HRTEM, JEOL 2100F) at 300 kV. The respective cross-section TEM image of the charge trapping NCs fabricated from ethanol and IPA solvents are demonstrated in Fig. 3.12. The formed NCs in Fig. 3.12(a) used ethanol solvent to prepare sol-gel solution, and annealed at 900°C for 60 sec. The morphology of charge trapping film completely transferred into isolated NCs. In contrast, the sample in Fig. 3.12(b) was prepared from IPA solvent and the morphology of NCs was in difference with the ethanol system. The NCs obtained from IPA solvent was interconnected

morphology. What is the growth mechanism for such different NC morphology by only varying the sol-gel solvent? The mechanism responsible for the formation of discrete or interconnected NCs is dependent on the phase separation of spinodal decomposition for the annealed sol-gel thin film mentioned early.

Stemmer and coworkers proposed the meta-stable phase diagram for the thin film of zirconium silicate and hafnium silicate [35]. They concluded that the film had the driving force for a thermodynamically meta-stable state of the spinodal decomposition under RTA at 900°C. Therefore, we depict a pathway in Fig. 3.13 for explaining the thickness phenomenon of spinodal decomposition on sol-gel thin film. As to the thinner film (such as 2.0 nm in Table 3.1) by ethanol solvent, a series of phase separation mechanism is depicted in Fig. 3.13(a). The first step shows the initial stage of sol-gel deposited film before annealing. The second step illustrates the morphology of thin film is continuous and smooth, and which retains the similar morphology under low-temperature annealing (~400°C). Upon 600°C RTA in step 3, the film starts to perturb, and becomes not only discontinuous but uneven. Finally, at the 900°C RTA, the phase transformation by spinodal decomposition leads to the completely isolated NCs. On the contrary, the morphology for the thicker film (such as 3.2 nm in Table 3.1) from IPA solvent system demonstrates the three-dimensional and interconnected NC structure at 900°C RTA.

In order to evaluate the charge trapping capability of the isolated and interconnected NC NVM, we fabricated the memory by following the schematic diagram of device structure in Fig. 3.10. Fig. 3.14 shows I_D - V_G characteristics of the NC memories at fresh, program, and erase state, respectively. The measured condition for programming is: $V_G = 10$ V, $V_D = 10$ V, and erasing: $V_G = -6$ V, $V_D = 10$ V. The memory fabricated by ethanol system shown in Fig. 3.14(a) exhibits a relatively large memory window of about 9.8 V, and is significantly larger than sample by IPA system of about 3.8 V window and other reports [36-39]. We infer the ethanol system with initially thinner film is beneficial for the better charge trapping performance due to the formation of isolated NCs through spinodal decomposition. The morphology of isolated NC in silicon dioxide can exhibit better charge trapping efficiency than the interconnected NC.

Fig. 3.15 shows the charge retention characteristics of the sol-gel derived NVM. The normalized V_t shift in % is defined as the ratio of V_t shift at the time of interest and at the beginning ($t=1$ sec). For NVM fabricated by ethanol solvent system, the retention times in Fig. 3.15(a) is extrapolated up to 10^6 sec for less than 5% charge loss at 25°C measurement. Under 85°C measurement, the retention times of NVM to 10^6 sec demonstrates less than 10% charge loss. As to the IPA system NVM at 85°C characterization, a significant amount of 15% charge loss at 10^6 sec is observed. This

result suggests the isolated NC from ethanol system is beneficial for data retention than interconnected NC from IPA system.

Regarding to device reliability, there also arises a challenge as the flash memory is repeatedly programming and erasing. The memory will be degraded as if the device suffers from the formation of a new defect during the applied voltage. The endurance of NC NVM after 10^4 programming and erasing (P/E) cycle is illustrated in Fig. 3.16. The measured condition for programming is: $V_G = 10$ V, $V_D = 10$ V, 10 ms, and erasing is: $V_G = -6$ V, $V_D = 10$ V, 10 ms. For NVM in ethanol and IPA solvent systems, the memory window narrowing after 10^4 P/E cycles are calculated to be 9.8 and 10.5 %, respectively. The endurance characteristic shows little difference between ethanol and IPA systems. In addition, the good endurance characteristic also indicates that the amount of operation-induced trapped electrons is very tiny.

3.4 Hot hole trapping characteristic of the Ti-based nanocrystal memory

Generally, the NC memory used channel hot electron (CHE) injection to program, which positive pulses were applied synchronously to the gate and drain of the device, and hence electrons are injected into the charge storage layer [40]. However, there is little information available on the study of NC memory

programmed by hot hole injection. Because the effective mass of hole ($m_p/m_0 = 0.69$) is much heavier than that of electron ($m_n/m_0 = 0.26$) in silicon [41], the hot hole is expected to be caught into a deeper level trap when injected to the charge trapping layer. Therefore, the data retention characteristic of the memory will be improved by hot hole trapping.

In this section, the $\text{Ti}_x\text{Zr}_y\text{Si}_z\text{O}$ NC was synthesized by sol-gel method and was employed as the charge trapping layer of the memory. This NC memory exhibited an interesting hot hole trapping property. A band diagram is theoretically derived to explain this hot hole trapping results. The electrical characteristics, including retention, endurance, and program speed for the NC memory are also demonstrated.

3.4.1 Experiments

The precursors utilized for the preparation of sol-gel solution were titanium tetrachloride (TiCl_4 , 99.5%), zirconium tetrachloride (ZrCl_4 , 99.5%), and silicon tetrachloride (SiCl_4 , 99.5%). Ethanol was used as the solvent to disperse the precursors. Hydrochloric acid serving as the catalyst for hydrolysis and condensation was added into the solution. The molar ratio of 1:1:1:1000 for TiCl_4 , ZrCl_4 , SiCl_4 , and ethanol were mixed and stirred vigorously for 0.5 hr to ensure homogeneous state. The sol-gel was then spin-coating onto the Si substrate. After thin film deposition,

samples were subjected to annealing at 900 °C for 60 sec in an O₂ ambient to transform into the NCs.

The fabrication of sol-gel derived NC memory was started with local oxidation of Si process on a p-type (100) silicon substrate. After clean process, a 4 nm tunneling oxide film was thermally grown at 925°C in a furnace. The sol-gel film was then spin-coating followed by RTA process. A 10 nm blocking oxide was deposited by PECVD, and a 200-nm-thick amorphous-Si gate was then deposited. Afterward, the rest of the subsequent MOS processes were performed to complete the sol-gel derived NC flash memory devices. Fig. 3.17 shows the plan-view TEM image of the sol-gel derived NC. The density of NC is estimated to be 2E12 cm⁻², with an average size is to be about 3~5 nm.

3.4.2 Results and discussion

The nature of the chemical bonding of the sol-gel derived Ti_xZr_ySi_zO nanocrystal was characterized by using XPS analysis. Fig. 3.18 provides the XPS results for (a) Ti 2*p*, (b) Zr 3*d*, (c) Si 2*p*, and (d) O 1*s* bonding of the sol-gel derived nanocrystal annealed at 900°C. The XPS results verify the composition of the Ti_xZr_ySi_zO nanocrystal.

Fig. 3.19 shows the I_D-V_G characteristics of the NC memories at fresh, program, and erase state, respectively. The measured condition for programming is: V_G = -7 V,

$V_D = 7 \text{ V}$, 1 ms, and erasing is: $V_G = 7 \text{ V}$, $V_D = 7 \text{ V}$, 1 ms. Unlike the memory that programmed by CHE, the I_D - V_G curve of the memory in Fig. 3.19 exhibits a shift to the left after programming, implying that the trapped charge to NC is hot hole. Therefore, a band-band hot hole (BBHH) was used to program in this study, and CHE was used to erase. We have tried to program by injecting the electrons (by applying a positive voltage to both the gate and drain), but no significant shift of the I_D - V_G curve was observed. On the contrary, the memory window by BBHH method can be up to 4.3 V, which is significantly larger than other reports [42-47]. We infer the high-density and isolated NCs are beneficial for the better charge trapping performance due to sufficient trapping site in the NCs.

The retention characteristics of the NC memory devices at various measurement temperatures are illustrated in Fig. 3.20(a). The normalized V_t shift is defined as the ratio of V_t shift at the time of interest and at the beginning ($t = 1 \text{ sec}$). The retention times are extrapolated up to 10^6 sec with only about 8%, 11%, and 25% charge loss at 25, 85, and 125°C measurement, respectively. Compare to other sol-gel derived NC memories reported previously [46-47], the retention characteristic by hot hole trapping is much improved. The superior performance is attributed to the effects of the isolated NCs and hole-trapped into the deep trap energy level, hence no significant lateral and vertical charge leakage occurred.

The endurance of NC NVM after 10^4 programming and erasing (P/E) cycle is illustrated in Fig. 3.20(b). The measured condition for programming is: $V_G = -7$ V, $V_D = 7$ V, 1 ms, and erasing is: $V_G = 7$ V, $V_D = 7$ V, 1 ms. The memory window narrowing after 10^4 P/E cycles is calculated to be 10.9 %. The threshold voltage shifts in programming and erasing states are slightly after cycles. The good endurance characteristic indicates that the amounts of operation-induced trapped charges are very tiny.

Although the retention characteristic is improved by hot hole trapping method, the program/erase speed is a concern due to heavy effective mass of hole. Therefore, the program and erase speeds of the NC memory are measured under various bias conditions and are shown in Fig. 3.21. As seen in the figure, the V_t shift increases upon increasing the programming time, and finally saturated at about -7.2 V. In addition, with increasing the applied program voltage, the V_t shift also increases. The program speed can be as fast as $24.3 \mu\text{s}$ with a -2 V V_t shift for program condition of $V_G = -8$ V, $V_D = 8$ V. Compared to other reports of flash memory devices [42-47], the sol-gel derived NC memory exhibits a relatively fast programming speed under similar condition. The erase speed shown in Fig. 3.21(b) is much faster than program speed, which is $1.4 \mu\text{s}$ with a 2 V V_t shift for erase condition of $V_G = 8$ V, $V_D = 8$ V. This result indicates the sol-gel derived NC memory yields a high efficiency charge

storage layer with fast programming speed and low programming voltage by the hot hole trapping method.

Fig. 3.22 illustrates the inferential energy band diagram of the sol-gel derived $\text{Ti}_x\text{Zr}_y\text{Si}_z\text{O}$ NC memory under thermal-equilibrium. The energy level of the NC conduction band is expected lower than that of the Si substrate. Therefore, longer programming time is required for hot electron injected from the Si substrate to the trapping site of the NC. On the other hand, the programming time for hot hole injection through tunnel oxide and trapped in the NC is much fast. This inferential energy band diagram explains why the $\text{Ti}_x\text{Zr}_y\text{Si}_z\text{O}$ NC memory used hot hole trapping to program, but it needs to further experimental prove.

3.5 Summary

In section 3.2, we have discussed the NCs formation of the sol-gel spin-coating thin film at different annealing temperatures. The XPS characterization indicated the annealing treatment under oxygen ambient can activate the formation of metal silicates (i.e. hafnium silicate and zirconium silicate). Together with the TEM images and interfacial energies, we propose a model to explain the transformation of thin film into nanocrystals. The 400°C treatment has no effect on the thin film, while 600 and 900 °C anneals affect the film's morphology. The film after morphology change has higher interfacial energy, and crystallization can minimize the energy. The sol-gel

derived NCs successfully played the role of charge trapping purpose in the memory. The 900 °C annealed sample demonstrates the satisfactory retention characteristic than the 600 °C annealed sample due to the NC formation. The large V_t shift of the 900 °C annealed sample is potential for future multi-bit application.

In section 3.3, we investigated the factor of sol-gel film thickness that affected the morphology of NCs. The solvent for precursor played an important role on the solution viscosity and film thickness. The IPA system was more viscous than ethanol system for sol-gel precursor under the same concentration. The thinner film by ethanol system led to the isolated NCs, while the interconnected NCs morphology was observed in the thicker film by IPA system. The sol-gel derived isolated NCs of ethanol system that applied in flash memory device exhibited better charge trapping performance, larger memory window, better retention times, and excellent endurance.

In section 3.4, a sol-gel derived NC memory by utilizing the hot hole trapping to program was proposed. With the merits of high-density NCs and hot hole trapping, this NC memory exhibited excellent electrical performance in terms of the large memory window, high data retention, exceptional endurance, and high program speed.

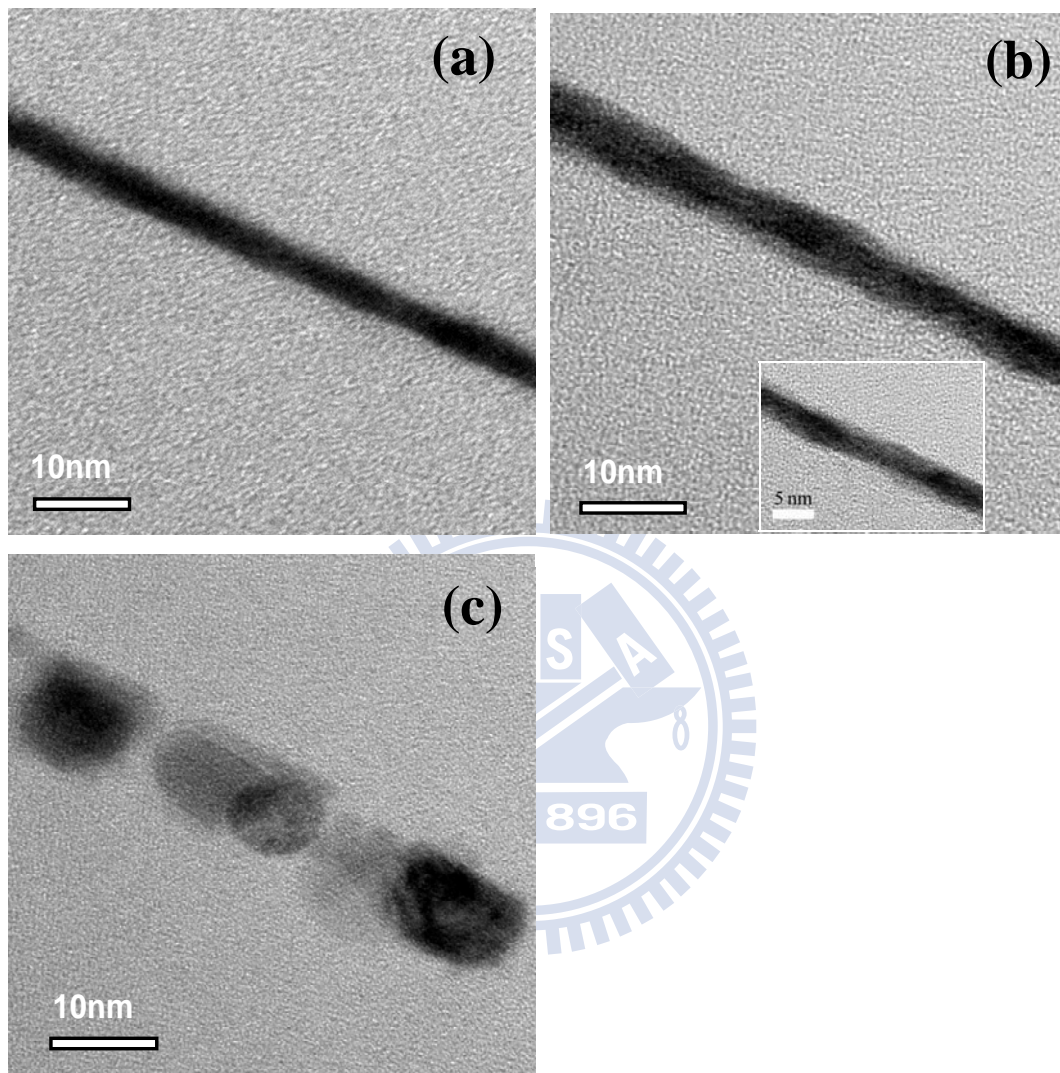


Fig. 3.1 Cross-sectional TEM micrographs of the thin film transformation after (a) 400°C, (b) 600°C, and (c) 900°C annealing.

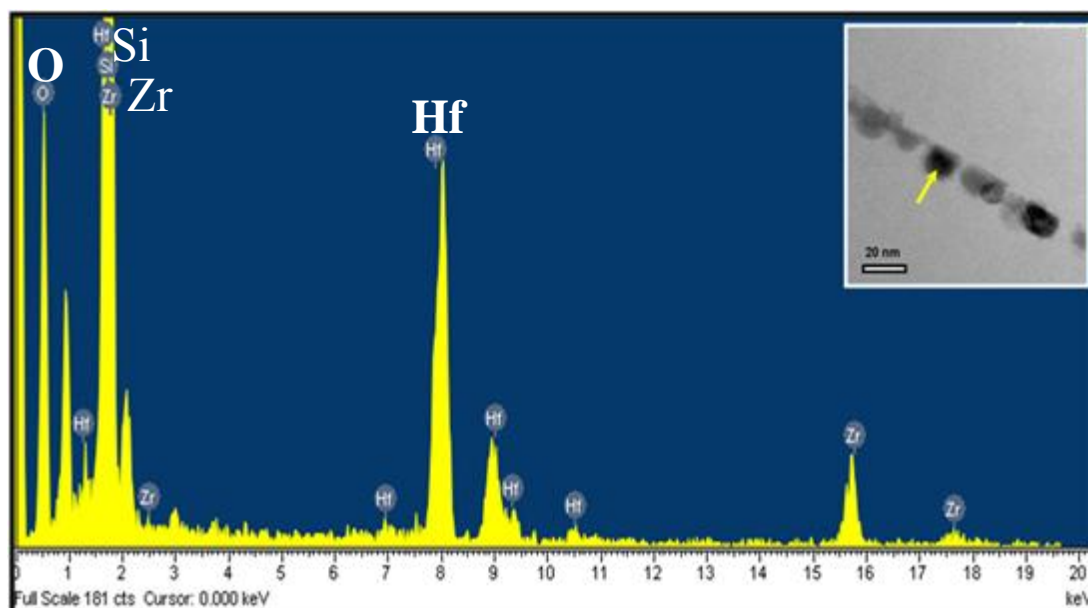


Fig. 3.2 EDS spectra of the sol-gel derived nanocrystals.

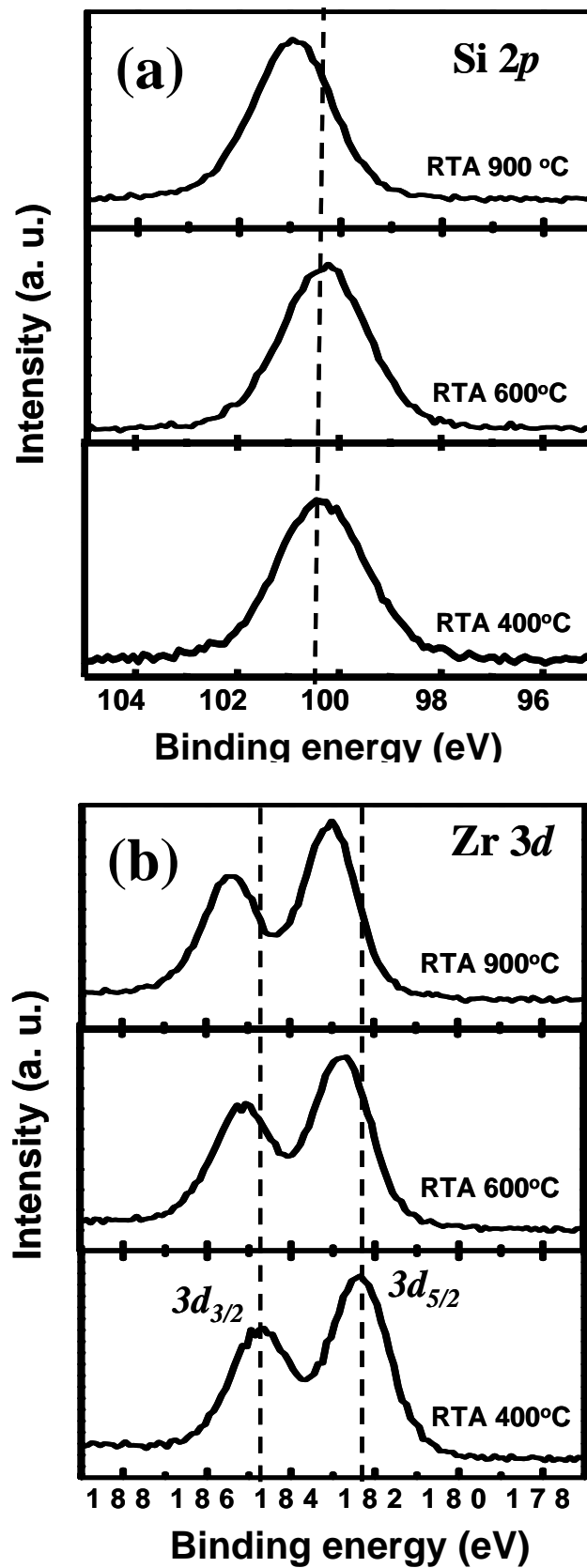


Fig 3.3(a) Si 2*p*, and (b) Zr 3*d* XPS spectra of the sol-gel thin films after different annealing temperatures.

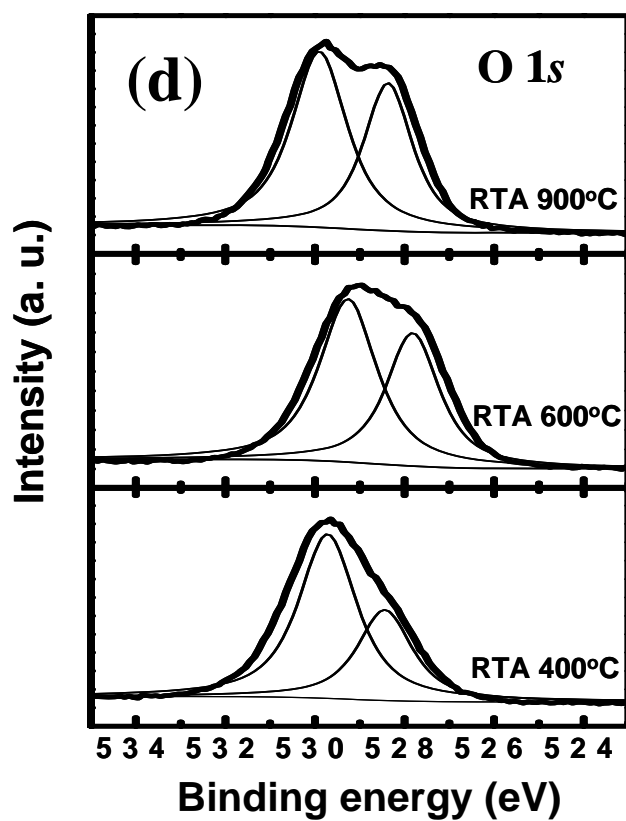
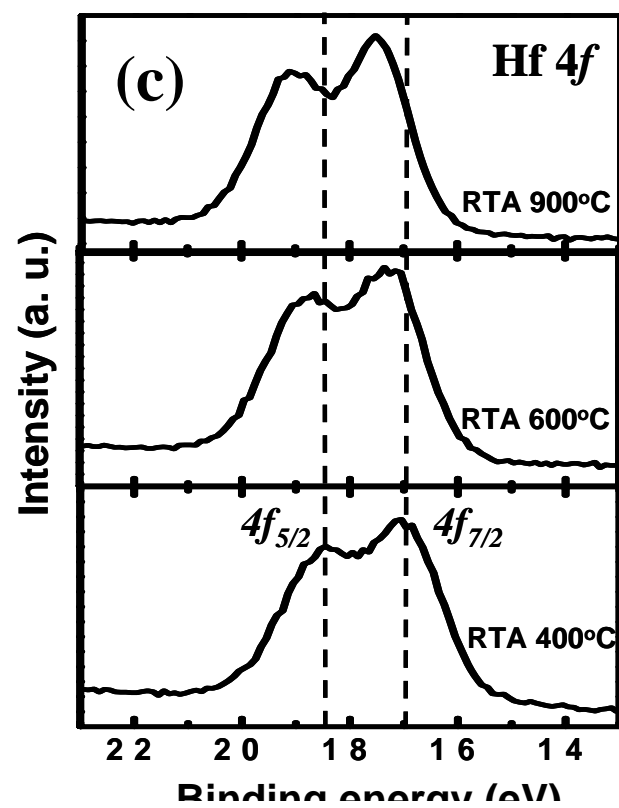


Fig 3.3 (c) Hf 4f, and (d) O 1s XPS spectra of the sol-gel thin films after different annealing temperatures.

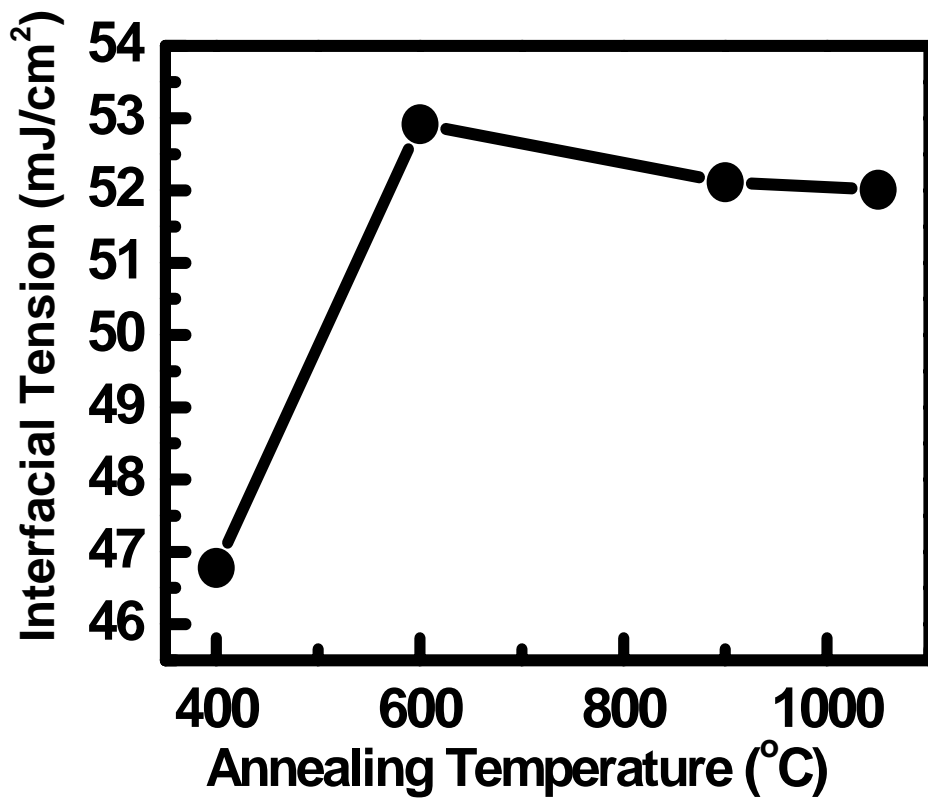


Fig. 3.4 Interfacial tension of the sol-gel thin film as a function of annealing temperature.

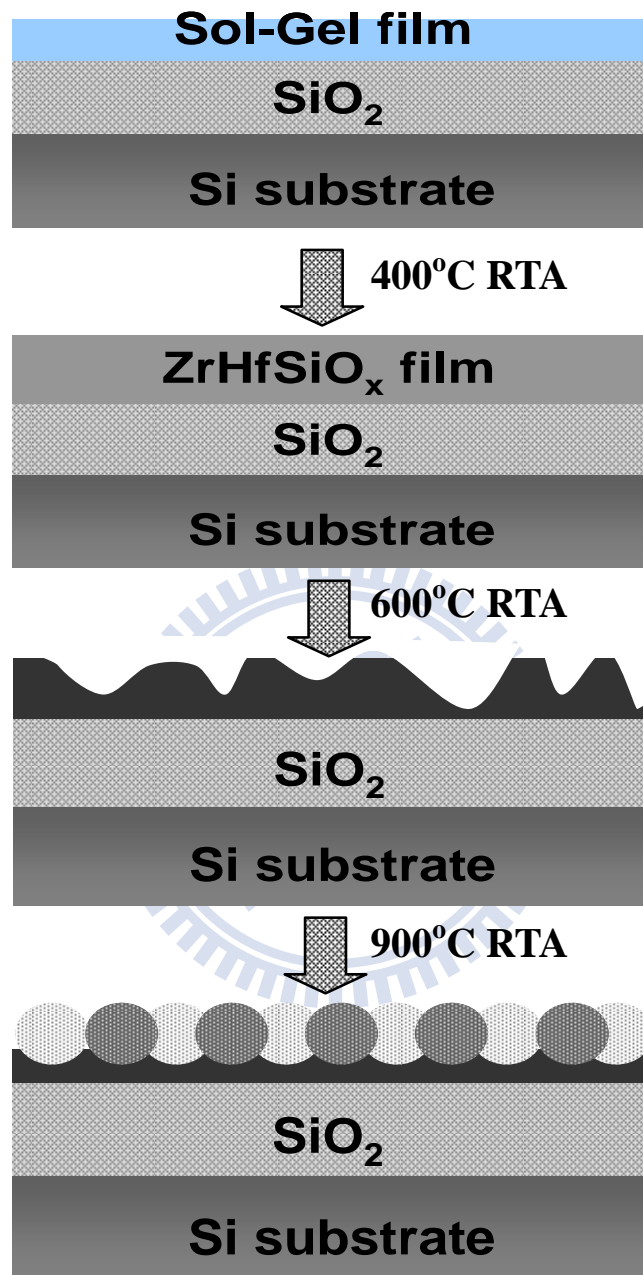


Fig. 3.5 Transformation processes of the sol-gel thin film into NC after different annealing temperatures

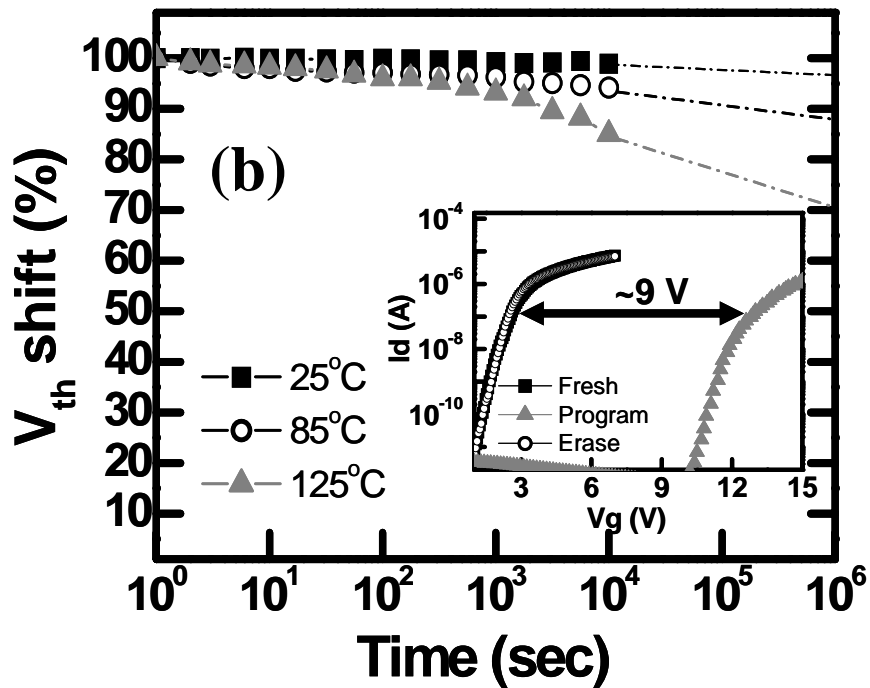
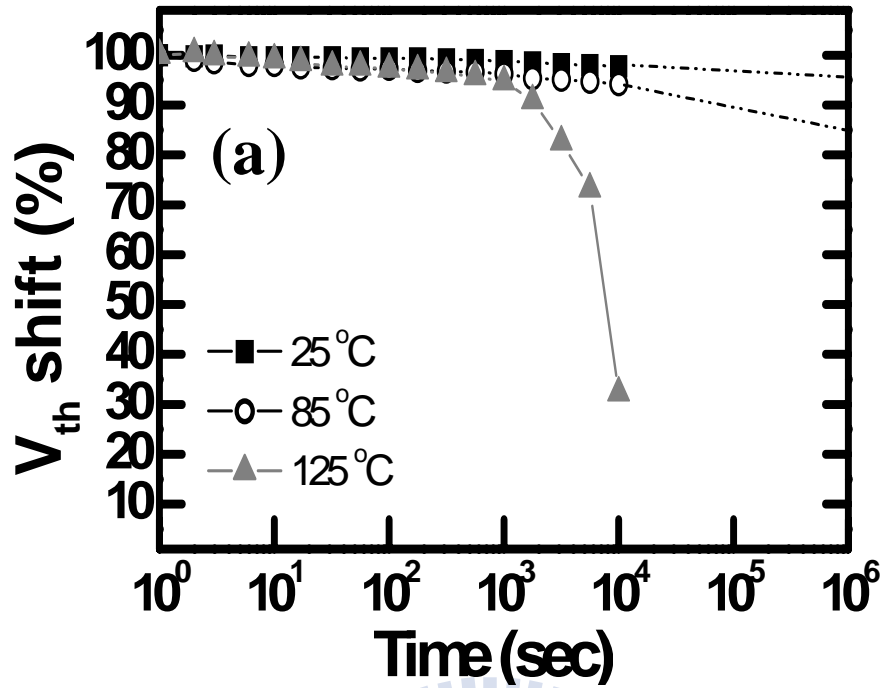


Fig 3.6 Retention characteristics of the NC memories annealed at (a) 600 and (b) 900°C at measurement temperatures of 25, 85, and 125°C. Inset of Fig. 4(b): the I_D - V_G curves of the NC memory in the programmed/erased state.

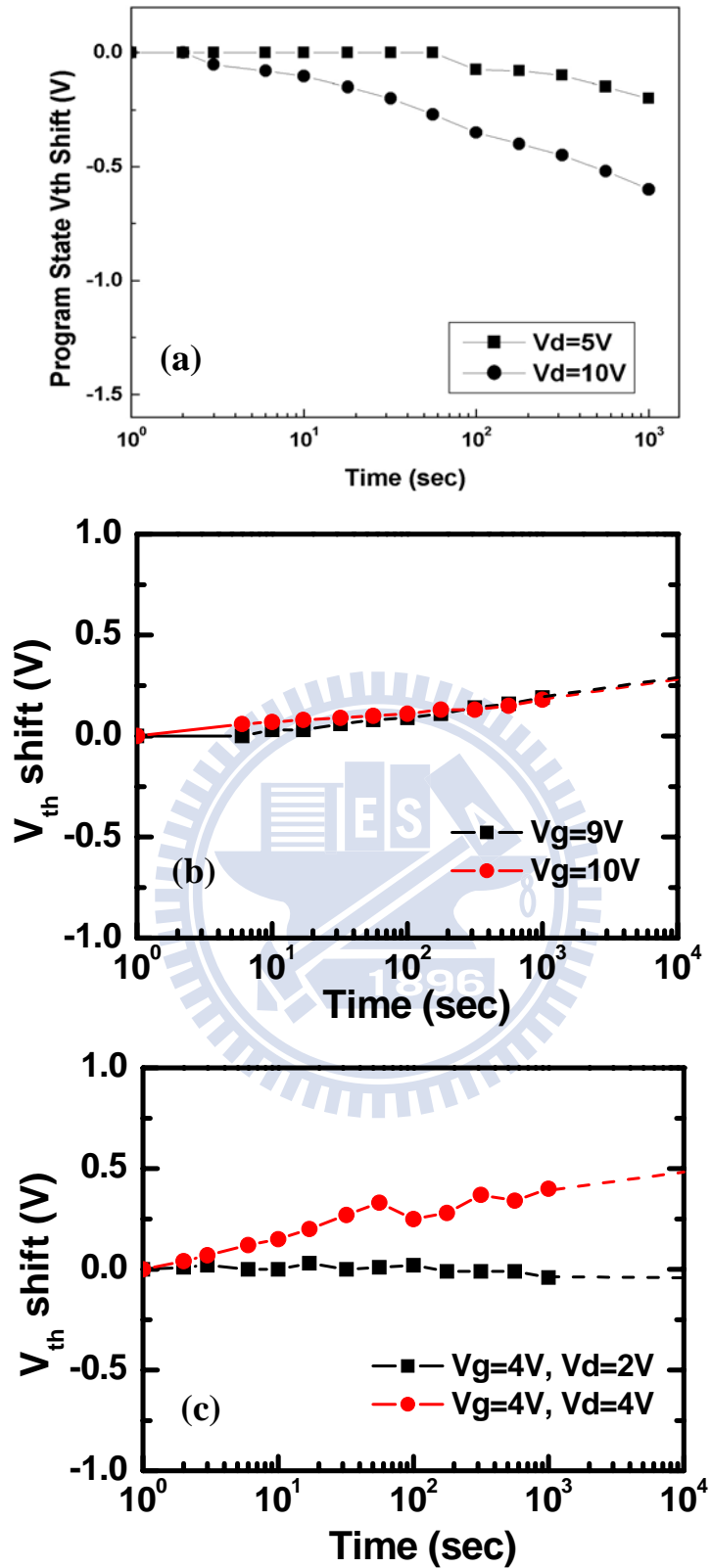


Fig. 3.7 Disturbance characteristics of the 900°C annealed NC memory. (a) Drain disturbance, (b) Gate disturbance, and (c) Read disturbance.

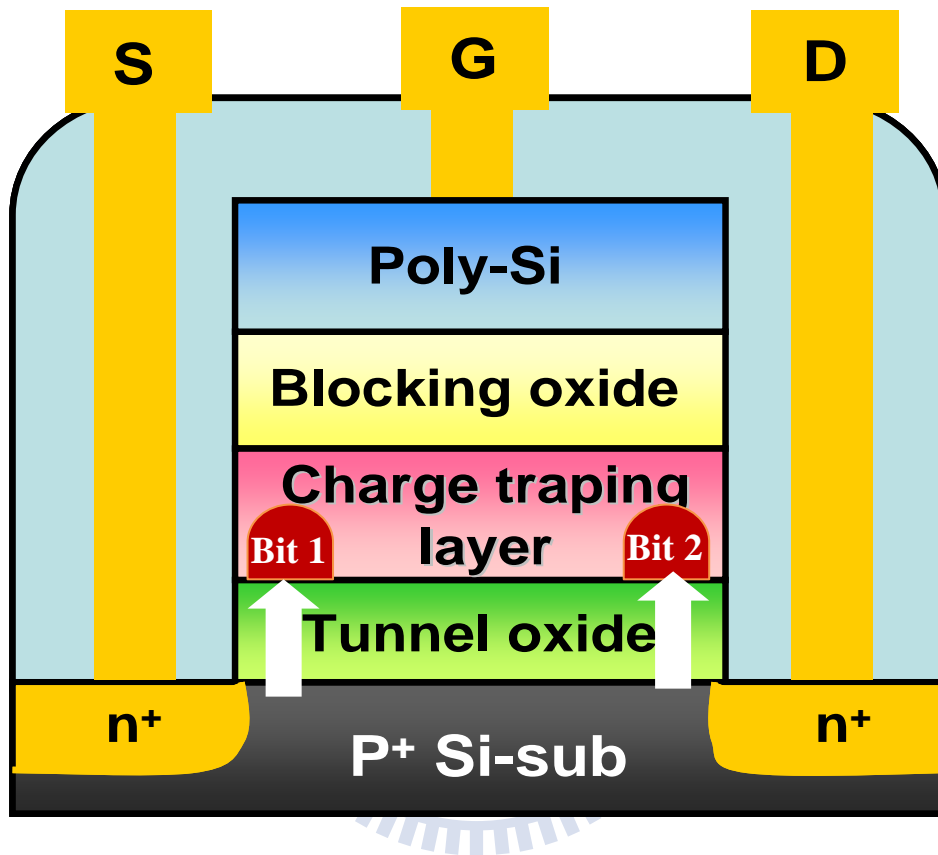


Fig. 3.8 Schematic diagram of the NC memory at 2-bit operation.

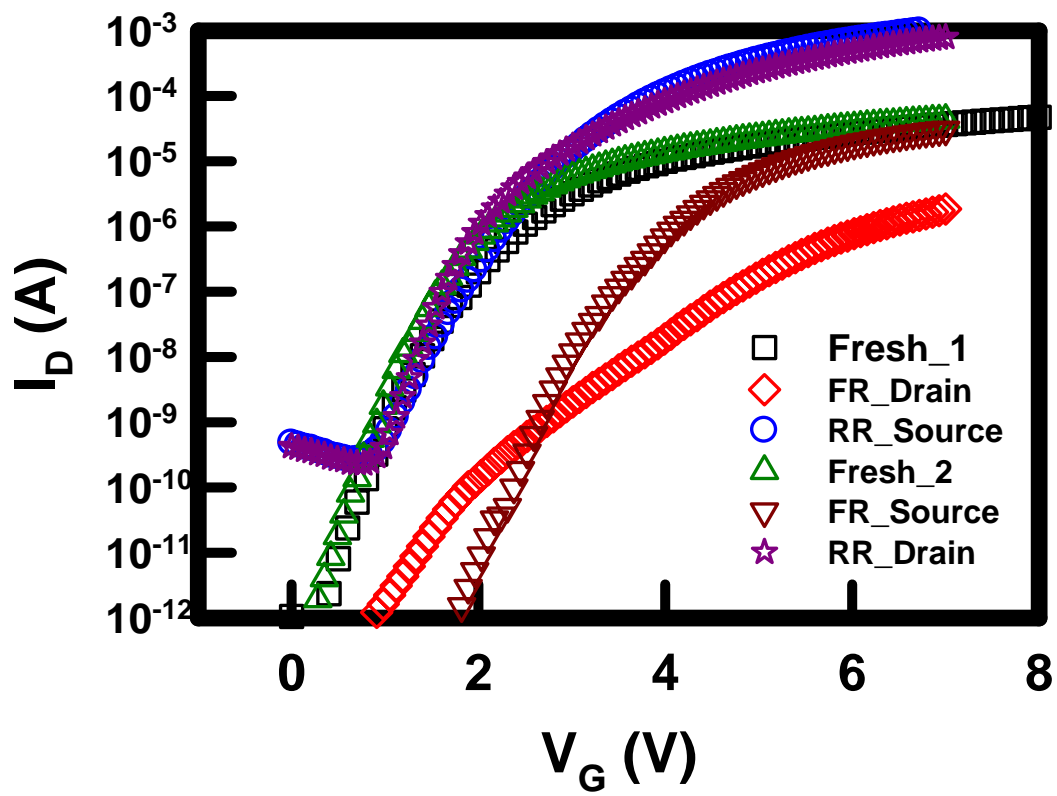


Fig 3.9 electrical characteristic of the NC memory at 2-bit operation.

Table 3.1 Dependence of viscosity and film thickness as a function of compositional molar ratio of sol-gel solutions.

Composition of precursor	Concentration (in molar ratio)	Viscosity (cP)	Thickness (nm)
ZrCl₄+HfCl₄+SiCl₄+Ethanol	1:1:1:1000	1.15	2.0
ZrCl₄+HfCl₄+SiCl₄+Ethanol	1:1:1:500	1.19	2.0
ZrCl₄+HfCl₄+SiCl₄+Ethanol	1:1:1:100	1.47	2.3
ZrCl₄+HfCl₄+SiCl₄+IPA	1:1:1:1000	2.45	3.2
ZrCl₄+HfCl₄+SiCl₄+IPA	1:1:1:500	precipitate	—
ZrCl₄+HfCl₄+SiCl₄+IPA	1:1:1:100	precipitate	—

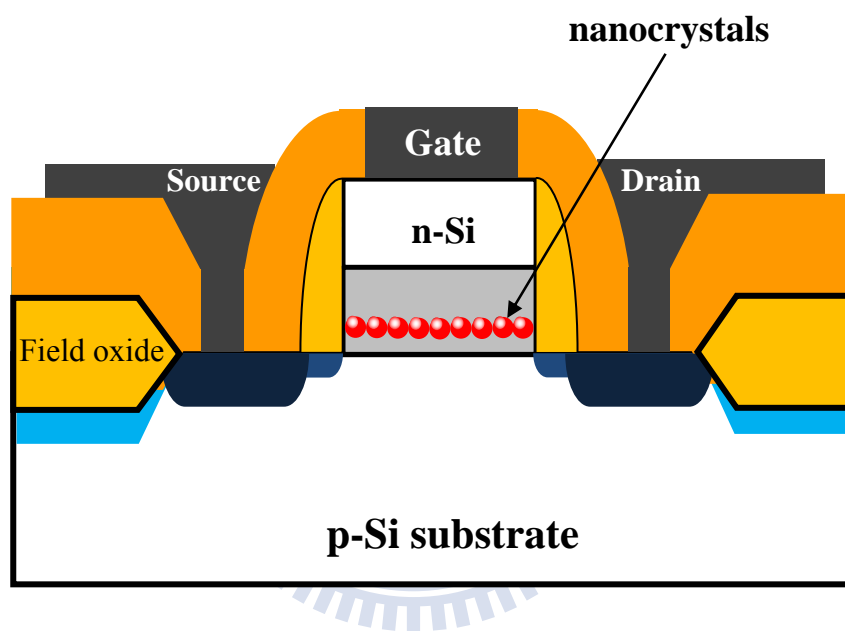


Fig. 3.10 Schematic diagram of the device structure for the spin coating charge trapping film/nanocrystal memories.

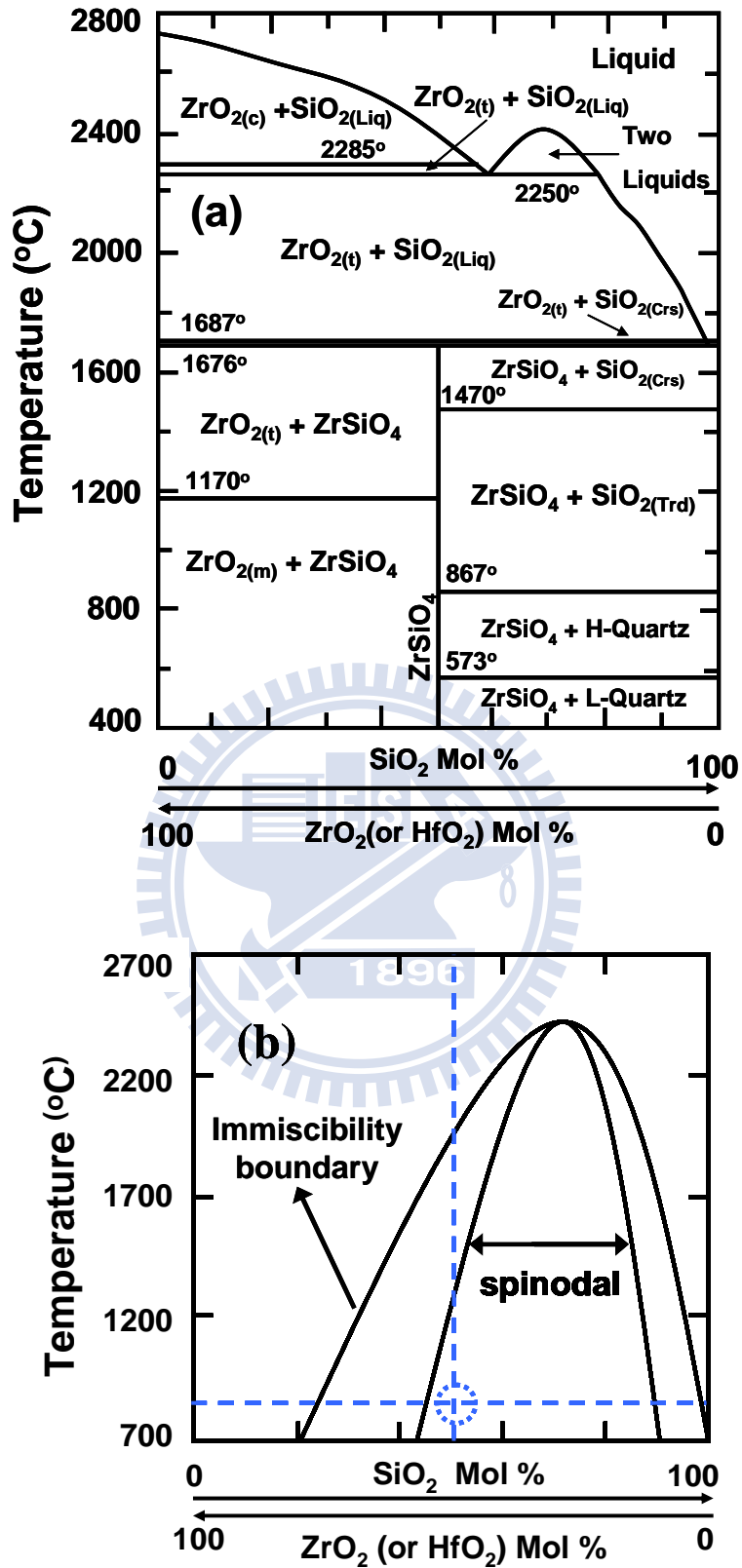


Fig. 3.11 (a) The pseudo-binary ZrO₂-SiO₂ phase diagram. (b) The metastable extensions of the liquid miscibility gap and spinodals to lower temperatures in ZrO₂-SiO₂.

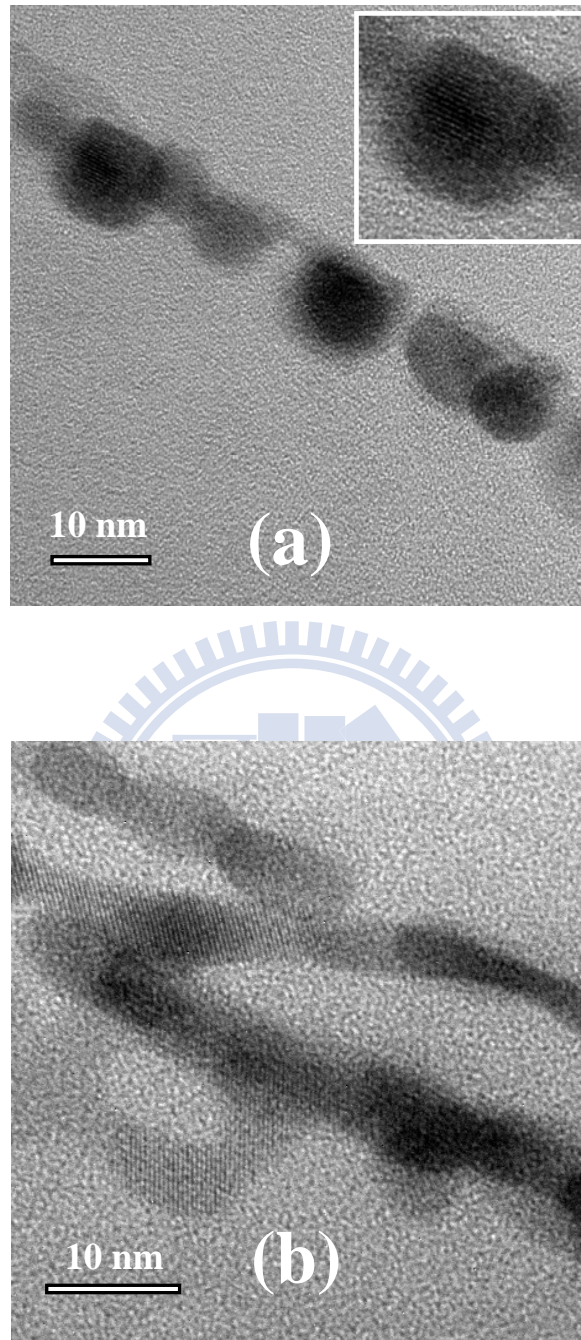


Fig. 3.12 Cross-sectional TEM images for the morphology from (a) ethanol system (inset: lattice fringe of nanocrystal), and (b) IPA system.

(a)

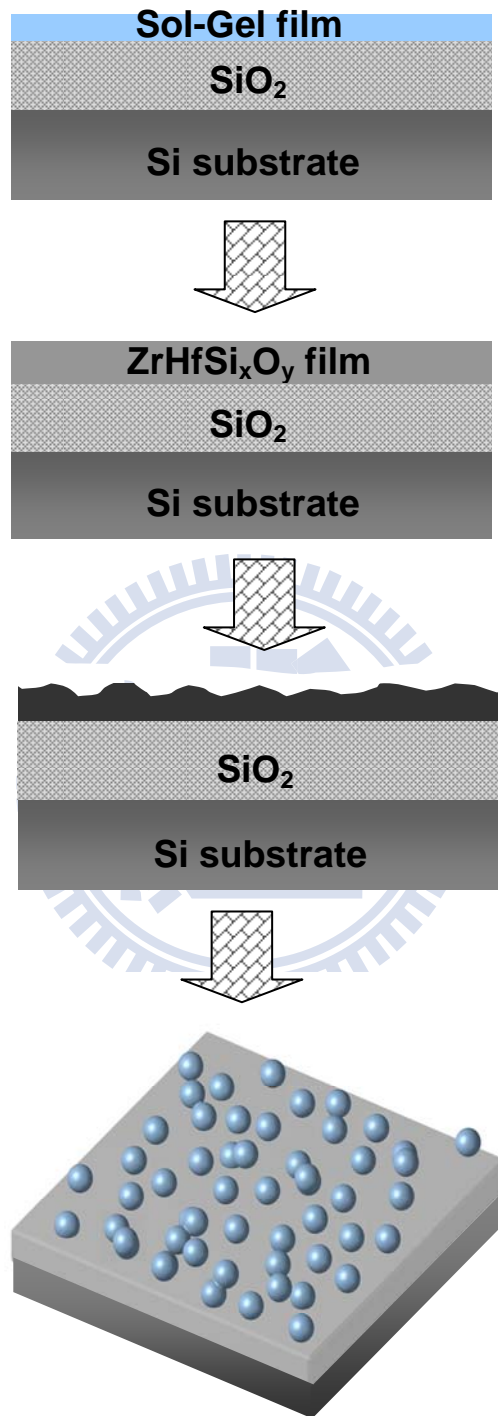


Fig. 3.13(a) Phase separation diagram of the sol-gel-derived film from ethanol system.

(b)

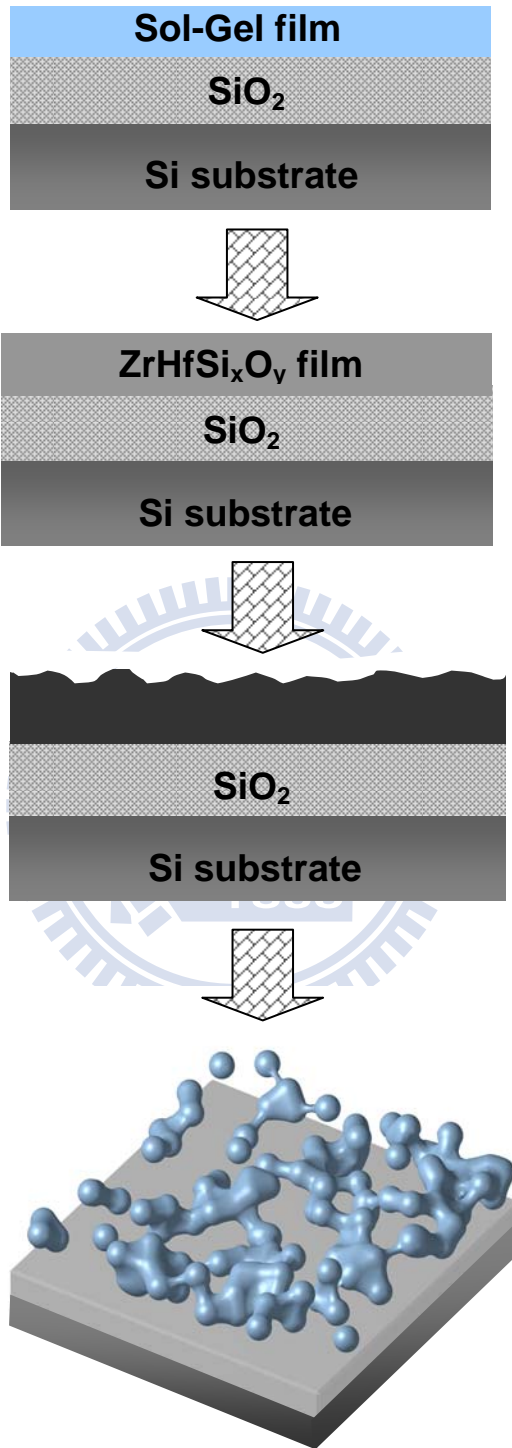


Fig. 3.13(b) Phase separation diagram of the sol-gel-derived film from IPA system.

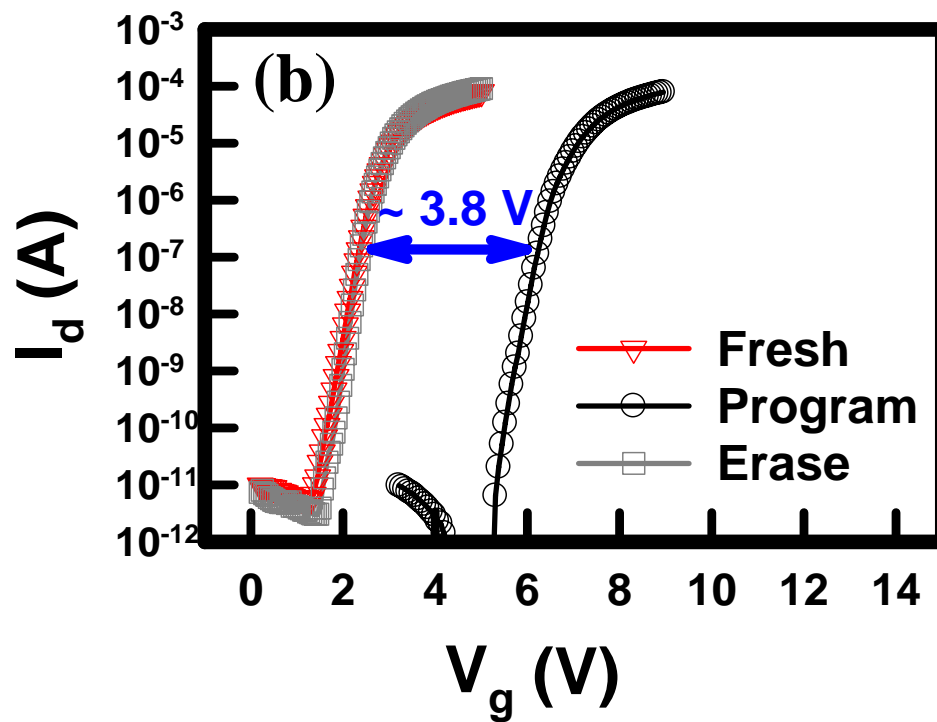
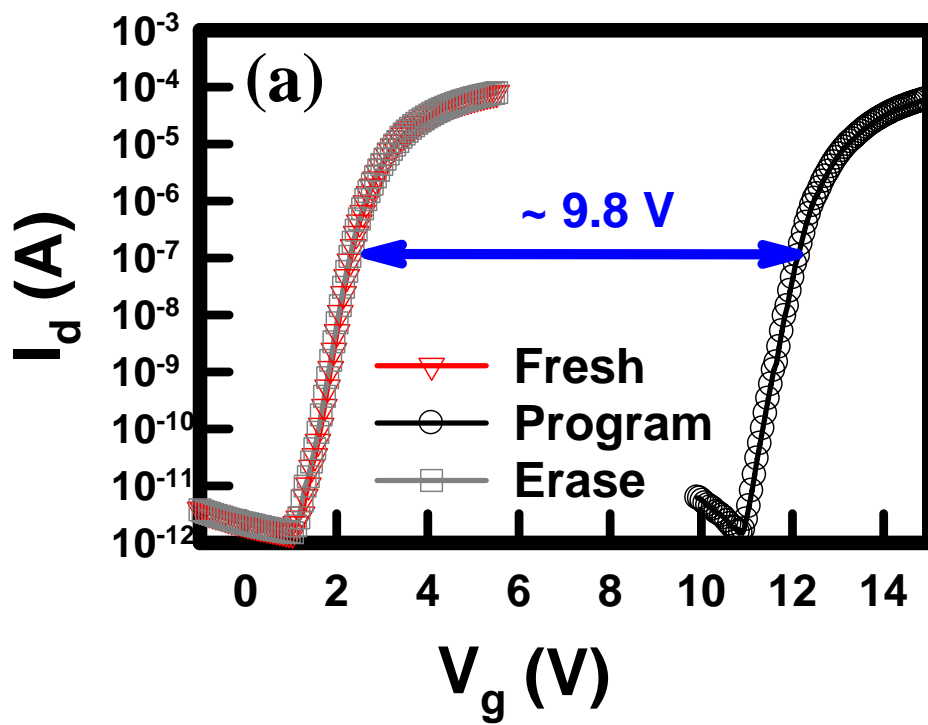


Fig. 3.14 I_D - V_G characteristics of the NC memories in (a) ethanol system, and (b) IPA system at fresh, program, and erase state, respectively.

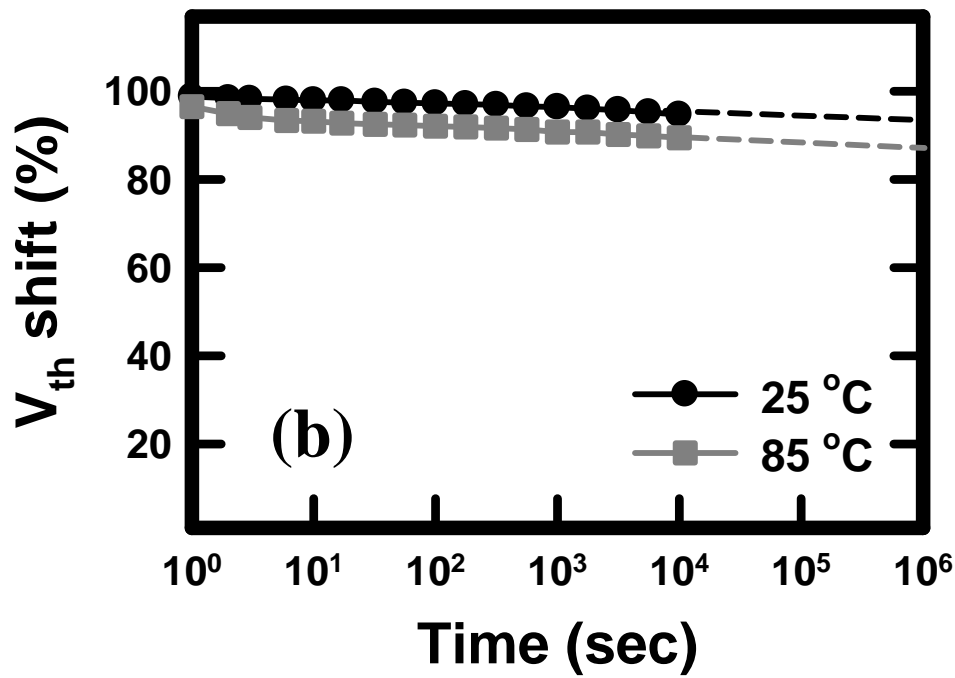
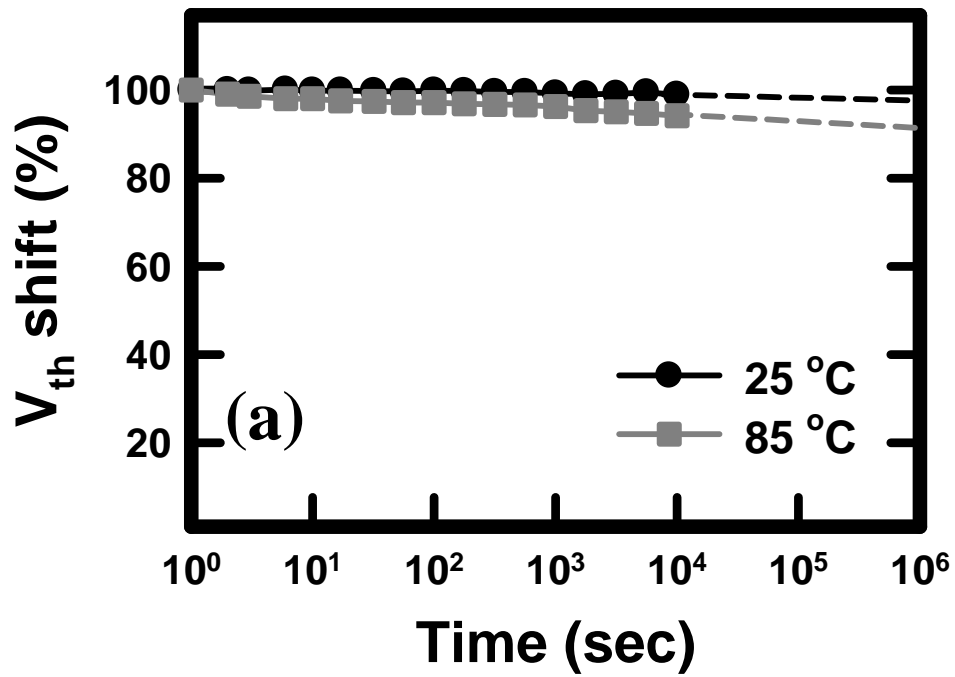


Fig. 3.15 Charge retention characteristics of the NC memories in (a) ethanol system, and (b) IPA system at measurement temperatures of 25 and 85°C.

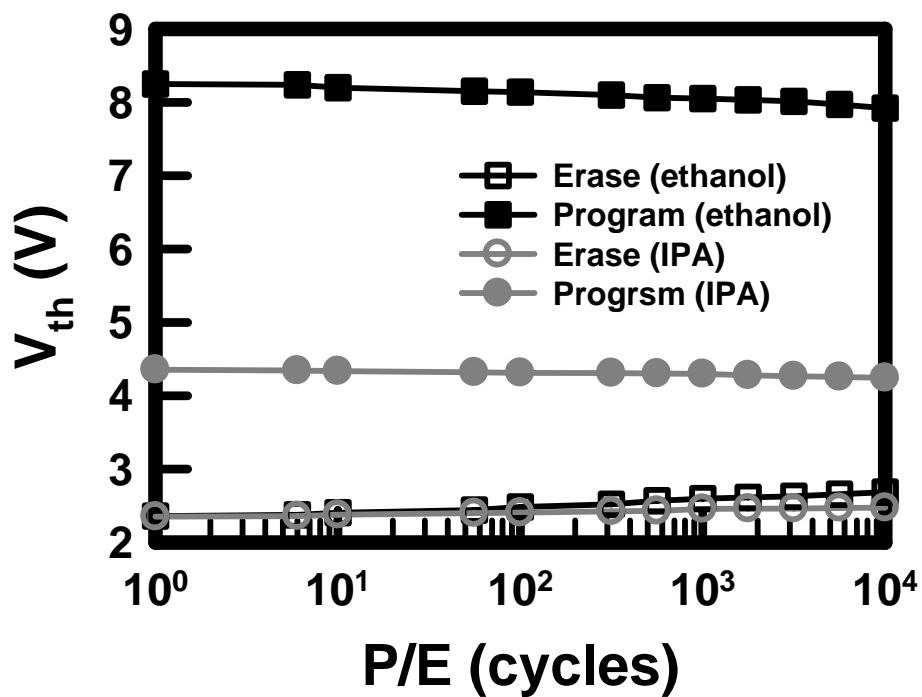


Fig. 3.16 Endurance characteristics of the NC memories in ethanol and IPA system, respectively. The measured condition for programming is : $V_G = 10$ V, $V_D = 10$ V, 10 ms, and erasing is: $V_G = -6$ V, $V_D = 10$ V, 10 ms.

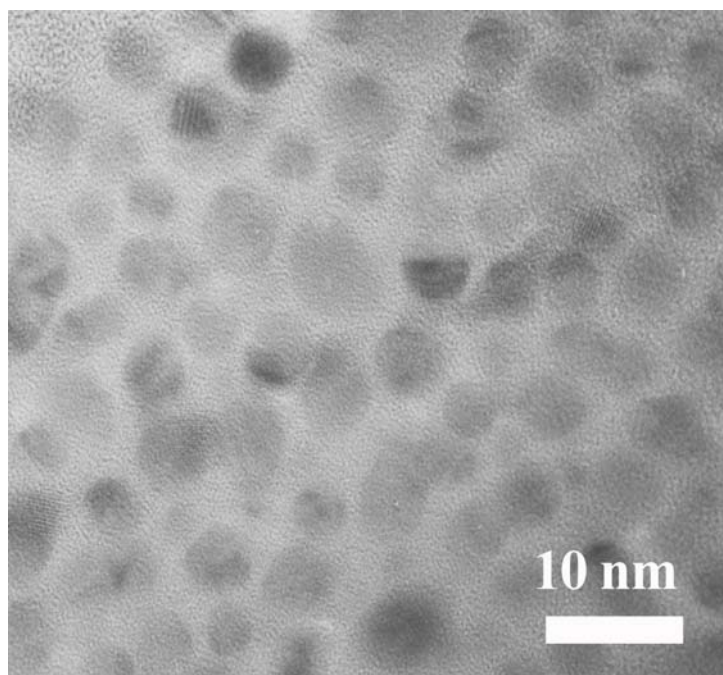


Fig. 3.17 Plan-view TEM image of the sol-gel derived NC.

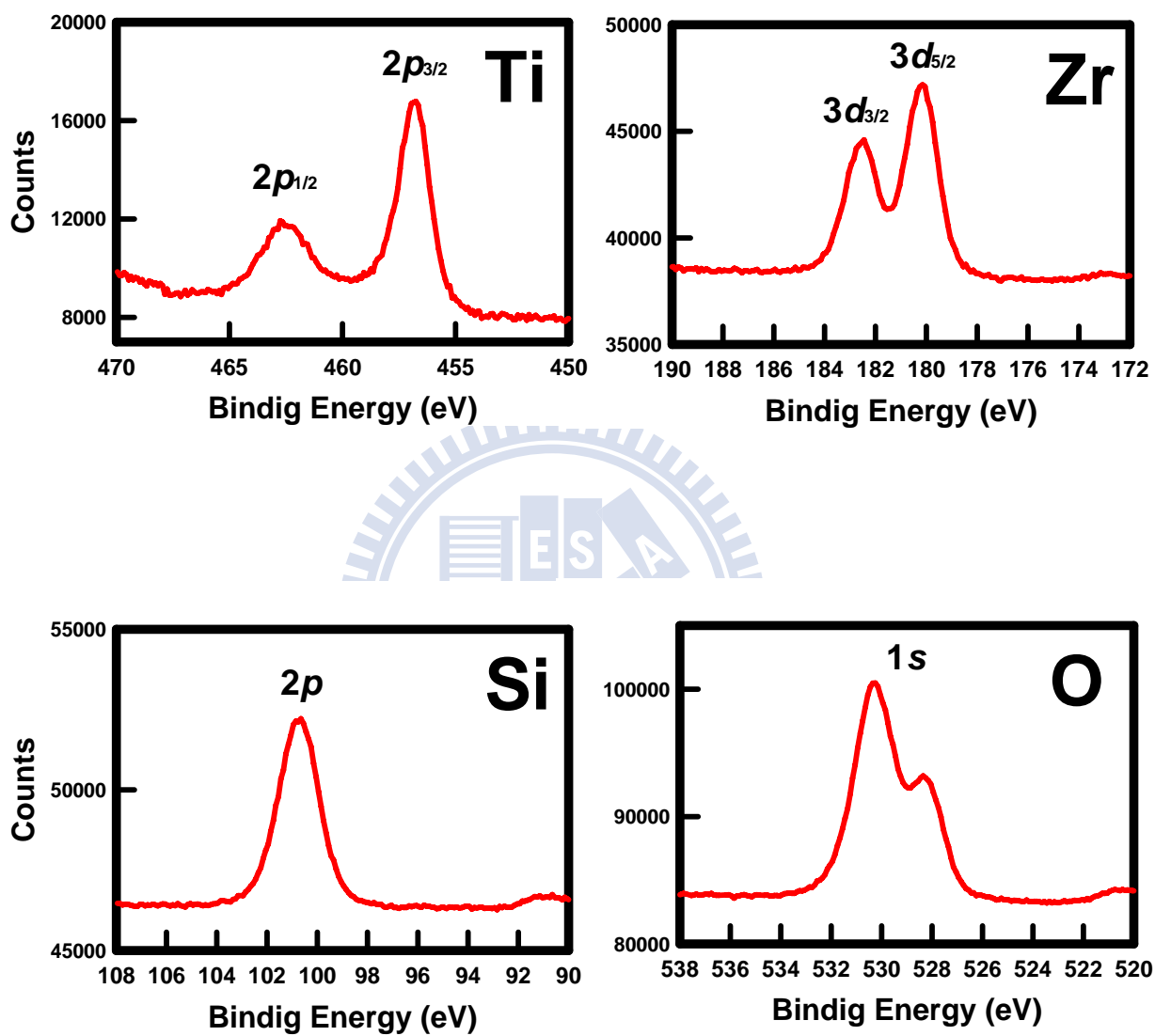


Fig. 3.18 (a) Ti 2p, (b) Zr 3d, (c) Si 2p, and (d) O 1s XPS spectra of the sol-gel derived $\text{Ti}_x\text{Zr}_y\text{Si}_z\text{O}$ nanocrystals.

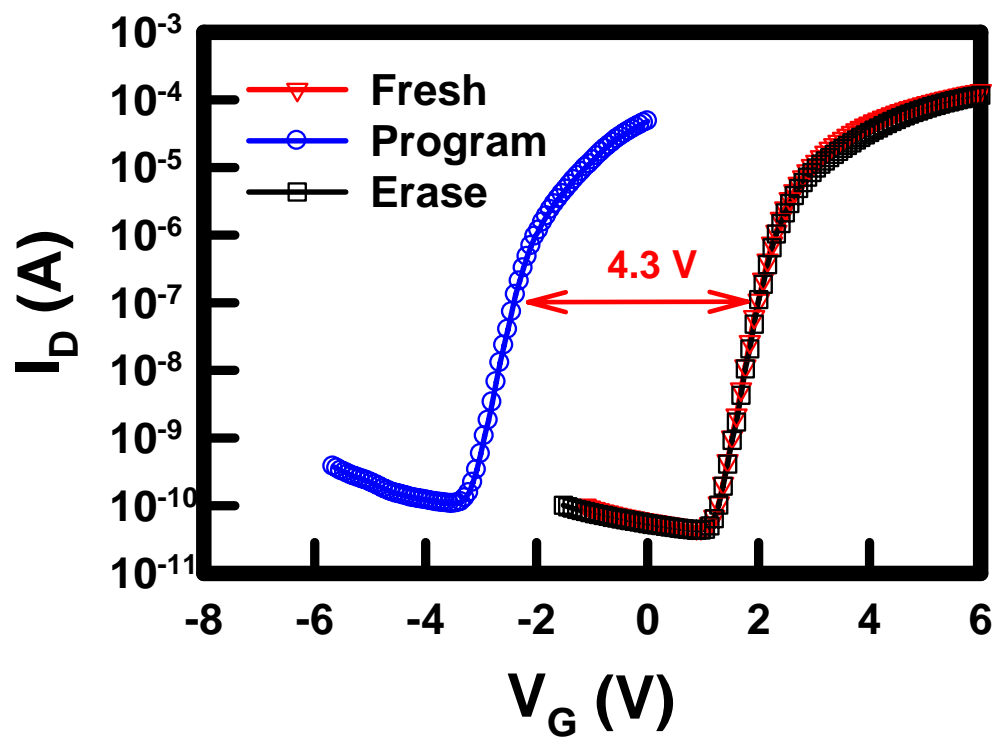


Fig. 3.19 I_D - V_G characteristics of the NC memory at fresh, program, and erase state, respectively.

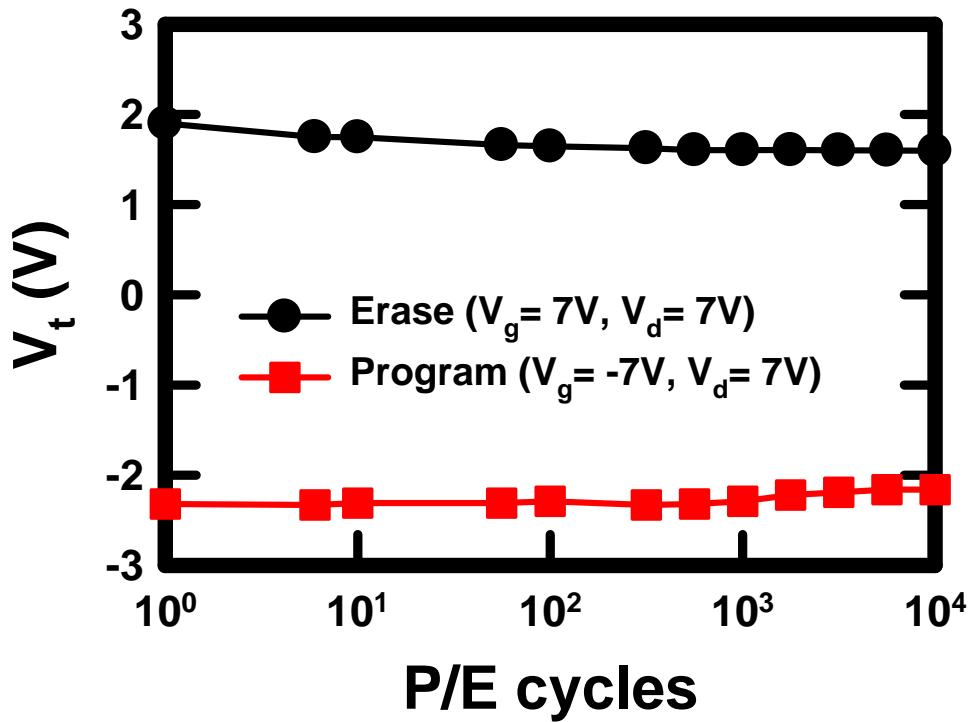
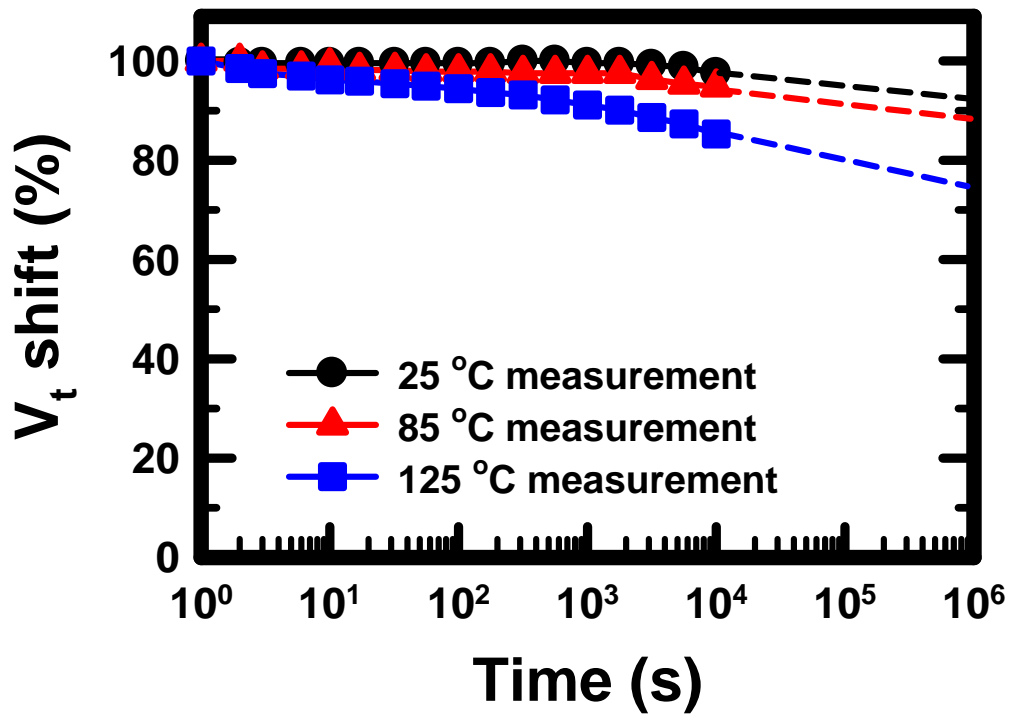


Fig. 3.20 (a) Retention characteristics of the NC memories at measurement temperatures of 25, 85, and 125°C. (b) Endurance characteristic of the nanocrystal memory device.

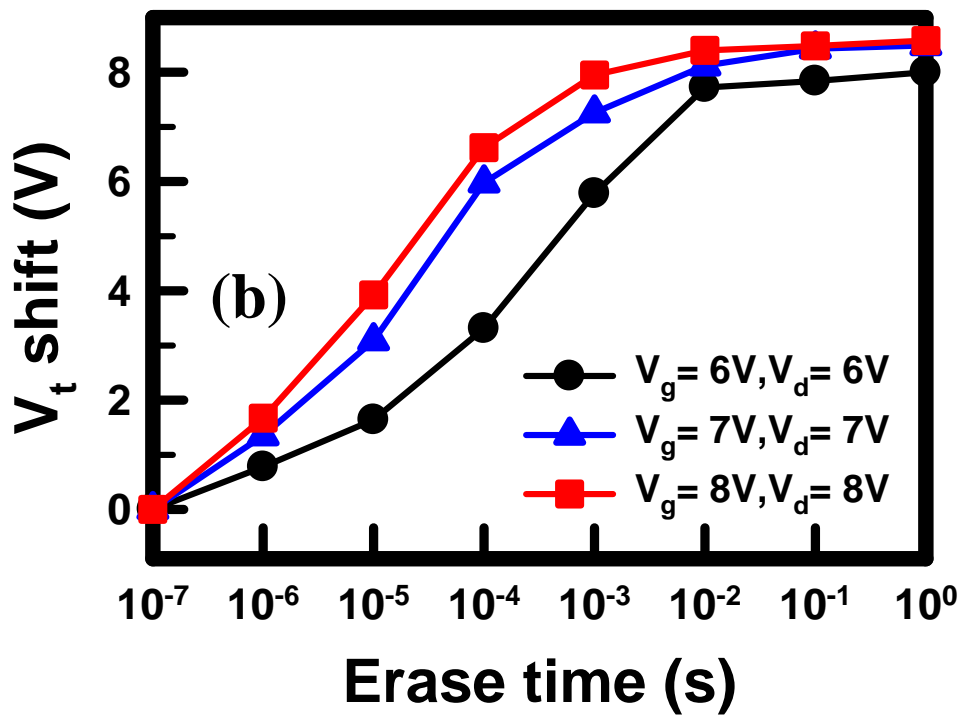
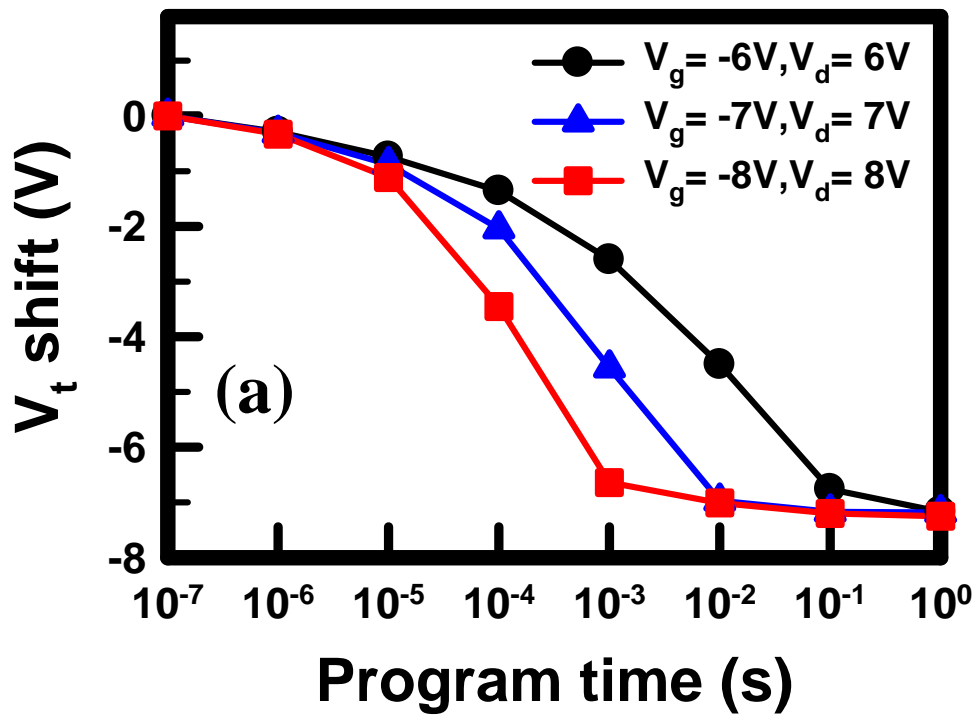


Fig. 3.21 (a) Program and (b) erase characteristics of the nanocrystal memory device under different conditions.

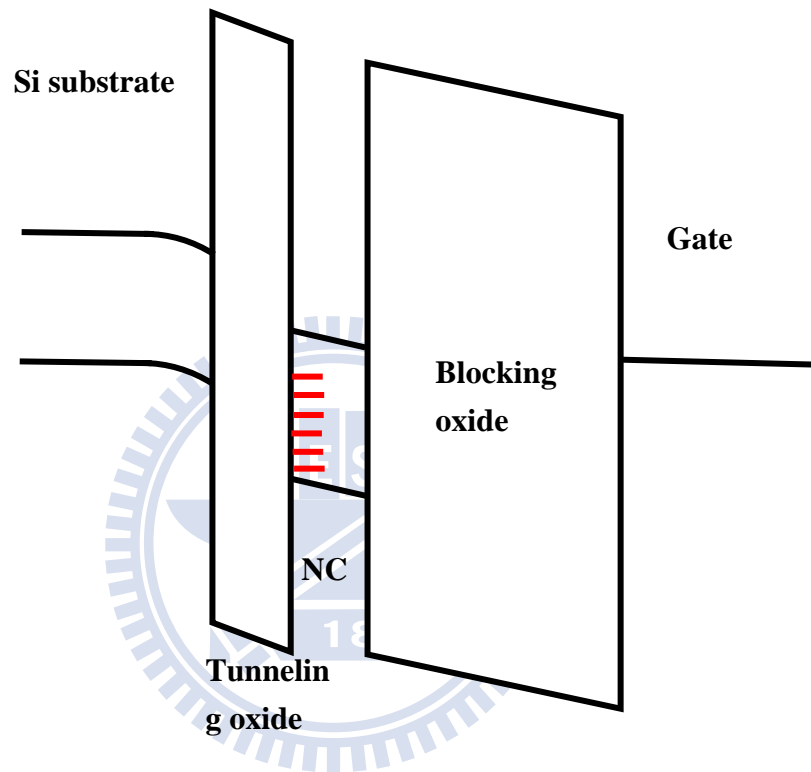


Fig. 3.22 Inferential energy band diagram of the sol-gel derived $Ti_xZr_ySi_zO$ NC memory under thermal-equilibrium.

Chapter 4

Research on the real-time, label-free and ultrasensitive nanowire and nanobelt FET biosensors for cancer marker analysis

4.1 Introduction

Ultrasensitive assays for biological and chemical species are fundamental requirements for the screening and detection of disease, as well as for the discovery of new drugs. There is increasing demand for ultrasensitive gene detection systems that allow the early detection of genetic disorders, thereby improving preventative health care. Many of these disorders are caused by in-cell mutations of double-stranded deoxyribonucleic acid (dsDNA), the blueprint of our genetic makeup. Double-stranded DNA comprises pairs of single-stranded DNA (ssDNA) bonded together to form the well-known DNA double helix. Hence, the detection of specific sequences of ssDNA and knowledge of the base pair composition are important aspects of the diagnoses of genetic disorders.

The most widespread technique for assaying DNA samples employs the polymerase chain reaction (PCR) to amplify a DNA fragment or sequence of interest through enzymatic replication [1-2]. PCR has become a common technique in

biological and medical research laboratories for such tasks as the sequencing of genes, the detection and diagnoses of infectious diseases, the identification of genetic fingerprints, and the creation of transgenic organisms [3]. The drawbacks of such assays include the need for a fluorescent label and the great length of time required to amplify trace DNA concentrations. Higher-sensitivity, label-free sensing devices are desired as replacements for the time-consuming, label-based assays [4].

One-dimensional nanowires [5-9] are particularly appealing candidates for use in ultrasensitive miniaturized biomolecule sensors. Nanowire field-effect transistors (NWFETs) can suppress the short-channel effects encountered in nanoscale metal oxide semiconductor field-effect transistors and provide high surface sensitivity [10]. Unlike the signal responses of conventional electrochemical cells operate based on the Nernst equation [11], the response of NWFETs featuring surface-immobilized molecules from the fluid is more complex. Recently, Nair and Alam [12] derived a logarithmic relationship between the target molecular concentration and the electrical signal for an NWFET functioning based on the diffusion–capture model and the Poisson–Boltzmann equation.

Silicon NWFETs have been fabricated using both “top down” and “bottom up” methods [13]. The “bottom up” fabrication methods usually involve the formation of NWs through vapor–liquid–solid (VLS) growth [14], which is limited by the need for

complex integration techniques that require precise transfer and positioning of individual NWs to provide reliable and superior ohmic contacts. In addition, control over the doping concentrations in self-assembled semiconducting nanostructures remains a great challenge, as is the fabrication of high-density sensor arrays. Furthermore, the use of an additional external gate—to precisely turn the NWFET sensor to higher sensitivity—is also critical [5,7,15]. The “top down” methods for fabricating NWs usually employ the advanced lithography techniques used in the semiconductor industry, allowing mass-production with reduced fabrication costs [16]. The excellent device performance and good ohmic contacts of such methods enable the possibility of integration.

In this chapter, ultrasensitive FET biosensor was fabricated for cancer marker analysis. In section 4.2, a single crystalline silicon nanowire FET biosensor with a critical 60-nm in width was fabricated. The Si NWFET allowed detection of the hybridization and de-hybridization for BRAF^{V599E} mutation gene from a cancer cell, as well as the ability to distinguish the complementary and mismatched target DNAs. In section 4.3, an novel silicon nanobelt FET process was proposed by using the LOCOS isolation process and CMOS-compatible technology. We used the NB FET as the ultrasensitive and real-time biosensor to analysis the hepatocellular carcinoma.

To avoid the false positive issue, the alpha-fetoprotein cancer marker, hepatitis B virus *x* gene fragment, and solution pH were detected by our NB FET.

4.2 A silicon NWFET biosensor to detect a gene mutation

In this section, we used conventional complementary metal-oxide semiconductor technology to develop a 60-nm-wide Si NWFET that enables the sensing of mutated genes. We first evaluated various cleaning solutions for their use in improving the immobilization of DNA onto the silicon dioxide (SiO₂) surfaces, in terms of the fluorescence efficiency and the electrical properties of the sensors. We then applied the NWFET sensor as an ultrahigh-sensitivity molecular probe for the detection of a cancer-related BRAF^{V599E} mutation gene.

It has been reported that the presence of BRAF^{V599E} mutation genes correlates to the occurrence of melanomas, colorectal cancers, gliomas, lung cancers, sarcomas, ovarian carcinomas, breast cancers, papillary thyroid carcinomas, and liver cancers [17-18]. This mutation is believed to mimic phosphorylation in the activation segment by insertion of an acidic residue close to a site of regulated phosphorylation at serine 598. BRAF^{V599E} exhibits elevated basal kinase activity and diminished responsiveness toward oncogenic stimulation. BRAF^{V599E} also transforms NIH3T3 cells (murine embryonic fibroblasts) with higher efficiency than does the wild-type form of the

kinase, consistent with the functioning as an oncogene [19]. Therefore, characterization of the BRAF^{V599E} mutation genes at the molecular level is significant for early tumor identification, allowing the possibility of aggressive and specific therapy to save human lives.

4.2.1 Fabrication of NWFET sensors

A commercially available 6-in. (100) silicon-on-insulator (SOI) wafer, which possessed 50-nm-thick intrinsic silicon and 150-nm-thick buried oxide, was served as the device substrate [Fig. 4.1(a)]. The detailed fabrication procedures for the back-gated NWFET sensor were mentioned below. The critical silicon NWs having a width of 60 nm and length of 2 μm were defined using a 40-keV electron beam (EB) lithography and dry etching system [Fig. 4.1(b)]. After removal of EB resist, a thin layer of SiO₂ film (10 nm) was then deposited by low-pressure chemical vapor deposition (LPCVD). Again, the EB photoresist (PR) was spin-coated onto the surface. Prior to ion implantation, the PR on the region of defining the source/drain areas was removed by EB lithography. Arsenic ion beam (As⁺) was then implanted with a dosage of $5 \times 10^{15} \text{ cm}^{-2}$ at an acceleration energy of 20 keV. Backside of the sample was also boron-implanted at 100 keV with $5 \times 10^{15} \text{ cm}^{-2}$ dosage. After PR removing, rapid thermal annealing (RTA) was performed at 1050°C for 30 s in a

nitrogen ambient to activate the carriers [Fig. 4.1(c)]. Prior to defining the contact pad region through lithography and wet etching (80% phosphoric acid, 5% nitric acid, 5% acetic acid, and 10% de-ionized water; by volume), a 500-nm-thick Al-Si-Cu (Al: 98.5%; Si: 1%; Cu: 0.5%; by weight) alloy was formed using a sputter system [Fig. 4.1(d)]. After PR removal, 50-nm-thick SiO₂ and 10-nm-thick silicon nitride (Si₃N₄) layers were sequentially deposited through plasma-enhanced chemical vapor deposition (PECVD) at 300°C to passivate the nanowire's surface. Then, the EB lithography was used to open the NWFET's detection region for sensing purpose. The region was sequentially etched back by plasma etch (for Si₃N₄) and diluted buffer oxide etching solution (BOE for SiO₂, NH₄F : HF : de-ionized water = 42: 7 : 1). The PR was then removed by H₂SO₄ and H₂O₂ mixture (3:1; denoted "piranha"), and the schematic diagram was indicated in Fig. 4.1(e). Then, only the backside surface was dipped and etched by BOE solution in a pipette. Finally, a 500-nm-thick Al-Si-Cu pad was deposited by sputter system. A cross-sectional representation of the NWFET with electrical connection for the detection of DNA molecules is presented in Fig. 4.1(f). Prior to the DNA immobilization, all the devices were preserved in clean room for at least one week to ensure the thickness saturation of native oxide.

4.2.2 Self-assembly of capture DNA on the NWFET device

Prior to immobilizing the DNA molecules, sensors were cleaned for 30 min using various solutions: (a) no cleaning (denoted “control”), (b) de-ionized water (denoted “DI”), (c) piranha, (d) 25% 2-propanol solution (denoted “IPA”), and (e) acetone and ethanol mixture (1:1; denoted “ACE”). The H₂SO₄, HCl, H₂O₂, and organic solvents used to clean the device surface were of analytical or higher grade (Merck, Darmstadt, Germany). High-purity DI water, purified through double deionization processes, was used throughout.

After performing the cleaning process, a monolayer of 30-mer ssDNA (capture DNA, Blossom Biotechnologies, Taipei, Taiwan) molecules was then immobilized onto the NWFET surface. The surface reactions occurred with the silanol groups present on the silicon NW surface as a result of silicon oxide formation. Because silanol groups are good proton donors (H⁺) and acceptors (SiO⁻), (3-aminopropyl)triethoxysilane (APTES) was employed to self-assemble a monolayer of DNA onto the surface of the NW detection region. Fig. 4.2 illustrates the procedure used to immobilize the DNA strands onto the surface-bounded APTES units. Initially, the samples were immersed into 10% APTES aqueous solution for 30 min at 37°C and adjusted to pH 3.5 with 1 M HCl. The samples were then rinsed with DI water and dried on a hot plate (120°C for 30 min). At this stage, amino groups were presented as terminal units from the surface. Next, glutaraldehyde was linked to the

amino groups to present aldehyde groups from the surface; the sample was immersed in the linker solution [2.5% glutaraldehyde (1,5-pentanedial)] for 30 min at room temperature and then rinsed with phosphate-buffered saline (PBS; 120 mM NaCl, 2.7 mM KCl, and 10 mM phosphate buffer; pH 7.4; Sigma–Aldrich) solution [20]. The 2.5% glutaraldehyde solution [21-22] was formed by diluting 25% glutaraldehyde (Sigma–Aldrich) with PBS solution. Next, the selective immobilization technique was used to bind the terminal 3'-amino group of the oligonucleotide to the aldehyde groups on the NW surface [23]. A fresh solution of synthetic 1 μ M capture DNA (Blossom Biotechnologies, Taipei, Taiwan) was diluted with PBS buffer to provide a 10 nM solution of capture DNA. A drop (100 μ L) of this capture DNA solution was placed onto the NWs and reacted for 1 h to ensure effective immobilization. The un-reacted aldehyde groups were blocked through reactions with ethanolamine (Sigma–Aldrich), washed with PBS buffer, and subsequently dried under ambient nitrogen.

To monitor the efficient immobilization of the capture DNA, a fluorescently labeled capture DNA sample (Blossom Biotechnologies, Taipei, Taiwan) was also prepared. The fluorescent unit was derived from fluorescein isothiocyanate (FITC), which reacted specifically at the 5' end of the capture DNA. Green fluorescence

images (excitation: 494 nm; emission: 520 nm) were observed using a BX51 fluorescence microscope (Olympus, PA, USA).

4.2.3 Target DNA hybridization and de-hybridization

After capture DNA immobilization, a strand of synthetic complementary DNA, namely the target DNA (Blossom Biotechnologies, Taipei, Taiwan), was applied to hybridize to the capture DNA on the NWFET surface. The sequence of the target DNA was complementary to that of the capture DNA. The 30-mer target DNA was diluted to various concentrations with PBS buffer solution. The target DNA was then injected into the microfluidic channel that ran through the NWFET detection region, followed by PBS washing to remove the excess target DNA. The electrical measurement of the NWFET sensor was performed to obtain the drain current (I_D) versus gate voltage (V_G) curve. To ensure successful hybridization, an FITC-labeled target DNA strand, with the fluorescent unit located at the 3' end, was also prepared.

The electrical properties of the NWFET biosensors were characterized using an Agilent-4156C semiconductor parameter analyzer (Agilent Technologies, CA). After measurement, the samples were washed with hot DI water (90°C) for 5 min to de-hybridize the complementary DNA pair. The resulting surface presenting only the capture DNA was then measured again.

4.2.4 Electrical performance of the NWFET

Fig. 4.3 presents plot of the I_D - V_G at drain voltages (V_D) of 0.1 and 1 V, respectively, for the fabricated 60-nm NWFET biosensor. The current flowing through the NW located between the source and drain electrodes could be switched “on” and “off” at various backside gate potentials. If, at a large negative gate bias (e.g., -15 V), the channel conduction (I_D) is very low, a positive voltage applied to the gate will create an n-channel (i.e., an electron carrier). Therefore, the sensor is a normally-on, n-channel depletion NWFET [24]. In general, a backside gate can apply a bias voltage to the NW and, thereby, affect the energy barrier for the charge carriers. This applied voltage ensures device operation under the optimal conditions of a larger current shift. Stern and co-workers [25] proposed a p-channel DNA sensor with a backside gate control design; the sub-threshold swing (SS) for their device was, however, about 1250 mV/decade ($I_D = 10^{-13}$ A and 10^{-9} A at -20 V and -25 V, respectively)—much higher than our value of 450 mV/decade. We attribute the high sensitivity of our DNA sensor to the use of the single crystal n-channel design rule having higher mobility and lower SS characteristic.

The turn-on/turn-off current ratio of this sensor was near six orders of magnitude when V_D was 0.1 V, suggesting improved practicality of the fabricated biosensors. The threshold voltage (V_t), which we determined for a drain current at 10^{-9} A, was ca. -10.8 V. The dependence of the value of I_D on the applied gate voltage implies that the fabricated NWFET sensors could be fine-tuned to optimal conditions to sense molecules that effect a change in the surface charge. A charged molecule bound onto an NW surface exerts an electric field in a manner similar to an applied gate voltage. For example, when the surface receptor contains a macromolecule of DNA bearing

negative charge, specific binding interactions will result in an increase in the NW's negative charge, and, hence, a shift to the right for the V_t in I_D-V_G curve of the NWFET biosensor [9].

4.2.5 Evaluating of cleaning efficiency through fluorescence imaging

The charge carriers in the NWs are affected by the presence of the immobilized biomolecule; therefore, the variation of their electrical signal can be used as the sensing indicator. If the surface of interest is covered by ambient contaminants, the detection region of the NW is blocked by the contaminants, which degrade the function of the sensor. Conventional bioassays described in the literature have been cleaned using piranha solution [26-27], even though it is not appropriate for sensor cleaning when the technology advances to the bio-electronic era. For example, piranha solution would corrode all of the metal contacts, e.g., the Al-Si-Cu alloys that are the most commonly used in semiconductor manufacturing. Hence, we sought a relative mild cleaning method that would restore the electrical signal in the NW devices—one that could be used as a substitute for washing with piranha solution—in the blooming field of coupling biomolecules to semiconductor electronics.

A silicon substrate on which stacked with $\text{SiO}_2/\text{Si}_3\text{N}_4/\text{SiO}_2$ film in a low-pressure quartz furnace was employed to test the efficiency of the various cleaning solutions. The primary SiO_2 film was a buffer layer to prevent the Si_3N_4 film from peeling off. The upper SiO_2 film was then patterned to form a line structure, as indicated in Fig. 4.4(a). The content of cleaning solutions and the post-cleaning immobilization procedure were mentioned in session 4.2.2. Because the immobilization efficiency of DNA on a SiO_2 surface is much higher than that on Si_3N_4 , the immobilization selectivity of DNA on these materials could be distinguished by using the line

structure. Prior to immobilizing the 10 nM FITC-labeled capture DNA, the 1-day ambient exposure samples were subjected to cleaning with various solutions to test their cleaning efficiencies. The intensity of fluorescence signal on the SiO₂ surface was then characterized to evaluate the cleaning efficiency. Quantification of the fluorescence images was achieved by the software of Image-Pro Plus (Media cybernetic®). Fig. 4.4(b) displays fluorescence images of the samples without cleaning (control) and after cleaning with DI, piranha, IPA, and ACE. The intensities of fluorescence signal for control and the samples cleaned using DI, piranha, IPA, and ACE are 4.2±0.2, 7.4±0.3, 45.8±1.5, 21.5±0.9, and 33.5±1.4, respectively. Obviously, the samples cleaned using piranha and ACE displayed clear fluorescence images, suggesting that these two solutions were effective surface cleaning agents. Moreover, the fluorescence appeared only on the SiO₂ patterns, indicated that DNA immobilization was unfavorable on the Si₃N₄ surfaces. In contrast, the weak fluorescence images of the surfaces washed with either DI or IPA indicate that they were not cleaned effectively; i.e., the contaminants remaining on the surface affected the immobilization of DNA. Despite its superior cleaning efficiency, piranha solution is very reactive and will corrode interconnect metals. The mild ACE cleaning solution appears to be a good substitute for the traditional piranha solution when cleaning NWFET biosensors.

We also characterized the immobilization efficiency in terms of the electrical properties of the NWFET biosensors. Fig. 4.5 illustrates the I_D-V_G curves recorded at a constant drain voltage ($V_D = 0.1$ V) for various resulting NWFET sensors. The threshold voltage of the base line (prior to cleaning and immobilization of capture DNA) was -10.80 V. It appears that the surfaces washed with DI and IPA was not cleaned effectively; only a few DNA strands bound to the NW, causing small

rightward shifts of the threshold voltage (0.15 and 0.42 V, respectively). In contrast, surface cleaning was effective when using the ACE mixture (rightward shift of 0.63 V for the curve); this clean surface allowed more DNA strands to self-assemble, consistent with the fluorescence images in Fig. 4.4(b). To clarify the influence of the ACE cleaning process, we also measured the electrical properties of the sample after ACE cleaning but without DNA immobilization. In this case, the I_D - V_G curve was almost identical to that of the sample prior to cleaning, implying that the threshold voltage shift arose mainly as a result of immobilizing the DNA strands on the NW surface.

4.2.6 Using the NWFET to detect a mutated gene

To detect BRAF^{V599E} mutation genes, we cleaned the surface of the NWFET with ACE and then immobilized a 30-mer capture DNA strand, having the sequence 5'-AAATATATTA-TTACTCTTGA-GGTCTCTGTG-3', onto the surface. This capture DNA sequence is fully complementary to that of the target DNA which is partial sequence of the BRAF^{V599E} mutation gene [28]. Hence, the capture DNA on the NW surface formed a molecular probe for the detection of target DNA having the specific gene sequence 5'-CACAGAGACC-TCAAGAGTAA-TAATATATTT-3'.

Fig. 4.6 reveals the ability of the NWFET biosensors to detect cancer-related mutation genes. The threshold voltage for the capture DNA-modified NWFET, measured in PBS buffer solution, was -10.16 V (base line). Various concentrations of the target DNA, containing the BRAF^{V599E} mutation gene, were adsorbed onto the surface of the

NWFET device, providing a further rightward shift of the I_D-V_G curve, indicating the successful hybridization of the complementary mutation gene with the capture DNA. The fluorescence image in inset (I) confirms the successful hybridization of the 10 nM FITC-labeled target DNA to the capture DNA.

For de-hybridization, we washed this dsDNA sample with hot DI (90°C) to separate the target DNA from the probe surface; the curve returned to almost the same level as that of the base line. To ensure de-hybridization, we also used the FITC-labeled DNA to trace the reaction pathway of the molecule of interest on the surface. The fluorescence image of the sample obtained after de-hybridization of the FITC-labeled target DNA [inset (II)] reveals that the target DNA was completely separated from the NW surface after de-hybridization.

Fig. 4.7 reveals the exponential relationship between the voltage shift of the NWFET sensor and the target DNA concentration. The voltage shift for the NWFET sensor under various target DNA concentrations of 10 fM, 1 pM, 100 pM, and 10 nM was 0.22 ± 0.03 , 0.45 ± 0.05 , 0.69 ± 0.04 , and 0.81 ± 0.04 V, respectively. The relationship between the response of a nanobiosensor and the DNA concentration has been reported previously [12] to be

$$S(t) \propto \ln[\rho_0]$$

where $S(t)$ is the sensor response, which is either a voltage or current shift, and $[\rho_0]$ is the DNA concentration. This equation suggests that the response of a nanoscale sensor should exhibit a logarithmic dependence on the DNA concentration, consistent with our finding. The linear fitting for the calibration curve is $y = 0.119 * \log(x) + 1.8817$ from 10 fM to 100 pM with correlation coefficient of 0.988. The detection limit, which is defined as the minimal mutation gene concentration that gives a voltage shift which is 3 times the standard deviation, is estimated to 0.88 fM from the calibration curve. In addition, the relative standard deviation of threshold voltage shift for the target DNA is less than 12%.

Fig. 4.8 reveals the specific detection of target DNA using our NWFET. We investigated the behavior of mismatched target DNA strands (concentration: 10 nM) containing one and five mismatched bases; their DNA sequences were 5'-CACAGAGACC-TCAAGTGTAATAATATATTT-3' and 5'-CACAGAGACC-TCAAGTACGG-TAATATATTT-3', respectively. The latter exhibited the same response as that of the base line, whereas the former exhibited a rightward shift but could still be distinguished from the complementary sample. These results suggest that the single-base-mismatched target DNA hybridized to a small degree, but the five-base-mismatched DNA barely reacted with the capture DNA. A similar result has been reported for three-base-mismatched mutant genes, which

interacted nonspecifically with an NW sensor, but could be quantified and distinguished from their corresponding wild-type genes [6].

4.3 A novel silicon NB FET for hepatocellular carcinoma detection

There is increasing need to develop ultrasensitive and selective biological sensors for disease detection, drug discovery, and biomedical diagnostics [29]. For example, ultrasensitive biological detection systems that allows the early detection of genetic disorders are expected to improve preventative health care. At present, the most widespread techniques for detecting biomolecules are based on enzyme-linked immunosorbent assays (ELISAs) [30] and polymerase chain reactions (PCRs) [31]. The ELISA method determines the level of an antigen in a sample through the magnitude of a fluorescence signal; its drawbacks include the need for a fluorescent label and relatively insensitive detection [32]. The PCR method utilizes enzymatic replication to amplify a deoxyribonucleic acid (DNA) fragment; it also has problems relating to fluorescent labeling and the long periods of time required to amplify traces of DNA [33]. The development of real-time, label-free sensing devices that overcome the drawbacks of ELISA- and PCR-based methods remains a considerable challenge.

Several solid state field effect transistors (FETs), including ion-sensitive FETs (IS FETs) [34] and extended-gate FETs (EG FETs) [35], have been adapted to

function as effective chemical and biomolecular sensors. More recently, such sensors based on quasi one-dimensional (Q1D) semiconductor nanostructures, such as nanotubes [36], nanowires [37], and nanobelts [38], have attracted considerable attention because of their distinct electrical, optical, and magnetic properties. The large surface-to-volume ratios and selective binding of charged biomolecules onto these nanostructures' surfaces can result in significant changes in electronic conductance in the channel of the nanostructure. Hence, the real-time, label-free detection of ultratrace levels of molecules in biological samples has become a real possibility [39]. Cheng et al. [38] were the first to utilize tin oxide nanobelt FETs for the sensing of solution pH, although the switching on/off current ratio, which was related to the method's sensitivity, was limited to only three orders of magnitude because of interference from defects and contamination. To the best of our knowledge, no silicon nanobelt FETs exhibiting excellent field effects have been developed previously for ultrasensitive biomolecule sensing.

Most of the previously available nanostructures have been fabricated using “top-down” or “bottom-up” methods [40]. The latter are usually used to construct nanostructures through vapor-liquid-solid (VLS) growth [41], which requires complicated integration techniques and exquisite control over doping concentration when adapted to the fabrication of high-density sensor arrays in acceptable fabrication

yields. The “top-down” methods for fabricating nanostructures typically employ the high-resolution lithography and reactive-ion-etching (RIE) systems that are used in semiconductor technology [42]. Although these methods are compatible with mass-production, the device fabrication costs are relatively high because advanced lithography tools are expensive [43].

To achieve nano-sized sensor devices, we previously employed a low-cost sidewall spacer technique for the fabrication of a poly-silicon nanowire FET for use as a biosensor [43-45]. The electrical performance of this poly-silicon NWFET was, however, poor in comparison with that expected for the corresponding single-crystalline silicon device; indeed, the higher mobility and better sub-threshold swing of single-crystalline silicon channels relative to those of poly-silicon suggest that more-reliable and -sensitive detection systems are possible. In this section, we describe a novel method—one that does not require expensive lithographic tools to define the nanoscale patterns—for fabricating single-crystalline silicon nanobelt field effect transistors (NB FETs). Specifically, we used the conventional local oxidation of silicon (LOCOS) [46] process to shrink the active silicon film to obtain a nano-sized silicon belt having a thickness of 4 nm and a width of 150 nm. This simple and economical method, which allows the fabrication of uniform and stable silicon

nanobelts, is completely compatible with complementary metal oxide semiconductor (CMOS) technology.

4.3.1 NB FET fabrication

A schematic representation of the fabrication steps is provided in Fig. 4.9. The NB FET sensor was fabricated using a commercially available 6-in. (100) silicon-on-insulator (SOI) wafer, which featured 50 nm-thick intrinsic silicon and 150 nm-thick buried oxide as the device substrate. After standard cleaning ($\text{NH}_4\text{OH}:\text{H}_2\text{O}_2 = 3:1$; then $\text{HCl}:\text{H}_2\text{O}_2 = 3:1$), the stacked films of tetraethyl orthosilicate (TEOS)-oxide and silicon nitride were deposited sequentially as the masking layer for the LOCOS process (Step 1). The underlying layer of TEOS-oxide, a so-called pad oxide, was used to cushion the transition of the stresses between the silicon substrate and the nitride film. In Step 2, an optical lithography system (Canon FPA-3000i5 stepper) and a plasma etching system (TEL TE5000) were used to define the silicon nitride (Si_3N_4)/TEOS-oxide as the active region. In Step 3, after the photo-resistor (PR) was removed, a silicon oxide (SiO_2) was grown thermally to oxidize the exposed silicon, while the patterned silicon nitride prevented the underlying silicon from oxidizing. The active region, including the nanobelt, source, and drain, was therefore defined as a result of the silicon nitride capped on top of the regions. Moreover, the

width of nanobelt was shrunk due to oxidant diffusion laterally during the oxidation process, as revealed in Figs. 4.10 (a) and (b). This phenomenon, the well-known “bird’s beak” effect, can self-reduce the width of a nanobelt to less than the expected width of the exposure system. The dimensions of the nanobelt were strongly dependent on the oxidation time (thickness). Figs. 4.11(a) and (b) present cross-sectional TEM images of the nanobelt after performing 150 and 240 nm–thick oxidation steps, respectively. The dimensions of the nanobelt in Fig. 4.11(b) are much smaller than those in Fig. 4.11(a) because the greater oxidation time of the former led to greater shrinking of the Si nanobelt. The thickness of the silicon oxide must be considered and verified to ensure not only that the underlying silicon had been oxidized completely but also that it maintained the nanobelt thickness. Through the improvement of LOCOS process, the nanowire can also be fabricated by this shrinking method, as shown in Fig. 4.11(c).

Prior to Step 4, wafers were immersed into a phosphoric acid solution at 165°C to remove the residual silicon nitride. In Step 4, optical lithography and ion implantation with a dosage of $5 \times 10^{15} \text{ cm}^{-2}$ from an arsenic ion beam (As^+) were performed on both the source and drain areas (acceleration energy: 20 keV), followed by rapid thermal annealing (RTA) at 1050°C for 30 s in a nitrogen ambient. In Step 5, optical lithography and a lift-off Al-Si-Cu alloy metallization were performed to

define the contact pad. In Step 6, the SiO₂ and Si₃N₄ layers were deposited sequentially through plasma-enhanced CVD (PECVD) to passivate the surface. In Step 7, the detection region of the NB FET was sequentially etched back by plasma etch (for Si₃N₄) and diluted buffer oxide etching solution (BOE for SiO₂, NH₄F : HF : de-ionized water = 42: 7 : 1) for the purpose of biomolecule detection. The PR was then removed by H₂SO₄ and H₂O₂ mixture (H₂SO₄ : H₂O₂ = 3:1). Then, only the backside surface was dipped and etched by BOE solution in a pipette. Finally, a 500-nm-thick Al-Si-Cu pad was deposited by sputter system (Step 8). Prior to biomolecule binding, all the devices were preserved in clean room for at least one week to ensure the thickness saturation of native oxide.

4.3.2 Surface modification of the NB FET

A schematic representation of the surface modification process is given in Fig. 4.12. Prior to surface modification, the NB FET sensor was cleaned for 30 min using acetone/ethanol (1:1). These organic solvents were of analytical grade (Merck, Darmstadt, Germany). After cleaning, the detection region of the NB FET was modified using (3-aminopropyl)triethoxysilane (APTES; 98%; Sigma–Aldrich). Initially, the samples were immersed into a 1.5% APTES aqueous solution for 30 min, and then rinsed with de-ionized (DI) water, followed by drying on a hot plate (120°C

for 30 min). Because of the formation of the native oxide on the silicon nanobelt surface, silanol groups, which are good proton donors (H^+) and acceptors (SiO^-), were present on the detection region of NB FET. APTES was then self-assembled onto the surface for the Si and H^+ reaction. At this stage, amino groups were presented as terminal units on the surface. Next, glutaraldehyde (25%; MP Biomedicals Inc.) was linked to the amino groups to present aldehyde groups on the surface; the glutaraldehyde solution was first diluted with DI water to 2.5% and then the sample was immersed in the linker solution for 30 min at room temperature, followed by rinsed with DI water and drying under ambient N_2 .

4.3.3 AFP antibody and antigen modification

A schematic representation of the AFP antibody and antigen modification steps is illustrated in Fig. 4.13. The antibody and antigen (Blossom Biotechnologies, Taipei, Taiwan) were stored at an $-20^\circ C$ ambient. Prior to modification, the antibody and antigen were thawed naturally at room temperature. The antibody was diluted with 1X phosphate-buffered saline (PBS; 120 mM NaCl, 2.7 mM KCl, 10 mM phosphate buffer; Sigma–Aldrich) to provide a 500 ng/mL solution of antibody. The 1X PBS solution was diluted with DI water and adjusted to pH 7.4. After then sensor had been functionalized with APTES and glutaraldehyde, a portion (100 μL) of the antibody

solution was placed onto the detection region, left for 10 min to ensure effective binding, and then rinsed with PBS to wash away the excess antibody. Next, the sample was immersed into bovine serum albumin (BSA) solution to block any unreacted parts for specific detection. BSA was used here because it is stable, inert toward the tested biomolecules, and cheap.

After attaching the antibody, the cancer marker AFP antigen (Blossom Biotechnologies, Taipei, Taiwan) was applied to bind to the antibody on the NB FET surface. To examine the sensitivity, the AFP antigen was diluted with 0.1X PBS buffer to various concentrations. Prior to selective binding of the AFP antigen to the receptor-modified NB FET device, PBS solution was injected into the microfluidic channel and run through the NB FET detection region to determine the influence of the buffer solution on the sensor. A typical electrical response after PBS had been injected into the detection region of the NB FET sensor is presented in Fig. 4.14. The real-time electrical response of the NB FET sensor was measured for the microfluidic system using an Agilent 4156C instrument.

4.3.4 Preparation and detection of mice serum

The infant and adult mice used to detect AFP were male BALB/c mice, purchased from the Laboratory Animal Center of Taipei Medical University. The infant mouse was 4 weeks old; the adult was 1 year old.

Initially, the antibody was immobilized on the sensor and then the remaining exposed areas were blocked with BSA. Blood was then drawn through cardiac puncture. Prior to using the NB FET sensor to detect the AFP concentration, the mouse serum was extracted in a centrifugal extractor to eliminate hemocyte from the blood. The mouse serum was then injected into the microchannel and run through the detection region of the sensor. The electrical measurements of the NB FET sensors were performed to obtain the device properties.

4.3.5 Modification of HBV DNA probe

The selective immobilization technique was used to bind the terminal 3'-amino group of the oligonucleotide to the aldehyde groups on the sensor's surface. A schematic representation of the DNA modification steps is provided in Fig. 4.15. The 15-mer capture DNA strand having the sequence 5'-NH₂-ACGTCCCGCGCAGGA-3' was purchased from MDBio, Inc. (Taipei, Taiwan). A solution of synthetic 1 μM capture DNA was diluted with PBS buffer to provide a 10 nM solution of capture DNA. A portion (100 μL) of this capture DNA

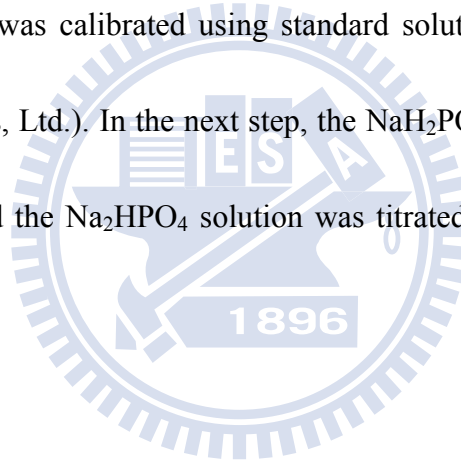
solution was placed onto the detection region of the NB FET and left for 10 min to ensure effective immobilization. The unreacted aldehyde groups were blocked through reactions with ethanolamine (Sigma–Aldrich) and then the surface was washed with PBS buffer and dried under ambient N₂.

After capture DNA immobilization, a strand of synthetic target DNA (MDBio, Inc., Taipei, Taiwan) having the sequence 5'-TCCTGCGCGGGACGT-3', which is the fragment of the HBV *x* gene at position 1403–1417, was applied to hybridize with the capture DNA probe on the NB FET surface. The 15-mer target DNA was diluted to various concentrations with 1X PBS buffer solution (pH 7.4). To ensure successful hybridization, a fluorescence-labeled capture DNA (MDBio, Inc., Taipei, Taiwan) was also prepared. The fluorescent label, fluorescein isothiocyanate (FITC), was specifically positioned at the 5' end of the target DNA. A fluorescence image of the FITC-labeled target DNA hybridized onto the detection region of the sensor is presented in Fig. 4.15.

Prior to injecting the target DNA, PBS solution was injected into the microfluidic channel and run through the NB FET detection region to determine the influence of the buffer solution on the sensor. The real-time electrical response of the NB FET sensor was recorded for the microfluidic system using an Agilent 4156C instrument.

4.3.6 Preparation of the hydrogen ion solution

The hydrogen ion solution was formulated from sodium phosphate monobasic monohydrate ($\text{NaH}_2\text{PO}_4 \cdot \text{H}_2\text{O}$, pH 4.3) and sodium phosphate dibasic (Na_2HPO_4 , pH 9.0), both purchased from J. T. Baker (USA). Each powder was dissolved into DI water to form a 1 mM solution. To measure the pH of the solution, a pH meter (Model 6173pH; Jenco Electronics, Ltd.) having the precision of ± 0.01 was employed. Initially, the pH meter was calibrated using standard solutions (pH 7.00, 4.01, and 10.01; Jenco Electronics, Ltd.). In the next step, the $\text{NaH}_2\text{PO}_4 \cdot \text{H}_2\text{O}$ solution was used as the base solution and the Na_2HPO_4 solution was titrated to adjust the solution to various values of pH.



4.3.7 Nanobelts images

Fig. 4.16(a) displays a cross-sectional transmission electron microscopy (TEM) image of the silicon nanobelt. The width of the nanobelt decreased from 500 nm (for the structure formed through relatively inexpensive optical I-line lithography) to 150 nm and the thickness decreased from 50 nm originally to ca. 5 nm after LOCOS processing [inset of Fig.4.16(a)]. We attribute the improved sensitivity of the silicon NB FET biosensor (see below) to this significant shrinkage of dimensions while

retaining a large detection region at the surface. Prior to characterizing the electrical response of this NB FET sensor in a liquid phase, we used PDMS to fabricate a 50 μm -wide microfluidic channel that we sealed onto the chip using a microfluidic holder (Fig. 4.17); the fluid flowing through the active region was delivered by an automatic syringe pump (Model 780270, Kd Scientific, USA). The complete NB FET sensor incorporated with the microfluidic channel is shown in Fig. 4.18.

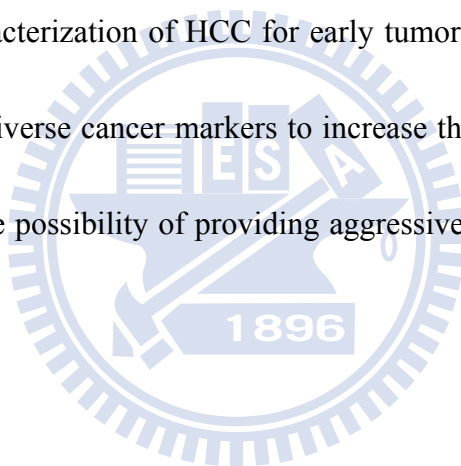
4.3.8 Electrical properties of the NB FET

Fig. 4.19 presents the electrical characteristics of the fabricated NB FET sensor: the dependence of the drain current (I_D) with respect to gate voltage (V_G) at drain voltages (V_D) of 0.5 and 1 V [Fig. 4.19(a)] and plots of I_D versus V_D at various values of V_G [Fig. 4.19(b)]. The electron carriers passing through the NB from the source to the drain were effectively modulated by means of biasing the back-gate voltage. For example, a negative voltage applied to the gate enhanced the channel electron barrier and reduced the obtained current (I_D), whereas a positive voltage applied to the gate reduced the electron barrier and, hence, increased the observed current. Similarly, the attachment of positively or negatively charged molecules resulted in the biosensing devices turning “on” or “off” [47]. The selection of a suitable applied gate voltage would ensure the operation of the proposed NB device under the optimal conditions to

sense biomolecules, due to a resultant change in the surface charge. Fig. 4.19(a) reveals that the ratio of the turn-on and turn-off currents of this sensor was nearly six orders of magnitude, suggesting the improved performance of the fabricated NB FET biosensors. The sub-threshold swing, estimated from the inset to Fig. 4.19(a), was ca. 268 mV/decade, as a result of the thicker dielectric film (150 nm-thick buried oxide). The superior electrical properties of the gate-modulated drain current hints at the successful application of this NB FET for biosensing, because a charged molecule bound to the NB surface would exert an electric field in a manner similar to an applied gate voltage [48]. For example, if the surface receptor coordinates a macromolecule bearing a negative charge, specific binding interactions will result in an increase in negative charge for the NB FET and, hence, a decrease in the value of I_D for the biosensor.

We applied our NB FET as an ultrahigh-sensitivity biosensor for the detection of hepatocellular carcinoma (HCC), which is the most common primary cancer of the liver worldwide. Several diagnosis and treatment methods have been developed for HCC over the years. The five-year survival rate of this disease is less than 5% because of recurrence; the mortality rate of HCC remains high [49]. This vital disease is prevalent in Asia and sub-Saharan Africa. The incidence of HCC in Taiwan is steadily rising, resulting in an increase in the mortality rate from 22.7 per 100,000 population

in 1986 to 28.1 in 2007; it is now the first most common cancer for men and second most common cancer for women [50]. Clinical studies have shown that HCC can be cured through early-stage surgical resection [51]. Because very few neurons spread in the liver, however, patients with HCC in the early state are asymptomatic. Most patients are, therefore, diagnosed in the late-stage or metastasis state, during which time surgical resection is not appropriate [52]. Moreover, erroneous diagnosis, as a result of the false positive identification, is another problem to be overcome [53]. Therefore, reliable characterization of HCC for early tumor identification, as well as multiplex detection of diverse cancer markers to increase the accuracy, would have a significant impact on the possibility of providing aggressive and specific therapies to save human lives.



4.3.9 AFP detection response by the NB FET

To screen HCC, we tested the capability of NB FET to determine alpha-fetoprotein (AFP) as a cancer marker. AFP is a glycoprotein, having the electrophoretic mobility of 1-globulin, that is produced in the fetal yolk sac, liver, and intestine. The expression of AFP antigen in serum is widely used as a tumor marker when evaluating the prognosis and management of patients with HCC. The concentration of AFP is high during fetal liver development, decreasing rapidly within

a few weeks after birth [54]. Once a patient is infected with HCC, the serum AFP concentration becomes markedly elevated [55]. Therefore, the AFP concentration is an important reference index for the physical condition of the liver.

Prior to sensing the AFP biomarker, we functionalized the detection region of the NB FET sensor with the AFP antibody receptor, and then immersed the device into a bovine serum albumin (BSA) solution for 10 min to block the un-reacted parts of the surface to ensure specific detection. Because the sensitivity of a biosensor device correlates with the transconductance ($g_m, \left. \frac{\partial I_D}{\partial V_G} \right|_{V_D=\text{constant}}$), the sensitivity is related to the applied gate voltage [56], with the most sensitive response occurring at the maximum transconductance ($g_{m,\text{max}}$) [57].

Fig. 4.20(a) displays the I_D - V_G curve and transconductance (g_m) of the NB FET ($V_D = 0.5$ V). The value of g_m varies with the back-gate voltage; $g_{m,\text{max}}$ is located at the boundary of the linear and saturation regions in the I_D - V_G curve (in this case, at $V_g = -0.4$ V). The detection of AFP by the sensor biased at $g_{m,\text{max}}$ is presented in Fig. 4.20(b). The sensor exhibited a large current shift after 500 pg/mL AFP had been injected. The I_D - V_G curves of the sensor before and after 500 pg/mL AFP had been injected are presented in Fig. 4.20(c). The injection of AFP to the detection region resulted in a rightward shift of the I_D - V_G curve, indicating that the drain current decreased to a lower level. When the sensor was biased at $g_{m,\text{max}}$ [red arrow in Fig.

8.20(c)], the current decreased to a level close to the noise level of the device, implying that concentrations greater than 500 pg/mL would result in an unapparent and non-linear current shift. Therefore, the detected concentration range when biasing at $g_{m,max}$ extended from 50 fg/mL to ca. 500 pg/mL. Beyond a concentration of 500 pg/mL, the drain current signal dropped significantly to near the noise level. The detection limit of the sensor, defined as the AFP concentration providing a signal intensity three times the standard deviation of the blank, was estimated to be 100 fg/mL.

Although this biosensor was very sensitive when biased at $g_{m,max}$, it was not suitable for AFP detection because the threshold limit value of the AFP concentration in relation to liver injury is ca. 5–20 ng/mL [58]. A patient whose AFP concentration is above the threshold limit value is likely to suffer from HCC. To detect AFP concentrations in this critical range and, thereby, allow specific HCC diagnosis, we tuned the applied gate voltage ($V_g = 0.5$ V) to a higher value so that the sensor would operate with relatively worse sensitivity; in this case, the detection range extended from 3 ng/mL (45 pM) to 600 ng/mL (9 nM) [59]. Fig.e 8.21(a) displays the detection response with respect to various AFP concentrations; note that each concentration was measured using a different device. Therefore, to provide a more definitive comparison, we normalized the currents by dividing by the value of I_D of the AFP pre-injected (i.e.,

blank) sample to observe the minute variations in each run. Because the isoelectric point (pI) of AFP antigen is ca. 4.57 [60], AFP in PBS buffer solution (pH 7.4) exhibits net negative charge. The observed concentration-dependent decreases in I_D are consistent with the amounts of negatively charged AFP antigen bound to the antibody receptor in the n-channel FET devices. The normalized current shift exhibited good linearity with respect to the logarithm of AFP concentrations ranging from 3 to 100 ng/mL [Fig. 4.21(b)]. Beyond a concentration of 100 ng/mL, the currents remained almost fixed, possibly because of saturation of the binding sites in the detection region. The linear fitting for the calibration curve had the form:

$$y = 0.331 \times \log(x) - 0.095$$

with a correlation coefficient of 0.972. The detection limit of the biosensor in this state was estimated to be 2 ng/mL. Note that this detection limit for AFP is not the optimal value because the sensor was not operated under its most sensitive conditions.

4.3.10 AFP detection from mice serum

In addition to the detection of synthetic AFP, we also used our biosensor to study real mice serum samples. The mice serums were bled and extracted using a centrifugal extractor; they were then delivered to the detection region of the sensors.

Fig. 4.22 presents the detection responses of both infant and adult mice. The AFP

concentration is higher in an infant mouse than in an adult mouse—as is also the case for humans—and, therefore, we observed a greater current decrease when analyzing the infant mouse serum. Using the calibration curve in Fig. 4.21(b), we estimated the mouse AFP concentrations, as measured with our NB FET biosensor, to be 26.6 ± 2.1 and 6.8 ± 1.7 ng/mL for the infant and adult mice, respectively. To verify the accuracy of these AFP concentrations obtained from the NB FET biosensor, we used an ELISA kit (Alpha Diagnostic International, San Antonio, USA) to analyze the mice serums through an alternative method (Fig. 4.23). In this case, we obtained the AFP concentrations in the infant and adult mice serums, from the calibration curve of the standard solution, of ca. 25.8 and 6.3 ng/mL, respectively [61]. Because the concentration levels of serum AFP obtained using the NB FET and ELISA methods are very close, our proposed real-time and label-free NB FET appears to be a reliable biosensor.

4.3.11 HBV *x* gene detection by the NB FET

Although AFP is an important marker for detecting HCC, monitoring the AFP concentration alone is insufficient because ca. 5–10% of HCC cases exhibit normal AFP levels [62]. Therefore, to increase the accuracy of the early detection of HCC, we employed a specific DNA fragment of hepatitis B virus (HBV) as an additional

biomarker. HBV infection leads to fulminant or chronic hepatitis, which has great potential for transformation into HCC. Hence, the incidence of HCC is highly dependent on the prevalence of hepatitis B [63]. Schweinitz et al. proposed that patients possessing low levels of AFP, but suffering from HBV, should be categorized as having a high-risk of developing HCC [64]. The *x* gene, which is part of a sequencing fragment of the HBV genomic, plays a critical role in HBV-associated hepatocarcinogenesis [65]. The *x* protein, which derives from the *x* gene, complexes with other proteins and inhibits the specific DNA binding, transactivating, and apoptotic capacity, thereby inducing the cell to transform into an HCC [66].

To detect HBV using the NB FET sensor, we immobilized a 15-mer capture DNA strand having the sequence 5'-NH₂-ACGTCCCGCGCAGGA-3', which is fully complementary to the target DNA, to the sensor surface as the receptor. The synthetic target DNA having a 5'-TCCTGCGCGGGACGT-3' in sequence is a fragment of the *x* gene [67]; it selectively hybridized to the capture DNA probe. Fig. 4.24(a) displays the electrical response for the detection of the *x* gene DNA at concentrations ranging from 1 fM (4.9 fg/mL) to 1 pM (4.9 pg/mL) [68]. Because DNA bears a negative charge, the specific binding interaction enhanced the electron barrier and, hence, led to a decrease in the value of I_D for the NB FET device. The concentration-dependent current shift exhibited good linearity, providing a calibration curve featuring a

detection limit of ca. 2.4 fM [Fig. 4.24(b)].

We also used our biosensor to detect mismatched target DNA to verify its specific binding. The tested mismatched target DNA strands were the one-, five-, and 15-base-mismatched DNA sequence 5'-TCCTGCGAGGGACGT-3', 5'-TCCTGACACTGACGT-3', and 5'-GAACCACACTAGATG-3', respectively. Fig. 4.25 reveals the detection responses of 100 fM of the mismatched target DNA strands binding to the NB sensor. The current shifts in the presence of the five- and 15-base-mismatched target DNA sequences were almost indistinguishable, whereas the one-base-mismatched sample and the complementary sample provided significant decreases in current, implying that the one-base-mismatched target DNA bound to the capture DNA probe through a nonspecific effect. Nevertheless, we could distinguish a difference in current for the analyses of the one-base-mismatched and complementary DNA strands, suggesting that our NB FET biosensor could effectively determine the signal change for HBV after only one base mismatch. A similar result has been reported for three-base-mismatched mutant genes interacting nonspecifically on a nanowire sensor, although they could be quantified and distinguished from their wild-type genes [69].

4.3.12 Solution pH analysis by the NB FET

In addition to HVB DNA, the serum pH is another reference index for the early screening of HCC. The variation in serum pH is attributed to the active metabolism of the transformed cancer cells, resulting in different amounts of carbon dioxide (CO₂) diffusing into the blood plasma. The excess CO₂ is converted to bicarbonate (HCO₃⁻) by the enzyme carbonic anhydrase. Because HCO₃⁻ is the primary buffer of blood pH, the presence of a higher HCO₃⁻ concentration induces more acidic blood—i.e., the blood pH decreases [70]. Furthermore, the mutant cells release acidic poison proteins, which also decrease the blood pH [71]. In general, the pH of normal blood is ca. 7.4; therefore, patients who have a blood pH of less than 7.4 should be vigilant that they may suffer from carcinoma [72].

To detect the effect of the pH on the NB FET sensor, we used sodium phosphate monobasic monohydrate (NaH₂PO₄·H₂O) solution as a base to titrate a sodium phosphate dibasic (Na₂HPO₄) solution from pH 6.40 to 7.39. The sensor had been modified with (3-aminopropyl)triethoxysilane (APTES) on the detection region so that it would present terminal NH₂ and SiOH groups, which are sensitive to changes in pH. Thus, the current of the sensor was related to the solution pH because of the different dissociation constants (pK_a) of the NH₂ and SiOH groups [73]. As a result, the current decreased stepwise upon increasing the pH [Fig. 4.2(a)]. Fig. 4.26(b) reveals that the current had a linear dependency on the pH over the range from pH

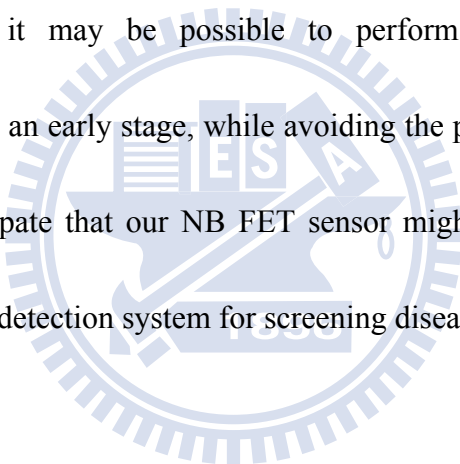
6.40 to 7.39. This result suggests that our NB FET might also act as a pH sensor for serum in the future.

4.4 Summary

In section 4.2, using a cleaning solution prepared from a mixture of acetone and ethanol allowed us to develop an NWFET device that behaved as a biomolecular sensor for an oncogene. We used the state-of-the-art semiconductor line to fabricate label-free NWFET devices having line widths of 60 nm. Connecting the NWs to source and drain electrodes fabricated on the SOI wafer provided functioning ohmic contacts without the problem of contact resistance. The NWFET exhibited n-channel depletion characteristics that allowed detection of the hybridization and de-hybridization of a BRAF^{V599E} mutation gene from a cancer cell, as well as the ability to distinguish between complementary and mismatched target DNA. The detection limit of the NWFET biosensor for the sensing of the mutation gene was in the sub-femtomolar regime. Because this label-free NWFET sensor displayed the ability to detect the oncogene, such devices are potentially useful tools for biological research and genetic screening.

In section 4.3, we used the LOCOS isolation process and CMOS-compatible technology to fabricate novel silicon NB FETs. The shrunken nanobelts, which had

high surface-to-volume ratios, were used to detect HCC. We found that our NB FET biosensor could detect AFP, a biomarker for HCC, at concentrations ranging from 3 to 100 ng/mL, the most critical range for screening HCC. The detection limit for a 15-mer fragment of DNA from HBV, a virus that commonly induces HCC, when using our NB FET sensor reached as low as 3.2 fM. The solution pH could also be distinguished within the range from pH 7.39 to 6.40, a critical blood pH range differentiating healthy individuals from cancer patients. With multiplex detection of AFP, HBV, and pH, it may be possible to perform the reliable, real-time determination of HCC at an early stage, while avoiding the problems of false positive identification. We anticipate that our NB FET sensor might operate as a real-time, label-free, ultrasensitive detection system for screening diseases in the future.



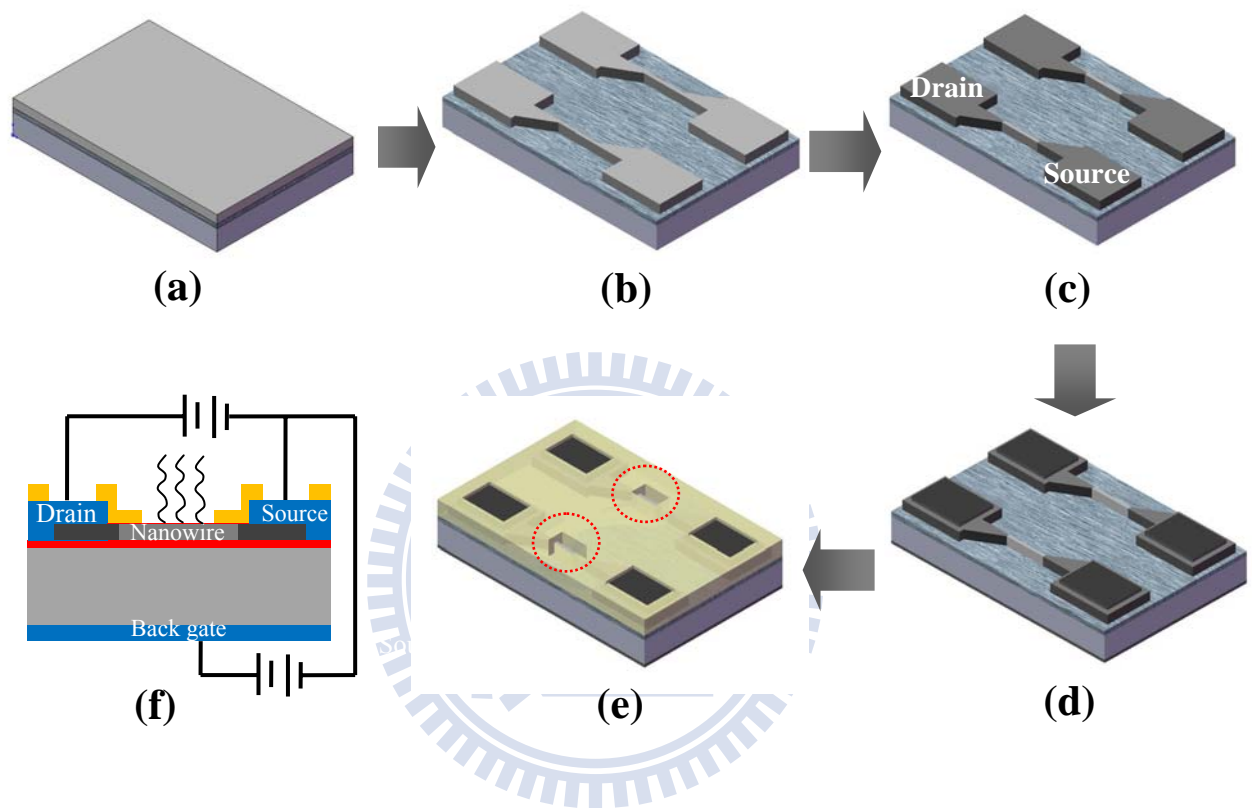


Fig. 4.1 Schematic representation for the fabrication of the NWFET sensors. (a) A 6-in. SOI wafer (50 nm intrinsic Si; 150 nm buried oxide) was employed as the device substrate. (b) NWs were patterned using an e-beam direct writing and dry etching system. (c) Source/drain implantation and annealing. (d) Contact pad (500 nm Al-Si-Cu film) was deposited at the source/drain region. (e) Passivation layer formed, followed by etching back the detection region for DNA immobilization (red circle). (f) Cross-sectional representation of the completed NWFET sensor and its electrical connection for the detection of DNA strands.

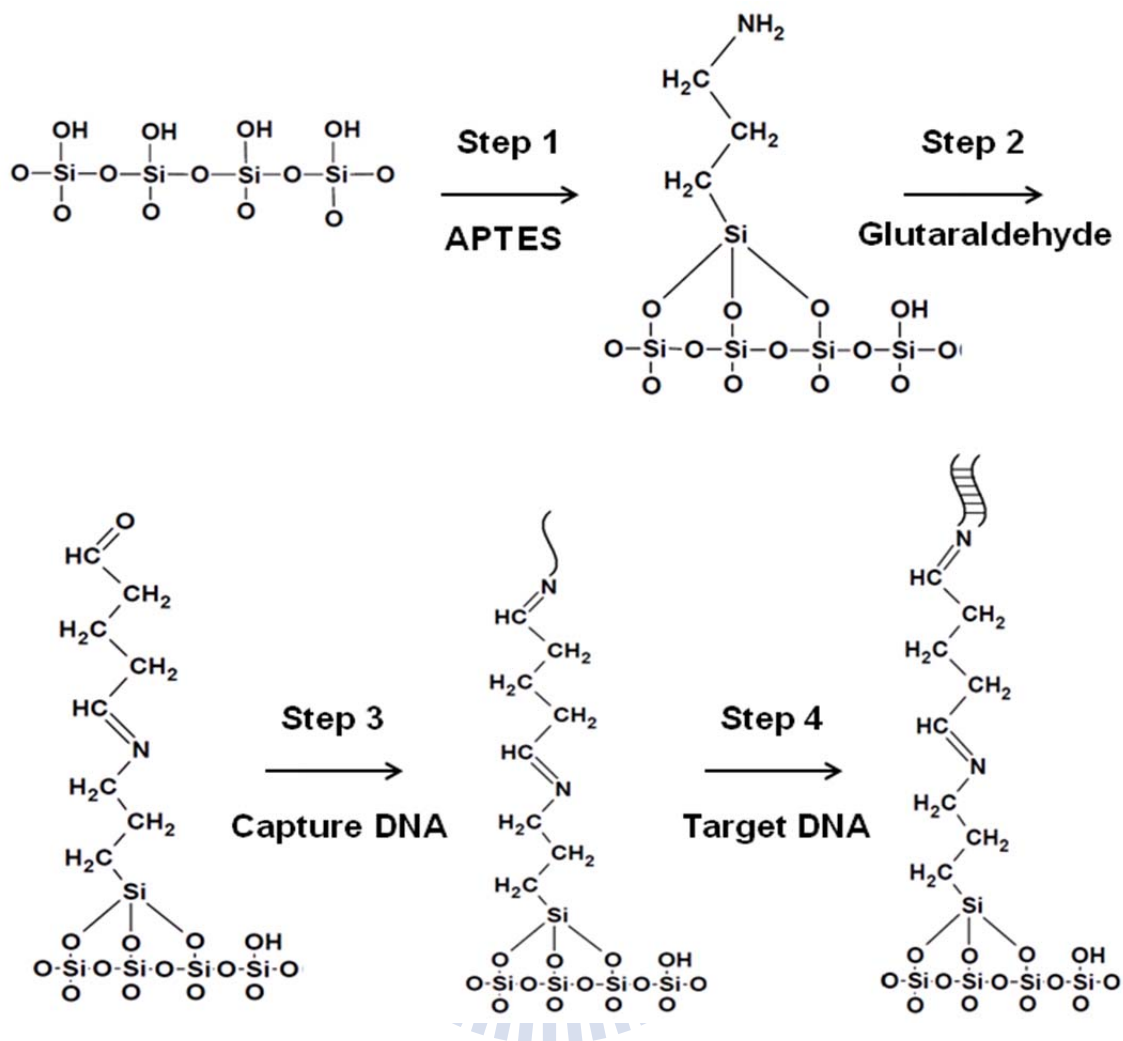


Fig. 4.2 Self-assembly processes for the immobilization of capture DNA and hybridization of target DNA. (1) The Si NW presenting a native oxide on its surface was coated with APTES. (2) Glutaraldehyde was linked to the amino groups. (3) Terminal 3'-amino groups of the capture DNA strands were reacted with the aldehyde groups. (4) Complementary target DNA was hybridized to the capture DNA on the Si NW surface.

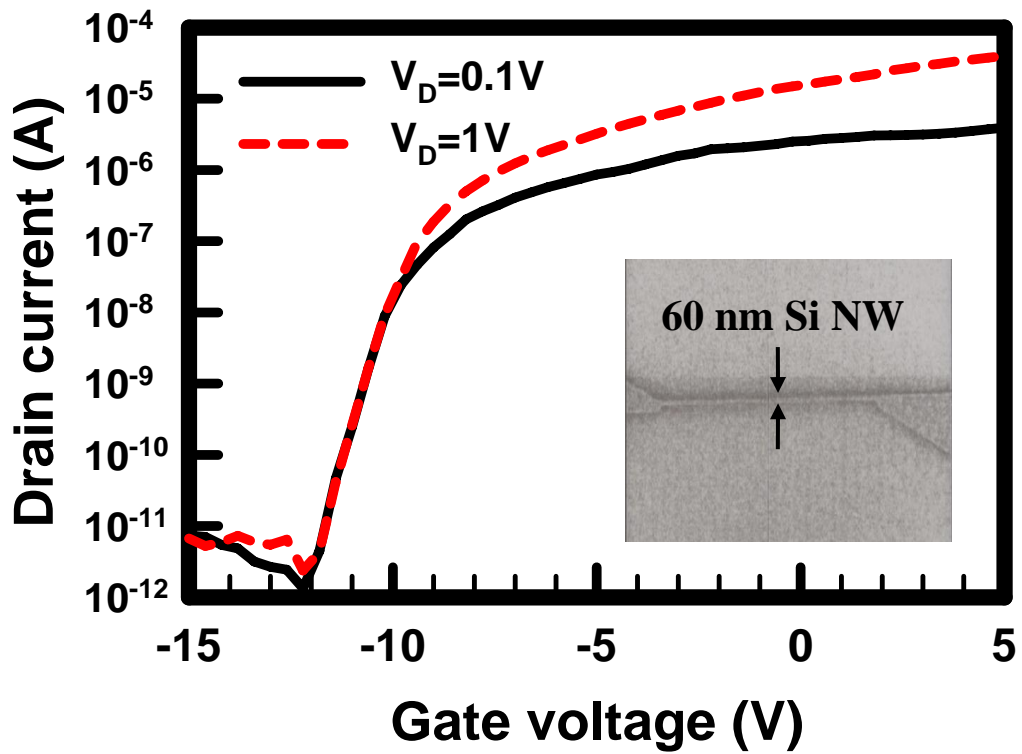


Fig. 4.3 Plots of drain current versus gate voltage for the NWFET sensor, measured at values of V_D of 0.1 (black line) and 1 V (red dotted line). Inset: Scanning electron microscopy image of the 60 nm-wide Si NW.

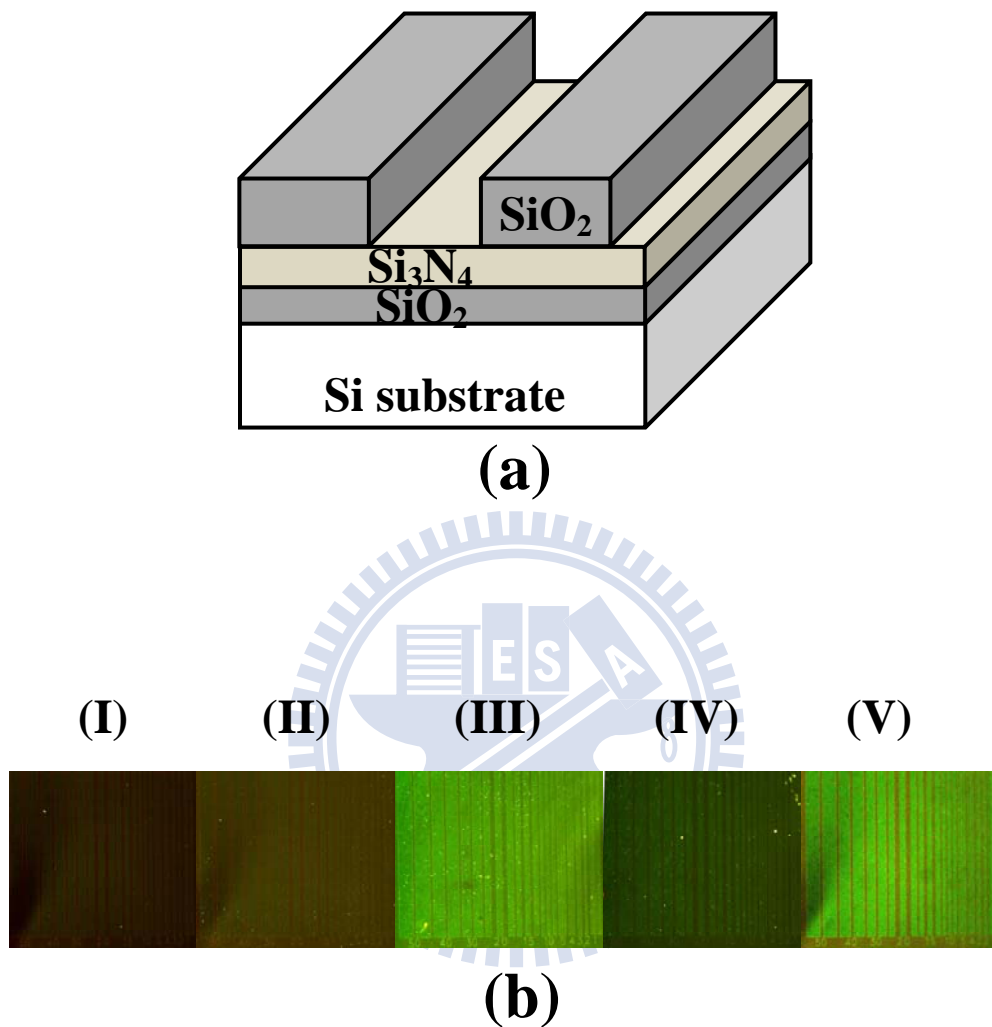


Fig. 4.4 (a) Schematic representation of the SiO₂ line structure used to test the immobilization efficiency. The underlying Si₃N₄ film was used to define the selectivity, because of the higher DNA immobilization efficiency of SiO₂ relative to that of the Si₃N₄ surface. (b) Fluorescence images of the (I) uncleaned (control) sample and (II–V) the samples cleaned with (II) DI, (III) piranha, (IV) IPA, and (V) ACE..

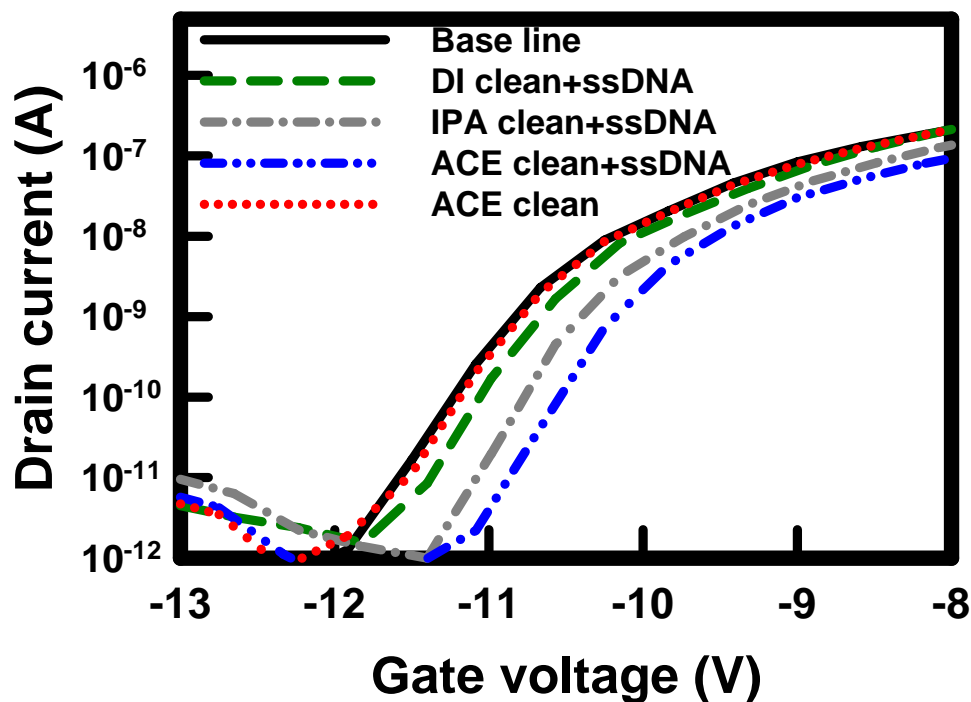


Fig. 4.5 Electrical responses of the NWFET sensor with capture DNA immobilized after using various cleaning methods. The I_D-V_G curves were recorded at a constant drain voltage ($V_D = 0.1$ V). The base line curve was recorded for the sample prior to cleaning but after treatment with PBS (black line). Curves were recorded for the DNA-immobilized NWFET sensors after washing with DI (green dotted line), IPA (gray dotted line), and ACE (blue dotted line). The curve recorded for the sample after ACE cleaning but without DNA immobilization (red dotted line) was recorded to confirm the influence of the cleaning process.

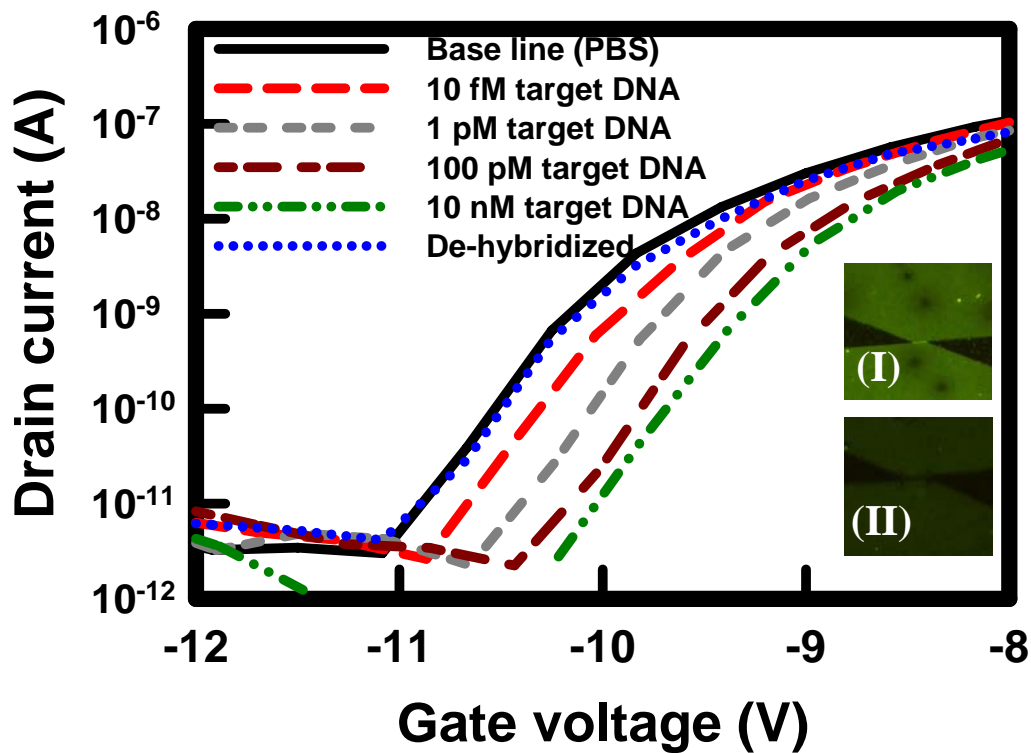


Fig. 4.6 Concentration-dependent electrical response of the capture DNA-modified NWFET sensor when detecting target DNA. The I_D - V_G curve of the base line was obtained in PBS buffer (black line); PBS buffer solutions containing target DNA at various concentrations (10 fM, 1 pM, 100 pM, 10 nM) were injected, respectively, and the I_D - V_G curves recorded. The de-hybridized samples were obtained after treatment of the dsDNA with hot DI water (90°C); the I_D - V_G curves were then measured (red dotted line). Inset (I): Fluorescence image of 10 nM FITC-labeled target DNA bound to the capture DNA. Inset (II): Fluorescence image of the FITC-labeled target DNA after de-hybridization.

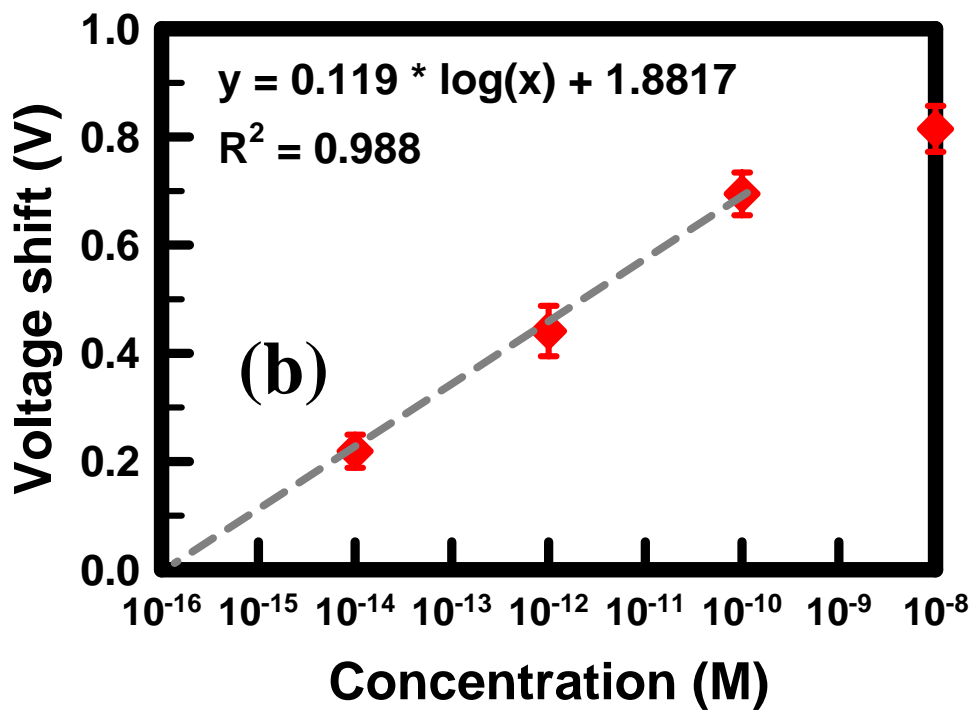


Fig. 4.7 Voltage shift (from $n=4$) of the NWFET sensor plotted with respect to the target DNA concentration. The voltage shift was extracted from Fig. 5(a) at a constant drain current ($I_D = 1$ nA).

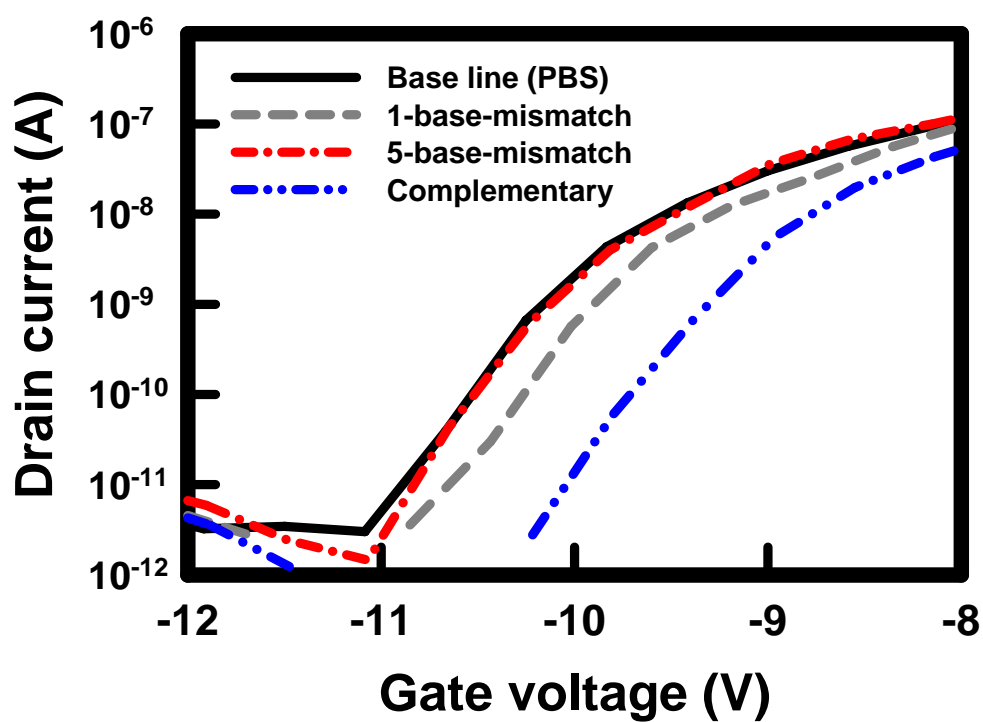
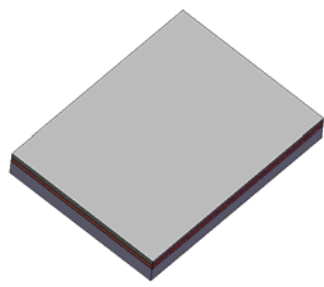
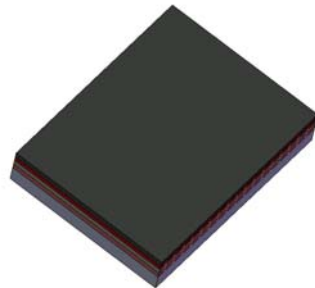


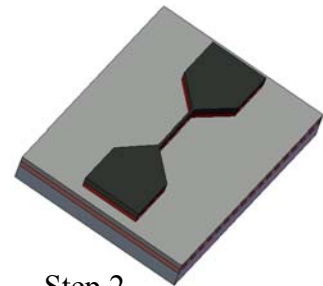
Fig. 4.8 Electrical response of the capture DNA-modified NWFET sensor when detecting mismatched target DNA. The I_D - V_G curve of the base line was recorded in PBS buffer (black line); PBS buffer solution containing one- or five-base-mismatched target DNA strands (10 nM) was injected and the I_D - V_G curves were recorded.



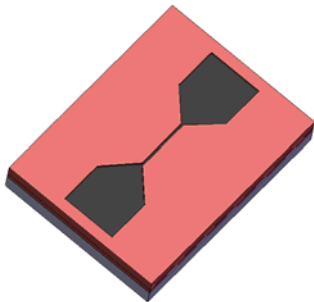
SOI wafer



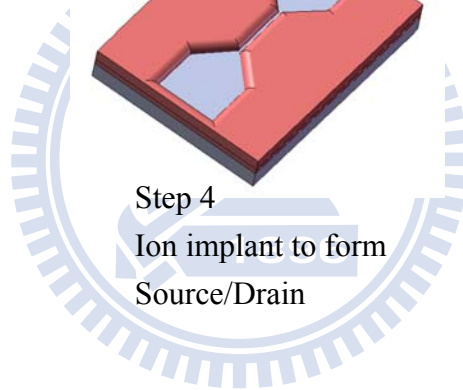
Step 1
TEOS-oxide/Si₃N₄ deposition



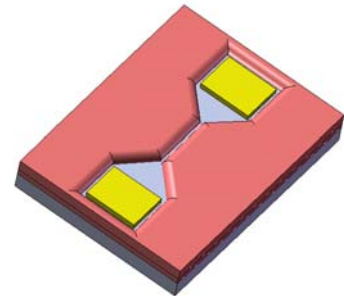
Step 2
Active region definition



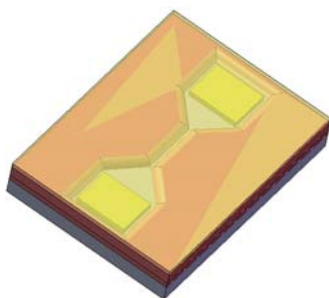
Step 3
Thermal oxidation



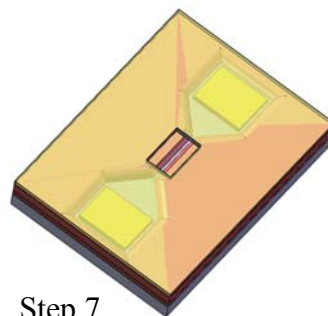
Step 4
Ion implant to form
Source/Drain



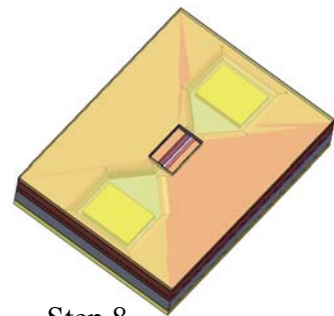
Step 5
Metal pad at Source/Drain



Step 6
SiO₂/SiN passivation



Step 7
Detection region opening



Step 8
Back Gate metal deposition

Figure 4.9 Schematic representation of the NB FET fabrication process.

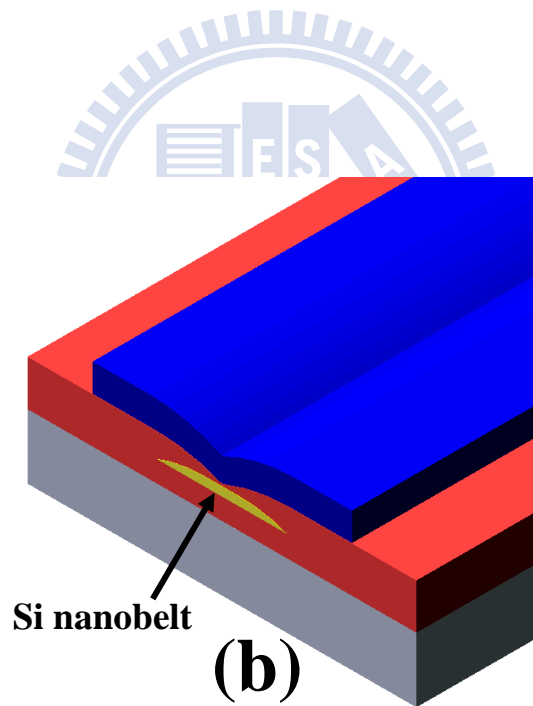
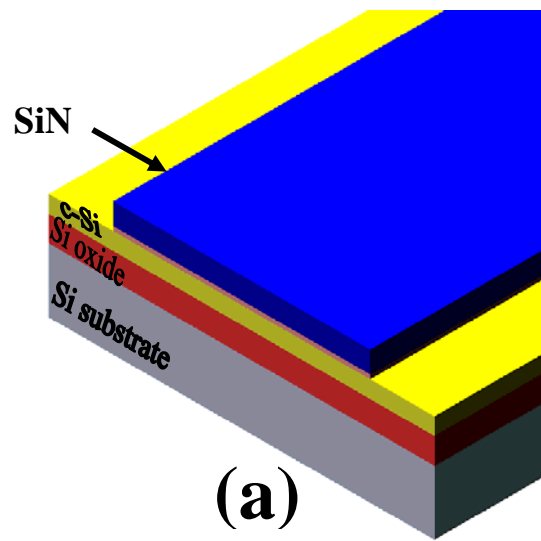


Fig. 4.10 Fabrication of the silicon nanobelt. (a, b) Schematic representations of the structures (a) before and (b) after performing the LOCOS process.

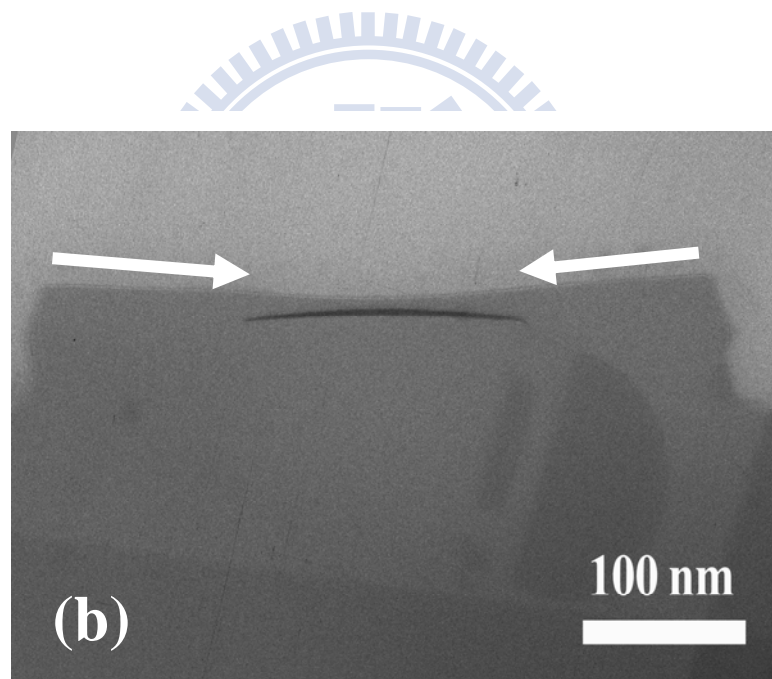
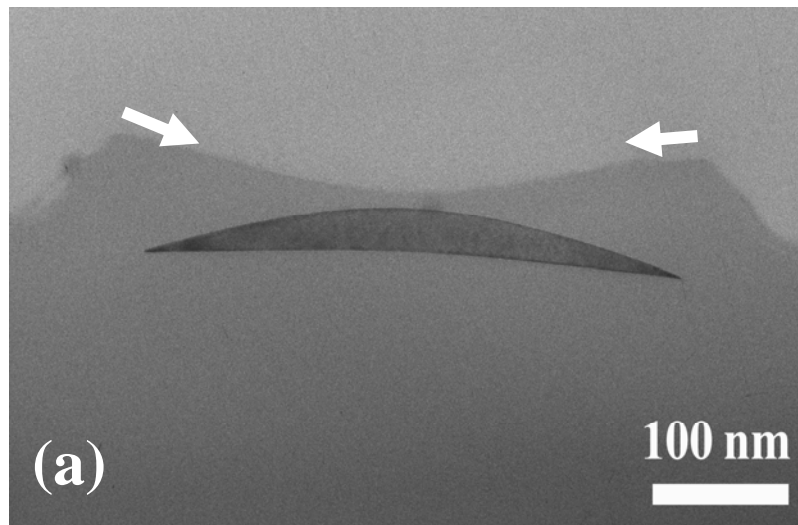


Fig. 4.11 Cross-sectional TEM images of the nanobelt after performing (a) 150 and (b) 240 nm–thick oxidation steps, respectively.

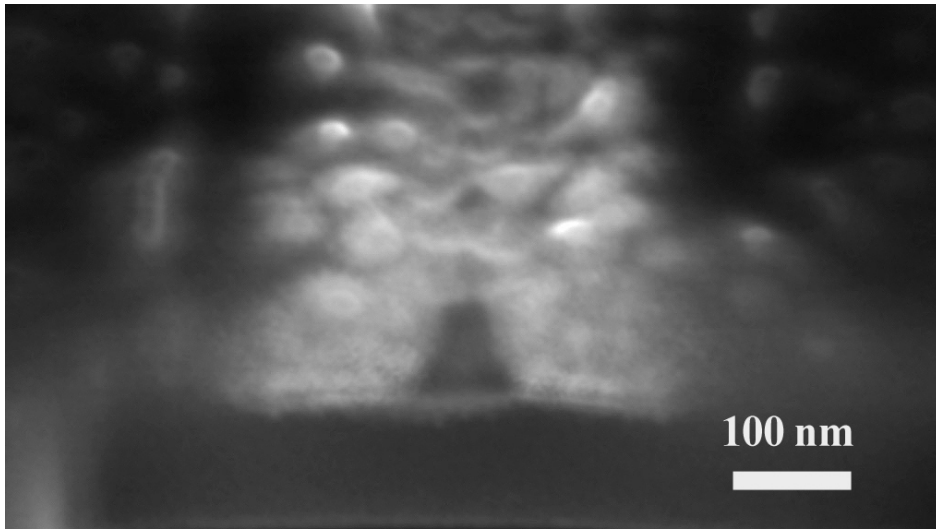


Fig. 4.11(c) Cross-sectional SEM image of the nanowire after improved LOCOS process.

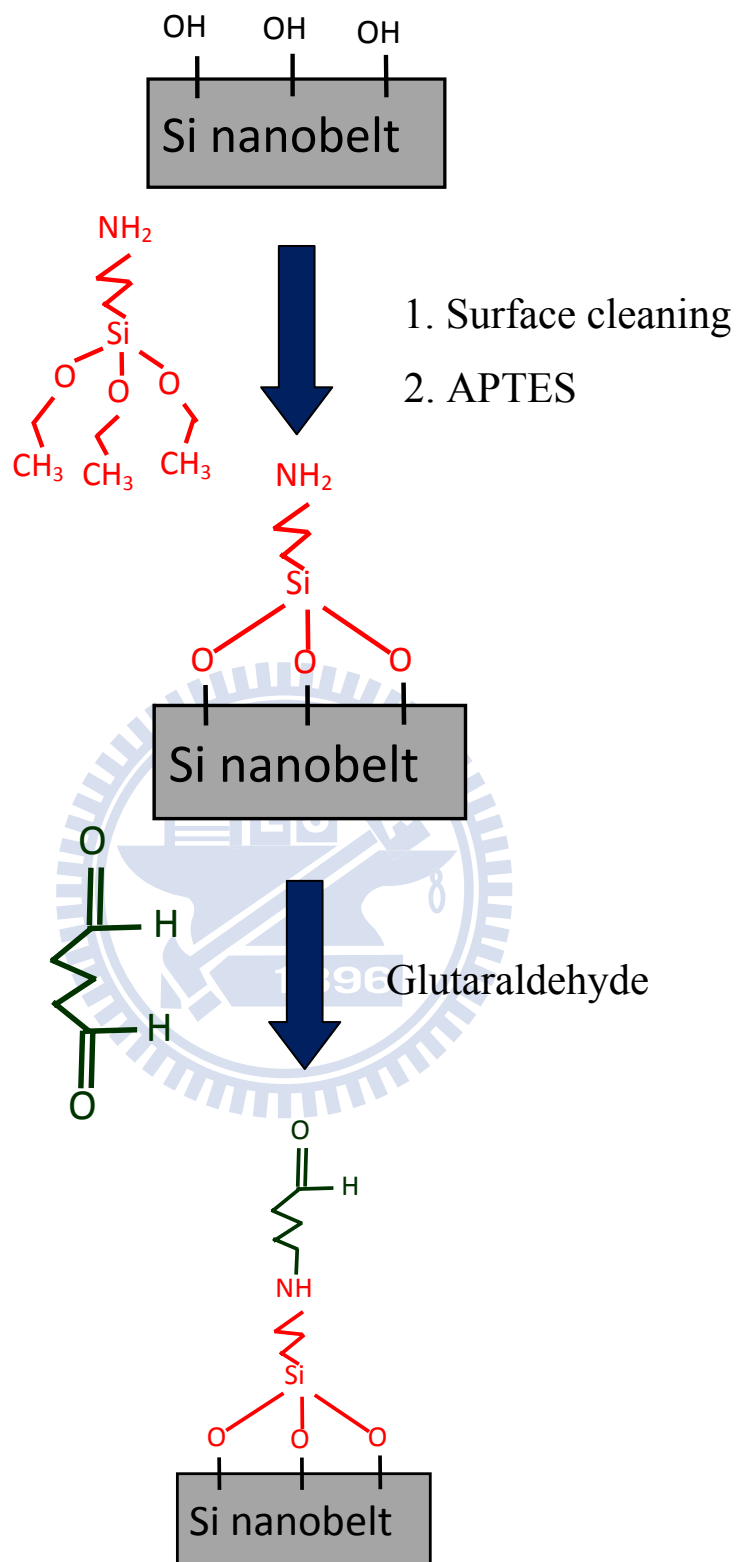


Fig. 4.12 Schematic representation of the NB surface modification process.

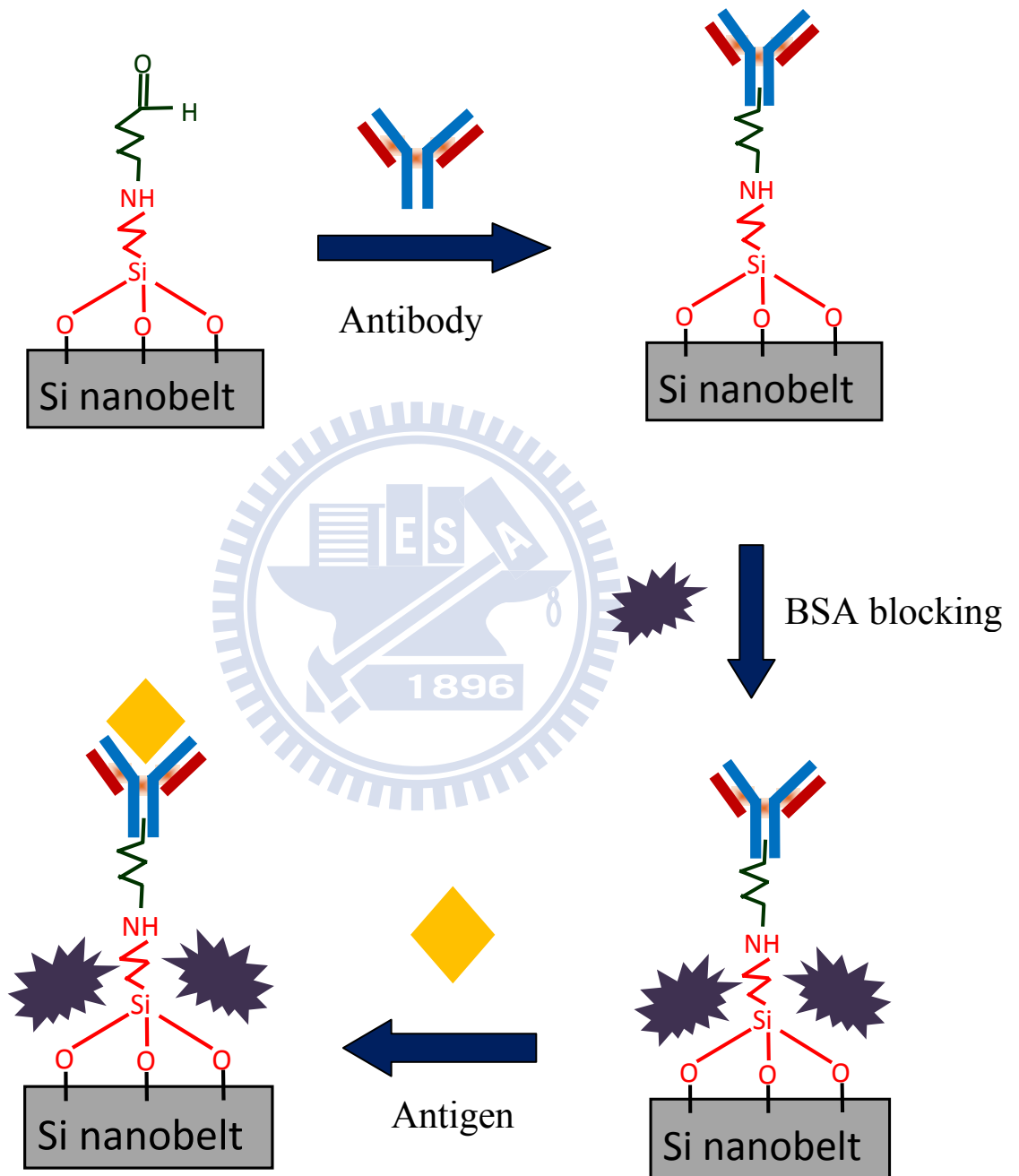


Fig. 4.13 Schematic representation of AFP antibody and antigen modification process.

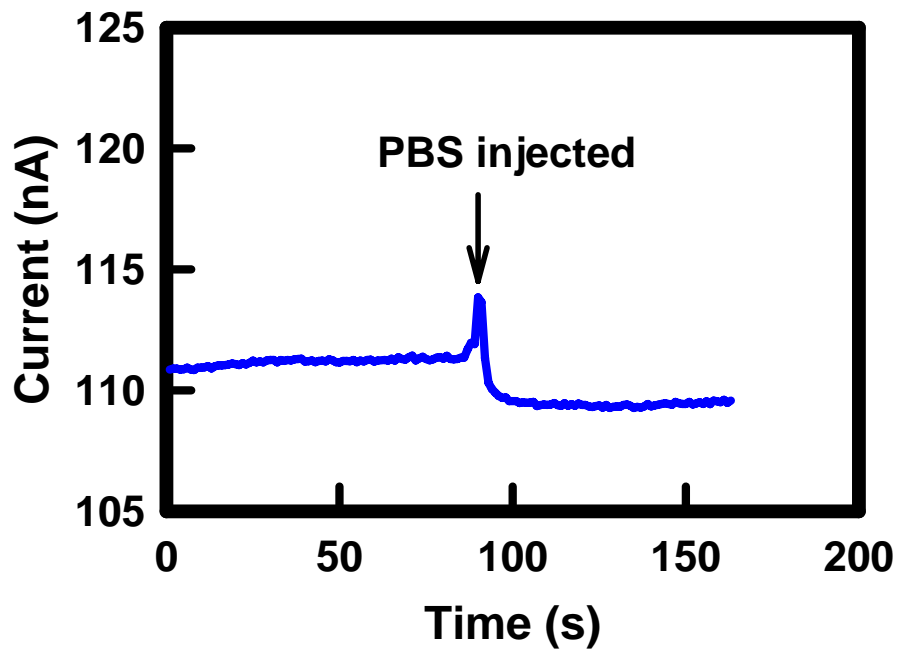


Fig. 4.14 Electrical response of PBS injected into the detection region of the NB FET sensor.

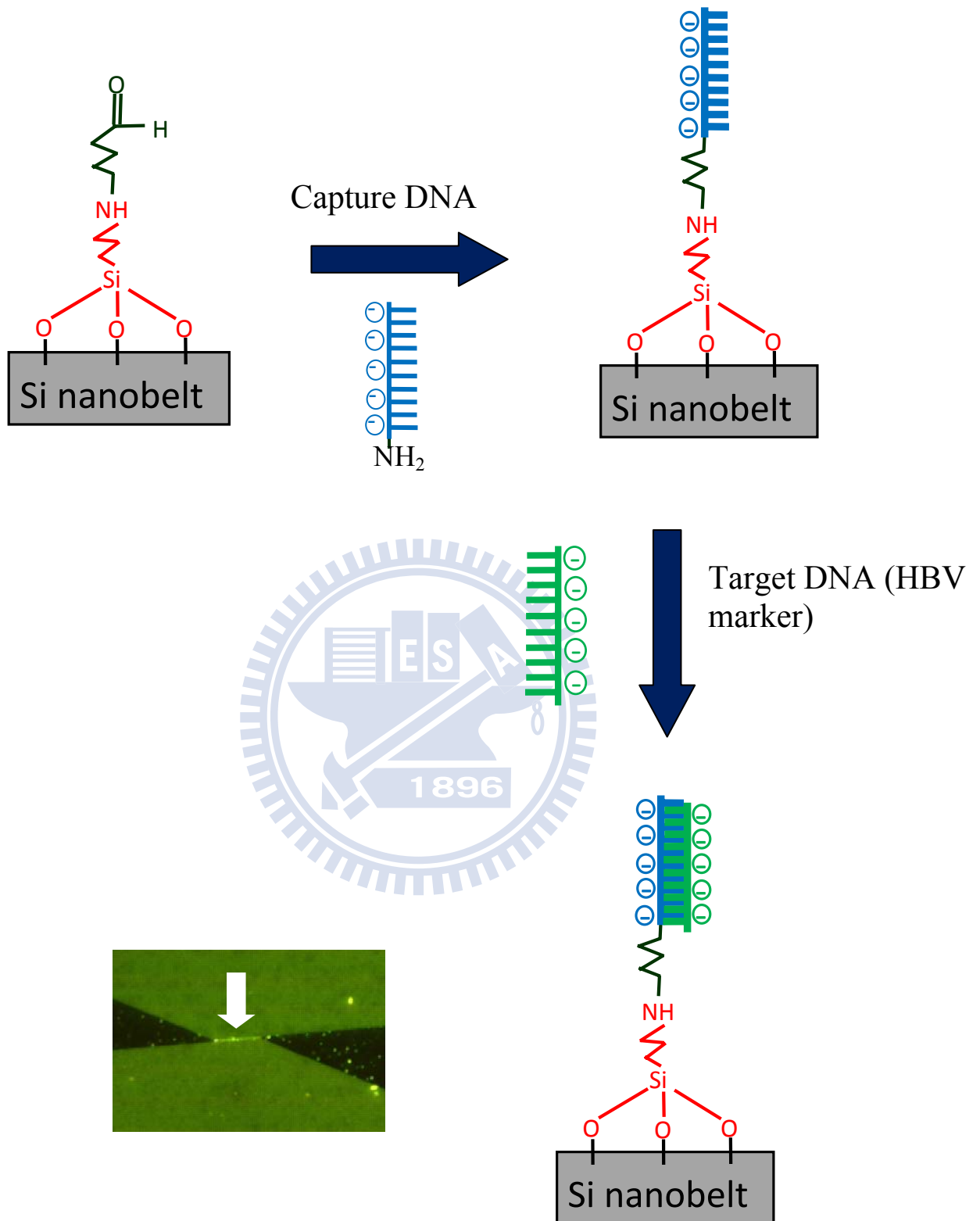


Fig. 4.15 Schematic representation of the DNA modification process.

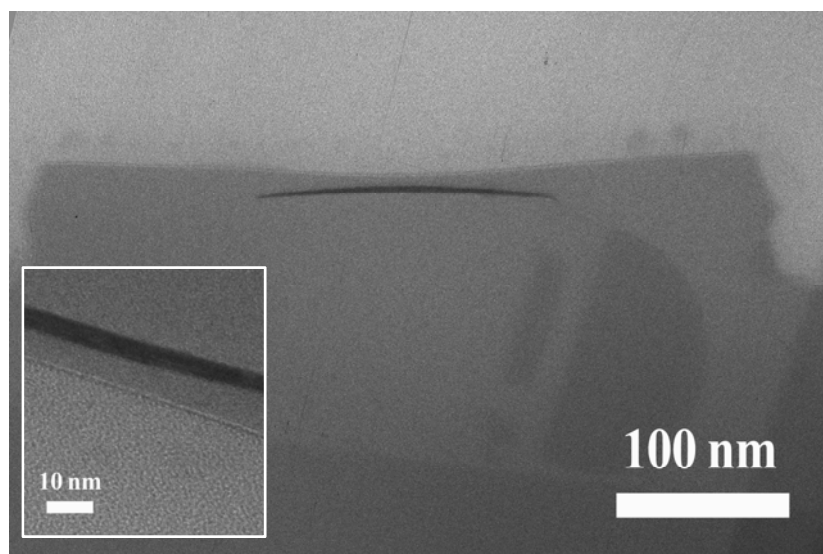


Fig. 4.16 Cross-sectional TEM image of the nanobelt. Inset: enlarged TEM image of the nanobelt to show its thickness.

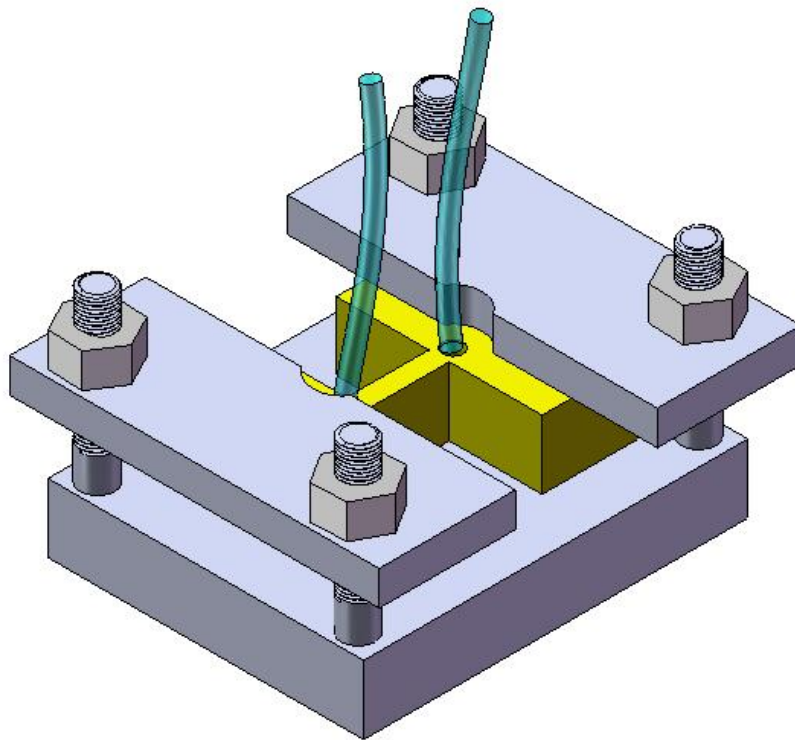
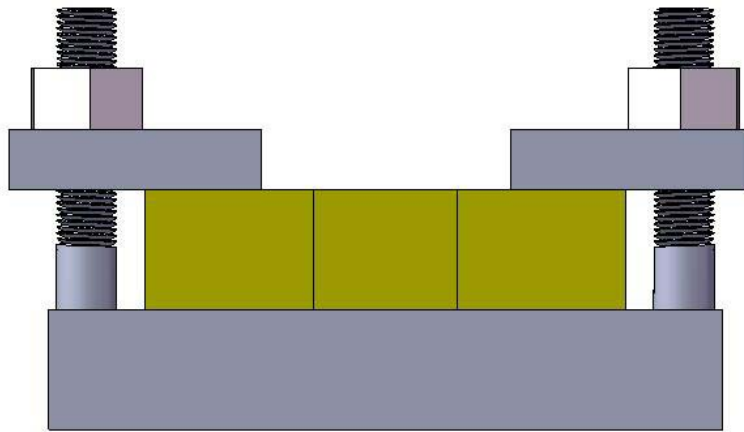


Fig. 4.17 Schematic representation of the microfluidic holder.

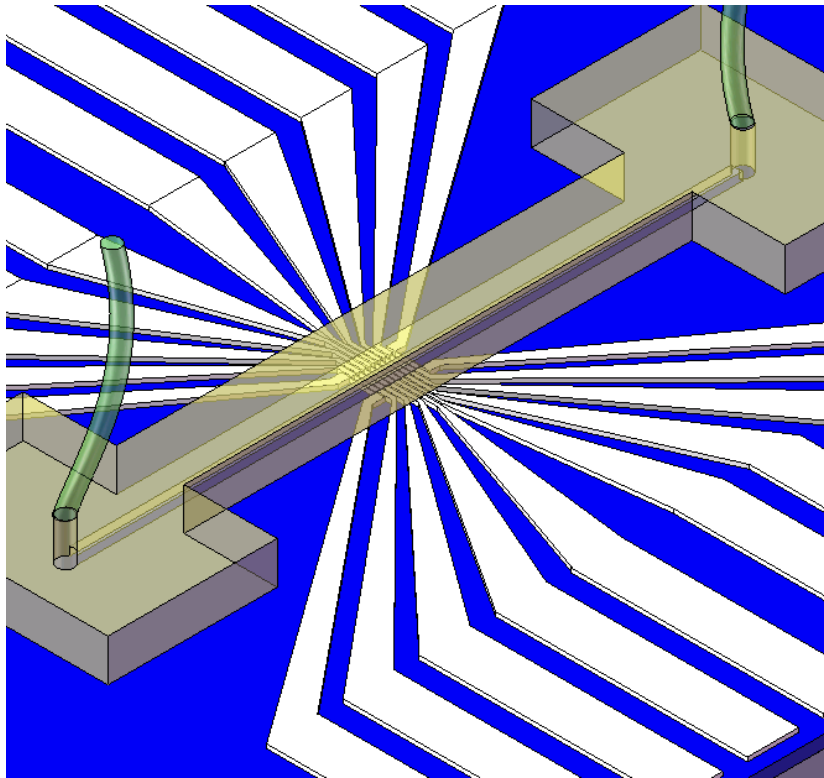


Fig. 4.18 Schematic representation of completed NB FET sensor with microfluidic channel.

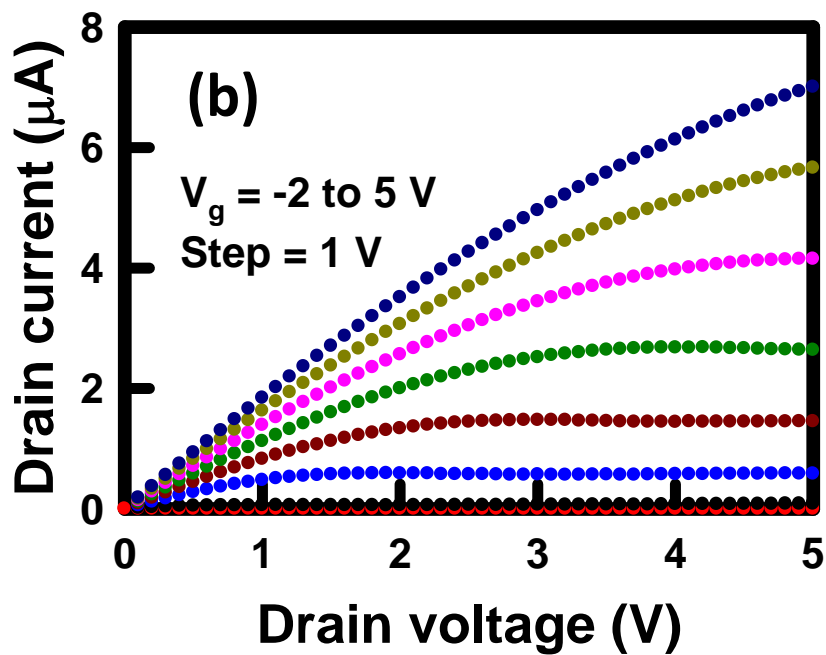
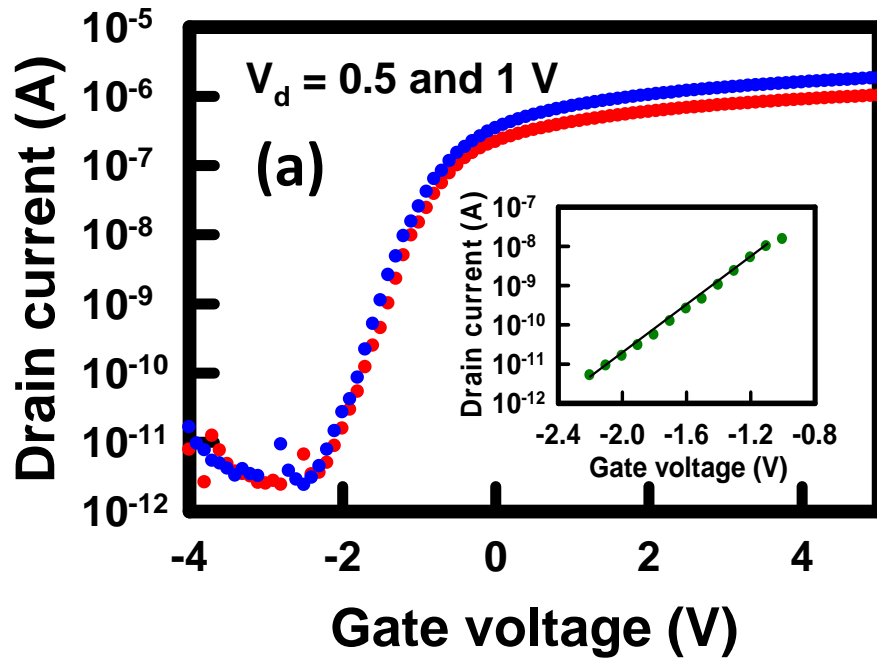


Fig. 4.19 Electrical performance of the NB FET. (a) I_D - V_G dependence for $V_D = 0.5$ (red) and 1 V (blue). Inset: Subthreshold swing in the subthreshold regime. (b) I_D - V_D for varying V_G (-2 to +5 V; $\Delta V = 1$ V).

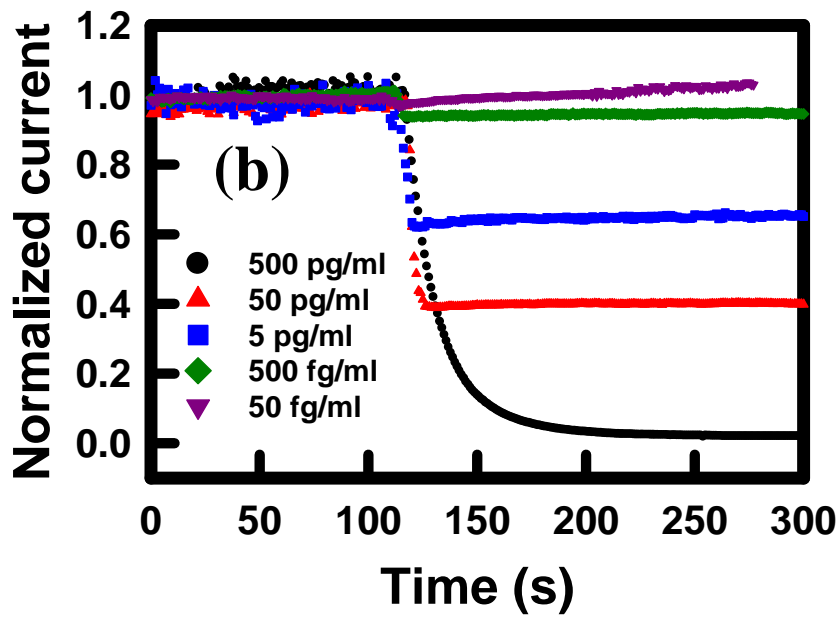
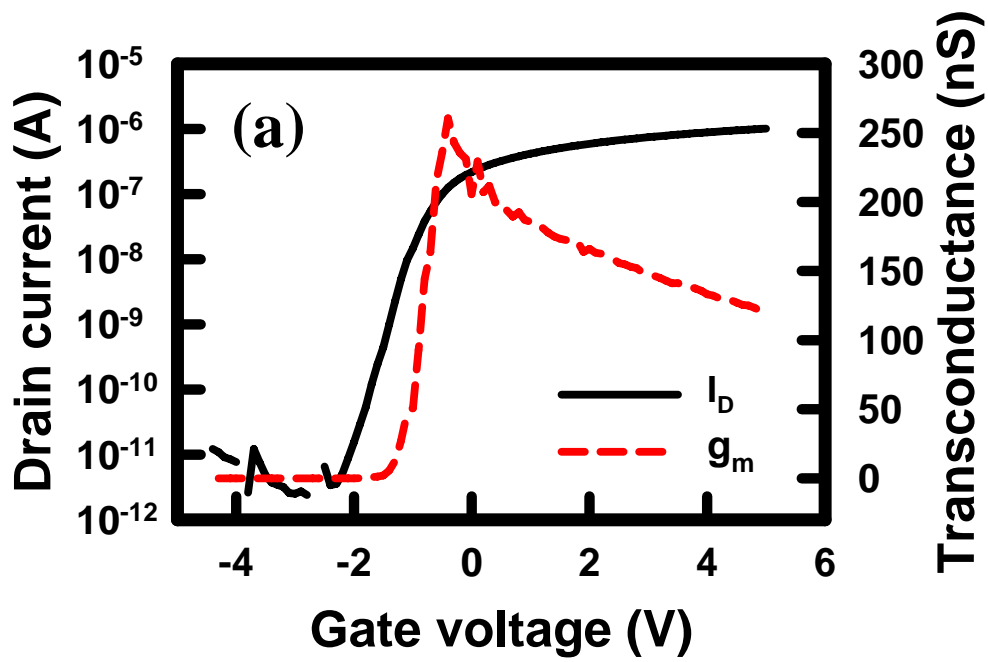


Fig. 4.20 Electrical properties of the NB FET sensors. (a) I_D - V_G curve and transconductance of the NB FET sensor. (b) Detection responses of the NB FET, biased at $g_{m,max}$, toward various AFP concentrations.

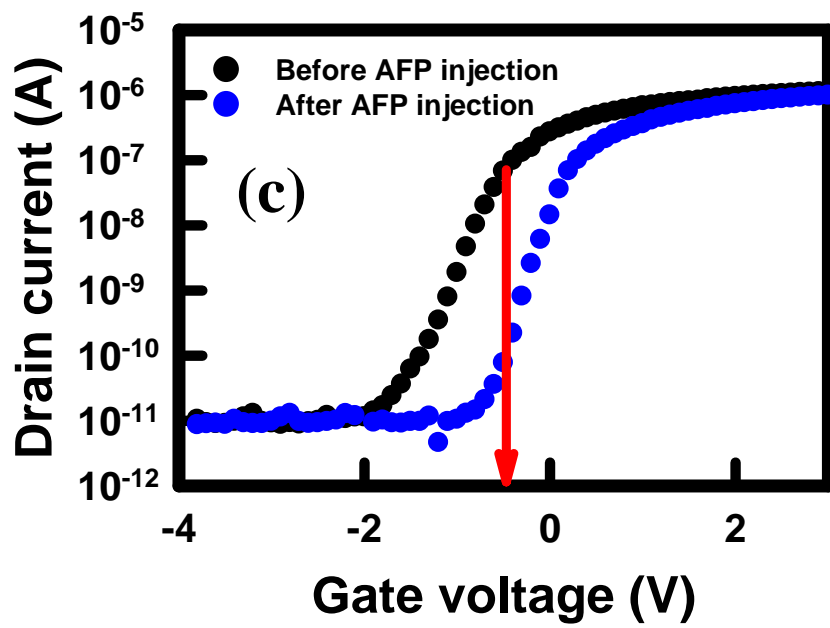


Fig. 4.20 (c) I_D - V_G curves of the NB FET before and after injection of 500 pg/mL AFP.

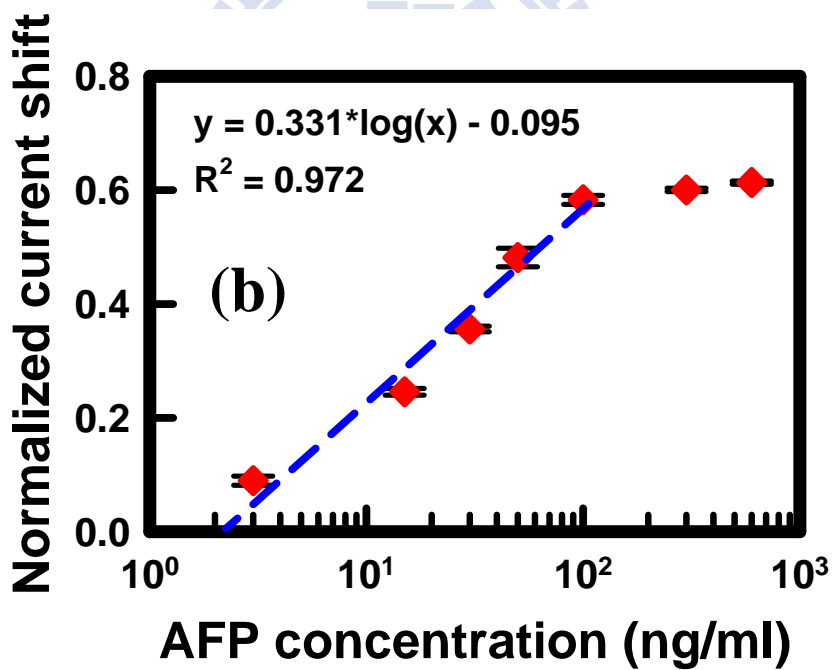
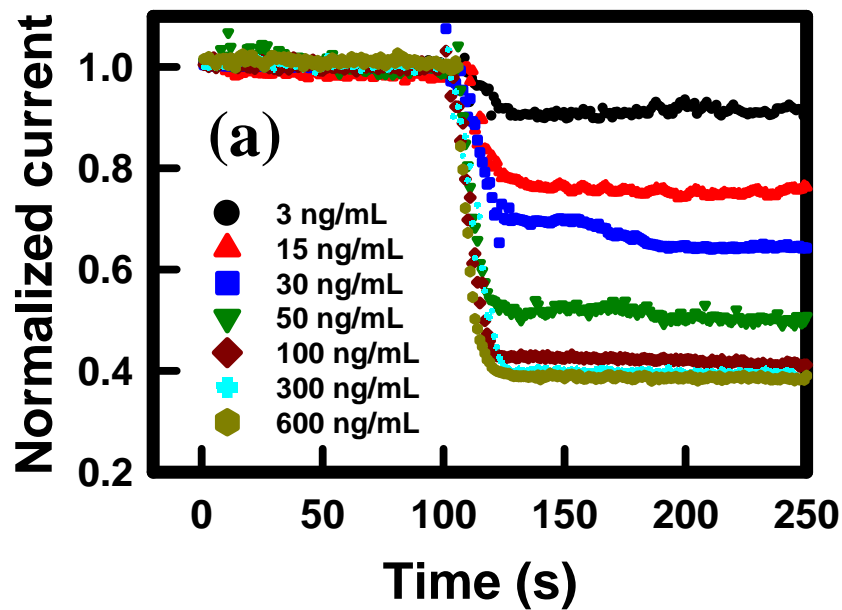


Fig. 4.21 (a) Detection response toward AFP concentrations ranging from 3 to 600 ng/mL. (b) Normalized current shift plotted as a function of AFP concentration.

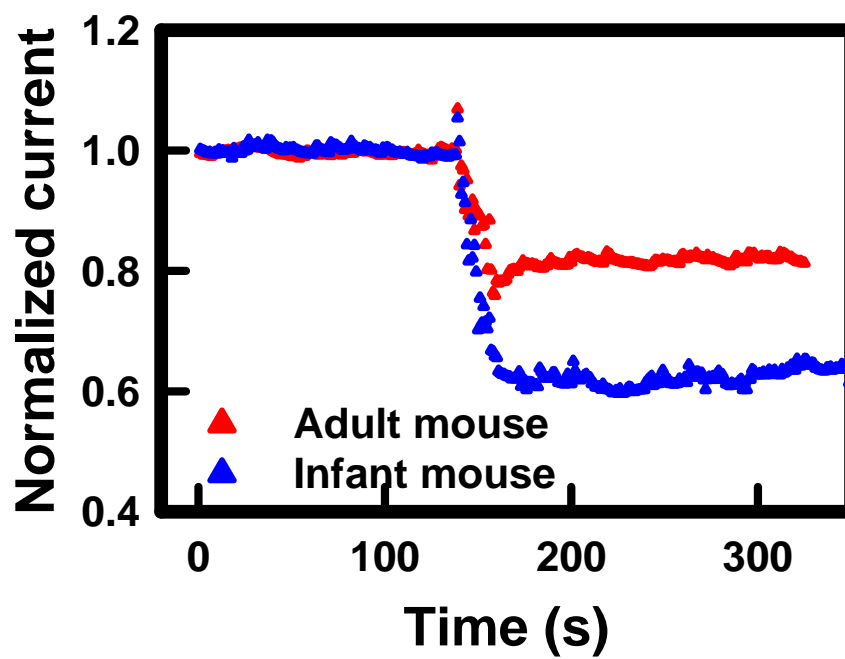


Fig. 4.22 Detection response of AFP concentration from adult and infant mice.

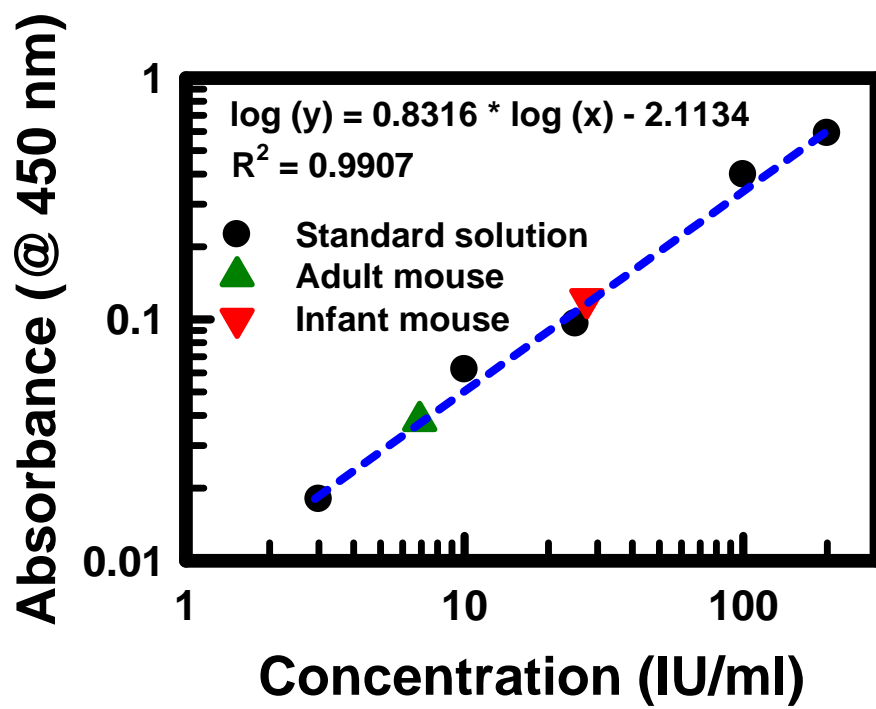


Fig. 4.23 Plot of light absorption with respect to AFP concentration, determined using an ELISA kit.

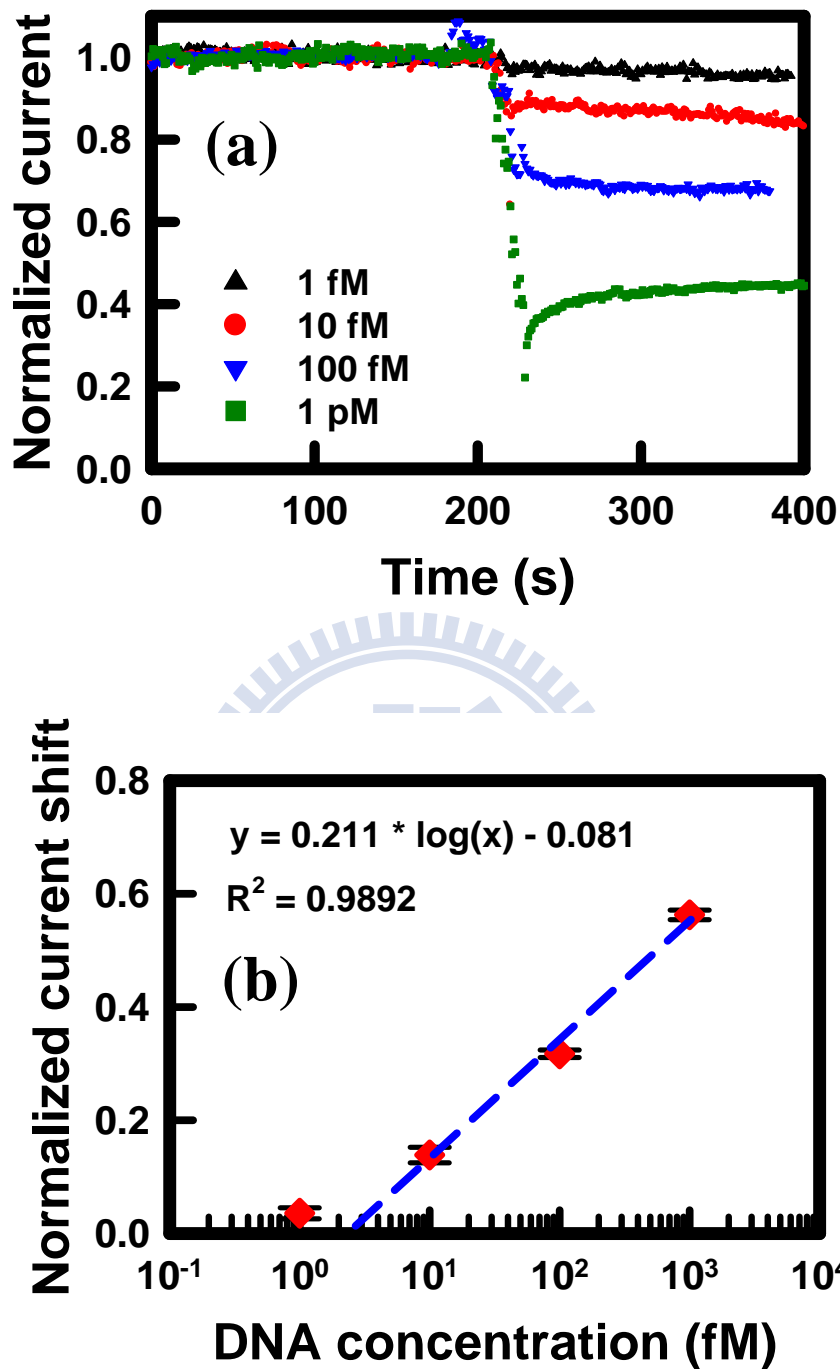


Fig. 4.24 Electrical response of the NB FET sensor toward a 15-mer DNA fragment from HBV. (a) Detection response toward DNA concentrations ranging from 1 fM to 1 pM. (b) Normalized current shift plotted as a function of DNA concentration; the linear range of calibration curve extended from 10 fM to 1 pM.

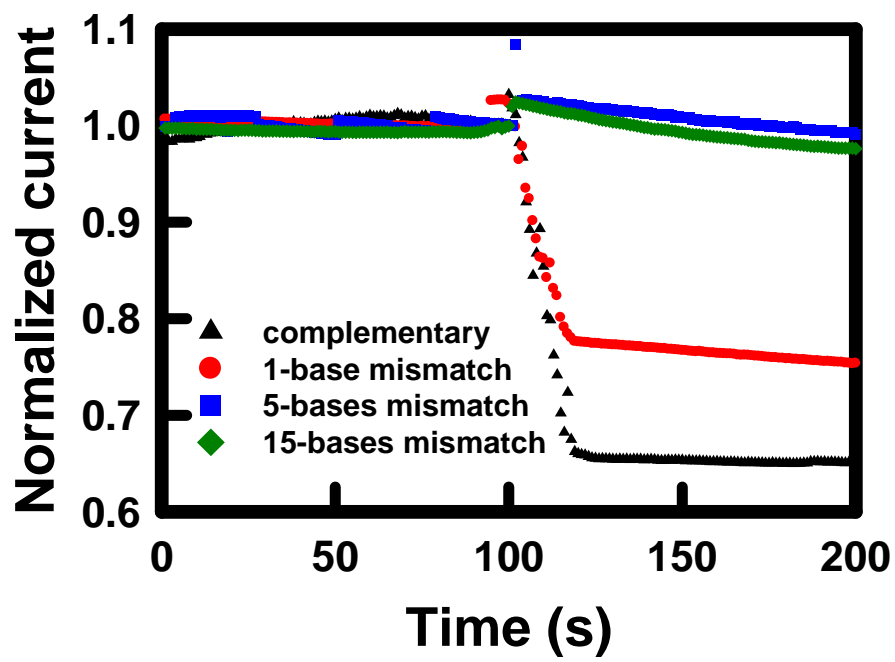


Fig. 4.25 Detection responses toward complementary and one-, five-, and 15-base-mismatched target DNA samples.

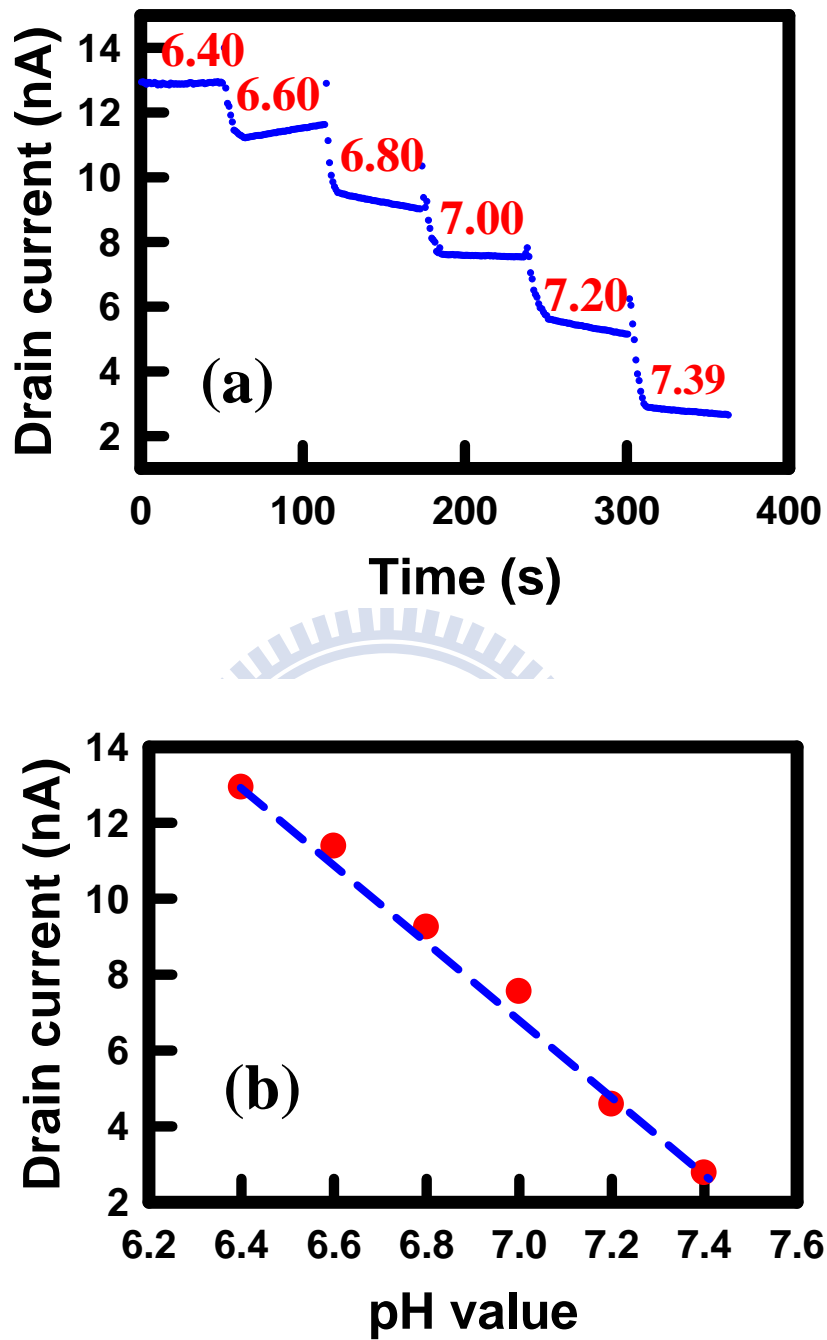


Fig. 4.26 Electrical response of the NB FET sensor toward the solution pH. (a) Detection response at values of pH ranging from 6.40 to 7.39. (b) Drain current plotted as a function of the pH.

Chapter 5

Conclusions and future perspective

9.1 Conclusions

In this thesis, we have investigated the nickel silicide process, NC memory, and NW/NB FET biosensor based on nanotechnology. In chapter 2, the effects of capping layers on formation of Ni-silicided junction was studied. With a Ti-capped layer on Ni-silicided sample, it is shown to exhibit inferior thermal stability than the uncapped and TiN-capped samples. For the silicided junctions, samples with a Ti capping layer are shown to have larger leakage current density. A high-resistivity $\text{Ni}_x\text{Ti}_y\text{Si}_z$ compound layer formed on the NiSi surface for the Ti-capped sample, resulted in the overall silicide thickness and the junction leakage current increased. We also demonstrated the thermal stability and electrical behavior of nickel germano-silicide structures. The insertion of a poly-Si film on poly-SiGe significantly enhances the thermal and morphological stabilities of NiSi films. We have derived a stress-confined grain growth and Ge blocking model to explain the beneficial effects of the poly-Si film and confirm the predictions made after scrutiny of TEM images. The presence of poly-Si films improved the properties of both the thin-film and fine-line NiSi structures.

In chapter 3, we have discussed the NCs formation of the sol-gel spin-coating thin film at different conditions. Together with the TEM images and interfacial energies, we proposed a model to explain the transformation of thin film into NCs. The 900°C annealed NC memory demonstrated the satisfactory retention characteristic than the 600°C annealed sample due to the NC formation. The large V_t shift of the 900°C annealed sample is potential for future multi-bit application. We also investigated the factor of solvent that affected the morphology of NCs. The coated film by ethanol system led to the isolated NCs, while the interconnected NCs morphology was observed in the thicker film by IPA system. The isolated NC memory in ethanol system exhibited better charge trapping performance and larger memory window.

Moreover, we proposed a sol-gel derived NC memory by utilizing the hot hole trapping to program. With the merits of high-density NCs and hot hole trapping, this NC memory exhibited excellent electrical performance in terms of high data retention, exceptional endurance, and high program speed.

In chapter 4, we used a cleaning solution prepared from a mixture of acetone and ethanol to develop an NWFET device that behaved as a biomolecular sensor for an oncogene. The NWFET exhibited n-channel depletion characteristics that allowed detection of the hybridization and de-hybridization of a BRAF^{V599E} mutation gene from a cancer cell, as well as the ability to distinguish between complementary and

mismatched target DNA. The detection limit of the NWFET biosensor for the sensing of the mutation gene was in the sub-femtomolar regime. We also fabricated a novel silicon NB FET by using the LOCOS isolation process and CMOS-compatible technology. The shrunken nanobelts, which had high surface-to-volume ratios, were used to detect HCC. We found that our NB FET biosensor could detect AFP, a biomarker for HCC, at concentrations ranging from 3 to 100 ng/mL, the most critical range for screening HCC. With multiplex detection of AFP, HBV *x* gene, and pH, it may be possible to perform the reliable, real-time determination of HCC at an early stage, while avoiding the problems of false positive identification.

9.2 Future perspective

There are some topics that are suggested for future perspective:

- (1) Development a photo-detector b using NiSi-Si-NiSi multi-segments for biomolecule detection.
- (2) Development of the sol-gel derived NC memory on a flexible substrate.
- (3) Study of RRAM by using sol-gel spin-coating method.
- (4) Development of the NB FET sensor array and measurement technique.
- (5) Development of the logic circuit by NB FET.

References

Chapter 1

1. C. P. Poole and F. J. Owens, Introduction to nanotechnology, John Wiley & Sons, New Jersey, (2003), p. 2.
2. G. M. Whitesides, J. C. Love, Sci. Am., 285 (2001), p. 38.
3. D. Mijatovic, J. C. T. Eijkel and A. van den Berg, Lab Chip, 5 (2005), p. 492.
4. H. V. Jansen, N. R. Tas and J. W. Berenschot, Encyclopedia of Nanoscience and Nanotechnology, ed. H. S. Nalwa, 5 (2004), p. 163.
5. P. Mela, N. R. Tas, A. van den Berg and J. E. ten Elshof, Encyclopedia of Nanoscience and Nanotechnology, ed. H. S. Nalwa, 6 (2004), p. 739.
6. S. A. Gajar and M. W. Geis, J. Electrochem. Soc., 139 (1992), p. 2883.
7. H.zhu, and M.Snyder, Current opinion in chemical biology, 7 (2003), p. 1.
8. R. W. Mann, L. A. Clevenger, P. D. Agnello, and F. R. White, IBM J. Res. Develop., 39 (1995), p. 403.
9. J. Seger, T. Jarmar, Z. B. Zhang, H. H. Radamson, F. Ericson, U. Smith, S. L. Zhang, J. Appl. Phys. 96 (2004), p. 1919.
10. S. Tiwari, F. Rana, K. Chan, H. Hanafi, W. Chan, and D. Buchanan, Tech. Dig. -Int. Electron Devices Meet., (1995), p. 521.
11. E. Kapetanakis, P. Normand, D. Tsoukalas, K. Beltsios, J. Stoemenos, S. Zhang, J. v. d. Berg, Appl. Phys. Lett., 77 (2000), p. 3450.
12. T. Baron, B. Pelissier, L. Perniola, F. Mazen, J. M. Hartmann, G. Rolland, Appl. Phys. Lett., 83 (2003), p. 1444.
13. Z. Liu, C. Lee, V. Narayanan, G. Pei, E. C. Kan, IEEE Trans. Electron Device Lett., 49 (2002), p. 1606.
14. J. Tang, J. Fabbri, R. D. Robinson, Y. Zhu, I. P. Herman, M. L. Steigerwald, L. E. Brus, Chem. Mater., 16 (2004), p. 1336.
15. J. Pitkanen, P. Peterson, Genes Immun. 4 (2003), p. 12.
16. C. Lin, Y. Liu, H. Yan, Nano Lett., 7 (2007), p. 507.
17. A. Gupta, D. Akin, R. Bashir, J. Vac. Sci. Technol. B, 22 (2004), p. 2785.
18. D. Fologea, M. Gershow, B. Ledden, D. S. McNabb, J. A. Golovchenko, J. Li, Nano Lett., 5 (2005), p. 1905.
19. M. A. Lapierre-Devlin, C. L. Asher, B. J. Taft, R. Gasparac, M. A. Roberts, S. O. Kelley, Nano Lett., 5 (2005), p. 1051.
20. O. U. Beg, R. G. Holt, Biotechnol. Appl. Biochem., 26 (1997), p. 27.
21. S. Takenaka, K. Yamashita, M. Takagi, Y. Uto, H. Kondo, Anal. Chem., 72 (2000), p. 1334.

22. R. Bowler, T. J. Davies, M. E. Hyde, R. G. Compton, *Anal. Chem.*, 77 (2005), p. 1916.
23. E. P. Go, J. V. Apon, G. Luo, A. Saghatelian, R. H. Daniels, V. Sahi, R. Dubrow, B. F. Cravatt, A. Vertes, G. Siuzdak, *Anal. Chem.*, 77 (2005), p. 1641.
24. C. E. Gardner, M. A. Ghanem, J. W. Wilson, D. C. Smith, *Anal. Chem.*, 78 (2006), p. 951.
25. Z. Gao, A. Agarwal, A. D. Trigg, N. Singh, C. Fang, C.-H. Tung, Y. Fan, K. D. Buddhharaju, J. Kong, *Anal. Chem.*, 79 (2007), p. 3291.
26. F. Patolsky, B. P. Timko, G. F. Zheng, C. M. Lieber, *MRS Bull.*, 32 (2007), p. 142.
27. F. Patolsky, G. Zheng, C. M. Lieber, *Nat. Protocols*, 1 (2006), p. 1711.
28. F.-H. Ko, Z.-H. Yeh, C.-C. Chen, T.-F. Liu, *J. Vac Sci. Technol. B*, 23 (2005), p. 3000.
29. O. H. Elibol, D. Morissette, D. Akin, J. P. Denton, R. Bashir, *Appl. Phys. Lett.*, 83 (2003), p. 4613.
30. H. Davies, G. R. Bignell, C. Cox, P. Stephens, S. Edkins, S. Clegg, J. Teague, H. Woffendin, M. J. Garnett, W. Bottomley, N. Davis, E. Dicks, R. Ewing, Y. Floyd, K. Gray, S. Hall, R. Hawes, J. Hughes, V. Kosmidou, A. Menzies, C. Mould, A. Parker, C. Stevens, S. Watt, S. Hooper, R. Wilson, H. Jayatilake, B. A. Gusterson, C. Cooper, J. Shipley, D. Hargrave, K. Pritchard.-Jones, N. Maitland, G. Chenevix.-Trench, G. J. Riggins, D. D. Bigner, G. Palmieri, A. Cossu, A. Flanagan, A. Nicholson, J. W. C. Ho, S. Y. Leung, S. T. Yuen, B. L. Weber, H. F. Seigler, T. L. Darrow, H. Paterson, R. Marails, C. J. Marshall, R. Wooster, M. R. Stratton, P. A. Futreal, *Nature*, 417 (2002), p. 949.
31. E. T. Kimura, M. N. Nikiforova, Z. Zhu, J. A. Knauf, Y. E. Nikiforov, J. A. Fagin, *Cancer Res.*, 63 (2003), p. 1454.
32. H. B. El-Serag, A. C. N. Mason, *Engl. J. Med.*, 340 (1999), p. 745.
33. H.-C. Wu, Q. Wang, H.-I. Yang, H. Ahsan, W.-Y. Tsai, L.-Y. Wang, S.-Y. Chen, C.-J. Chen, R. M. Santella, *Cancer Epidemiol. Biomarkers Prev.*, 18 (2009), p. 846.
34. I. Levy, P. D. Greig, S. Gallinger, B. Langer, M. Sherman, *Ann. Surg.*, 234 (2001), p. 206.

Chapter 2

1. C.Y. Chang, S.M. Sze, *ULSI TECHNOLOGY*, McGRAW-HILL, New York (1996) p. 397.

2. C.T. Huang, T.F. Lei, *IEEE Trans. Electron Dev.*, 44 (1997), p. 601.
3. G. Verma, C. Gelatos, S. Talwar, J.C. Bravman, *IEEE Trans. Electron Dev.*, 49 (2002), p. 42.
4. S.K. Saha, R.S. Howell, M.K. Hatalis, *Thin Solid Films*, 347 (1999), p. 278.
5. A. Lauwers, P. Besser, T. Gutt, A. Satta, M. de Potter, R. Lindsay, N. Roelandts, F. Loosen, S. Jin, H. Bender, M. Stucchi, C. Vrancken, B. Deweerdt, K. Maex, *Microelectron. Eng.*, 50 (2000), p. 103.
6. S.-L. Zhang, U. Smith, *J. Vac. Sci. Technol. A* 22 (2004), p. 1361.
7. J.P. Lu, D. Miles, J. Zhao, A. Gurba, Y. Xu, C. Lin, M. Hewson, J. Ruan, L. Tsung, R. Kuan, T. Grider, D. Mercer, C. Montgomery, *Technical Digest of the International Electron Devices Meeting (IEEE 2002)*, p. 371.
8. A. Alberti, C. Bongiorno, F. La Via, C. Spinella, *J. Appl. Phys.*, 94 (2003), p. 231.
9. T.-H. Yang, G. Luo, E.Y. Chang, T.-Y. Yang, H.-C. Tseng, C.-Y. Chang, *IEEE Elec. Dev. Lett.*, 24 (2003), p. 544.
10. Y. Hu, S.P. Tay, *J. Vac. Sci. Technol.*, A 16 (1998), p. 1820.
11. C. Detavernier, R.L. Van Meirhaeghe, F. Cardon, R.A. Donaton, K. Naex, *Microelectron. Eng.*, 50 (2000), p. 125.
12. G.B. Kim, J.S. Kwak, H.K. Baik, S.M. Lee, *J. Vac. Sci. Technol. B* 17 (1999), p. 162.
13. W.L. Tan, K.L. Pey, S.Y.M. Chooi, J.H. Ye, T. Osipowicz, *J. Appl. Phys.*, 91 (2002), p. 2901.
14. R.T. P. Lee, D.Z. Chi, M.Y. Lai, N.L. Yakovlev, S.J. Chua, *J. Electrochem. Soc.*, 151 (2004), p. G642.
15. K. Maex, *Mater. Sci. Eng.*, R11 (1993), p. 53.
16. C. C. Wu, W. F. Wu, P. Y. Su, L. J. Chen, and F. H. Ko, *Microelectron. Eng.* 84 (2007), p. 1801.
17. X. Yu, C. Zhu, and M. Yu, *Appl. Phys. Lett.* 89 (2006), p. 163508.
18. J. Huang, N. Wu, Q. Zhang, C. Zhu, M. F. Li, A. A. O. Tay, Z. Y. Cheng, C. W. Leitz, and A. Lochtefeld, *Appl. Phys. Lett.* 88 (2006), p. 143506.
19. M. Mitsui, K. Arimoto, J. Yamanaka, and K. Nakagawa, *Appl. Phys. Lett.* 89 (2006), p. 192102.
20. J. Seger, T. Jarmar, Z. B. Zhang, H. H. Radamson, F. Ericson, U. Smith, S. L. Zhang, *J. Appl. Phys.* 96 (2004), p. 1919.
21. Y. He, X. L. Liu, J. Y. Feng, and Q. L. Wu, *J. Appl. Phys.* 96 (2004), p. 6928.
22. H. Iwai, T. Ohguro, and S. I. Ohmi, *Microelectron. Eng.* 60 (2002), p. 157.
23. Q. Xiang, C. Woo, E. Paton, J. Foster, B. Yu, and M. R. Lin, *Symp. on VLSI Technol.*, (2000), p. 76..

24. S. L. Zhang, U. Smith, *J. Vac. Sci. Technol. A* 22 (2004), p. 1361.
25. R. W. Mann, G. L. Miles, T. A. Knotts, D. W. Rakowski, L. A. Clevenger, J. M. E. Harper, F. M. d'Heurle, and C. Cabral, Jr., *Appl. Phys. Lett.* 67 (1995), p. 3729.
26. T. Jarmar, J. Seger, F. Ericson, D. Mangelinck, U. Smith, and S.-L. Zhang, *J. Appl. Phys.* 92 (2002), p. 7193.
27. L. J. Chen, J. B. Lai, and C. S. Lee, *Micron* 33 (2002), p. 535.
28. W. W. Wu, S. L. Cheng, S. W. Lee, and L. J. Chen, *J. Vac. Sci. Technol. B* 21 (2003), p. 2147.
29. W. W. Wu, J. H. He, S. L. Cheng, S. W. Lee, and L. J. Chen, *Appl. Phys. Lett.* 83 (2003), p. 1836.
30. W. W. Wu, T. F. Chiang, S. L. Cheng, S. W. Lee, L. J. Chen, Y. H. Peng, and H. H. Cheng, *Appl. Phys. Lett.* 81 (2002), p. 820.
31. P. S. Lee, K. L. Pey, D. Mangelinck, J. Ding, D. Z. Chi, J. Y. Dai, and L. Chan, *J. Electrochem. Soc.* 149 (2002), p. 331.

Chapter 3

1. R. Bez, E. Camerlenghi, A. Modelli, A. Visconti, *Proceedings of the IEEE*, 91 (2003), p. 489.
2. S. Maikap, T. Y. Wang, P. J. Tzeng, C. H. Lin, L. S. Lee, J. R. Yang, and M. J. Tsai, *Appl. Phys. Lett.* 90 (2007), p. 253108.
3. K. S. Seol, S. J. Choi, J. Y. Choi, E.-J. Jang, B.-K. Kim, A.-J. Park, D.-G. Cha, I.-Y. Song, J.-B. Park, and Y. Park, *Appl. Phys. Lett.* 89 (2006), p. 083109.
4. Y. Liu, S. Tang, and S. K. Banerjee, *Appl. Phys. Lett.* 88 (2006), p. 213504.
5. S.-J. Ding, M. Zhang, W. Chen, D. W. Zhang, L.-K. Wang, *Journal of Electronic Materials* 36 (2007), p. 253.
6. S. Tiwari, F. Rana, K. Chan, H. Hanafi, W. Chan, D. Buchanan, *Tech. Dig. – Int. Electron Device Meet* (1995), p. 521.
7. C.-C. Lin, T.-C. Chang, C.-H. Tu, W.-R. Chen, C.-W. Hu, S. M. Sze, T.-Y. Tseng, S.-C. Chen, and J.-Y. Lin, *J. Electrochem. Soc.*, 156 (2009), p. H716.
8. T.-M. Pan and W.-W. Yeh, *J. Vac. Sci. Technol. B*, 27 (2009), p. 700.
9. S.-W. Ryu, C. B. Mo, S. H. Hong, Y.-K. Choi, *IEEE Transactions on Nanotechnology* 7 (2008), p. 145.
10. S. Maikap, P. J. Tzeng, H. Y. Lee, C. C. Wang, T. C. Tien, L. S. Lee, and M.-J. Tsai, *Appl. Phys. Lett.* 91 (2007), p. 043114.

11. T. Muller, K.-H. Heinig, W. Moller, G. Bonafos, H. Coffin, N. Cherkashin, G. B. Assayag, S. Schamm, M. Tence, and C. Colliex, *Appl. Phys. Lett.* 85 (2004), p. 2373.
12. M. She, *Semiconductor Flash Memory Scaling*, University of California, Berkeley (2003).
13. S. Maikap, A. Das, T.-Y. Wang, T.-C. Tien, and L.-B. Chang, *J. Electrochem. Soc.*, 156 (2009), p. K28.
14. C.-C. Lin, T.-C. Chang, C.-H. Tu, W.-R. Chen, L.-W. Feng, S. M. Sze, T.-Y. Tseng, S.-C. Chen, and J.-Y. Lin, *J. Electrochem. Soc.*, 156 (2009), p. H276.
15. T.-M. Pan and T.-Y. Yu, *J. Electrochem. Soc.*, 155 (2008), p. G124.
16. Y. Liu, S. Tang, and S. K. Banerjee, *Appl. Phys. Lett.*, 88 (2006), p. 213504.
17. T. Muller, K.-H. Heinig, W. Moller, G. Bonafos, H. Coffin, N. Cherkashin, G. B. Assayag, S. Schamm, M. Tence, and C. Colliex, *Appl. Phys. Lett.*, 85 (2004), p. 2373.
18. C. Gerardi, B. DeSalvo, S. Lmnbardo, T. Barod, *IEEE International Conference on Integrated Circuit Design and Technology*, (2004).
19. Y.-C. King, T.-J. King, C. Hu, *Tech. Dig. – Int. Electron Device Meet* (1998).
20. Y.-H. Lin, C.-H. Chien, C.-T. Lin, C.-Y. Chang, T.-F. Lei, *IEEE Electron Device Lett.* 26 (2005), p. 154.
21. F.-H. Ko, H.-C. You, C.-M. Chang, W.-L. Yang, and T.-F. Lei, *J. Electrochem. Soc.*, 154 (2007), p. H268.
22. F.-H. Ko, H.-C. You, and T.-F. Lei, *Appl. Phys. Lett.* 89 (2006), p. 252111.
23. M. Gombos, A. Vecchione, D. Zola, P. Tedesco, and S. Pace, *Physica C*, 1141 (2002), p. C372.
24. S. Stemmer, Z. Chen, C. G. Levi, P. S. Lysaght, B. Foran, J. A. Gisby, and J. R. Taylor, *J. J. Appl. Phys.* 42 (2003), p. 3593.
25. T.-M. Pan, W.-H. Shu, *Appl. Phys. Lett.* 91 (2007), p. 172904.
26. W.-R. Chen, T.-C. Chang, P.-T. Liu, J.-L. Yeh, C.-H. Tu, J.-C. Lou, C.-F. Yeh, and C.-Y. Chang, *Appl. Phys. Lett.* 91 (2007), p. 082103.
27. F.-H. Ko, C.-T. Wu, M.-F. Chen, J.-K. Chen, and T.-C. Chu, *Appl. Phys. Lett.* 90 (2007), p. 191901.
28. H.-C. You, T.-H. Hsu, F.-H. Ko, J.-W. Huang, W.-L. Yang, and T.-F. Lei, *IEEE ELECTRON DEVICE LETT.* 27 (2006), p. 635.
29. C.-C. Wu, Y.-J. Tsai, M.-C. Chu, S.-M. Yang, F.-H. Ko, P.-L. Liu, W.-L. Yang, and H.-C. You, *Appl. Phys. Lett.*, 92 (2008), p. 123111.
30. A. G. Khachaturyan, *Theory of structural transformations in solids*, John Wiley and Sons, New York, (1983).

31. M. A. White, S. T. Ochsenein, and D. R. Gamelin, *Chem. Mater.*, 20 (2008), p. 7107.
32. S. Y. Hu, and L. Q. Chen, *Acta Materialia*, 52 (2004), p. 3069.
33. R. G. J. Ball, M. A. Mignanelli, T. I. Barry and J. A. Gisby, *J. Nucl. Mater.*, 201 (1993), p. 128.
34. D. J. Seol, S. Y. Hu, Y. L. Li, J. Shen, K. H. Oh, and L. Q. Chen, *Acta Materialia*, 51 (2003), p. 5173.
35. S. Stemmer, Z. Chen, C. G. Levi, P. S. Lysaght, B. Foran, J. A. Gisby, and J. R. Taylor, *Jpn. J. Appl. Phys.*, 42 (2003), p. 3593.
36. C. H. Tu, T. C. Chang, P. T. Liu, H. C. Liu, S. M. Sze, and C. Y. Chang, *Appl. Phys. Lett.*, 89 (2006), p. 162105.
37. H.-C. You, C.-C. Wu, F.-H. Ko, T.-F. Lei, and W.-L. Yang, *J. Vac. Sci. Technol. B*, 25 (2007), p. 2568.
38. C.-C. Lin, T.-C. Chang, C.-H. Tu, W.-R. Chen, L.-W. Feng, S. M. Sze, T.-Y. Tseng, S.-C. Chen, and J.-Y. Lin, *J. Electrochem. Soc.*, 156 (2009), p. H276.
39. T.-M. Pan and T.-Y. Yu, *J. Electrochem. Soc.*, 155 (2008), p. G124.
40. T. Y Chiang, T. S. Chao, Y. H. Wu, and W. L. Yang, *IEEE Electron Device Lett.*, 29 (2008), p. 1148.
41. S.M. Sze, *Semiconductor devices, physics and technology*. 2nd ed., John Wiley and Sons, New York, (2002).
42. P. H. Tsai, K. S. Chang-Liao, T. C. Liu, T. K. Wang, P. J. Tzeng, C. H. Lin, L. S. Lee, and M. J. Tsai, *IEEE Electron Device Lett.*, 30 (2009), p. 775.
43. T. M. Pan, and W. W. Yeh, *Appl. Phys. Lett.*, 92 (2008), p.173506.
44. D. Shahrjerdi, D. I. Garcia-Gutierrez, and S. K. Banejee, *IEEE Electron Device Lett.*, 28 (2007), p. 793.
45. Y. H. Lin, C. H. Chien, C. T. Lin, C. W. Chan, C. Y. Chang, and T. F. Lei, *IEEE Electron Device Lett.*, 26 (2005), p. 154.
46. F. M. Yang, T. C. Chang, P. T. Liu, P. H. Yeh, Y. C. Yu, J. Y. Lin, S. M. Sze, and J. C. Lou, *Appl. Phys. Lett.*, 90 (2007), p.132102.
47. H. C. You, T. H. Hsu, F. H. Ko, J. W. Huang, W. L. Yang, and T. F. Lei, *IEEE Electron Device Lett.*, 27 (2006), p.653.

Chapter 4

1. T. Sano, C. L. Smith, C. R. Cantor, *Science*, 258 (199), p. 120.
2. L. Tang, G. Zeng, G. Shen, Y. Li, C. Liu, Z. Li, J. Luo, C. Fan, C. Yang, *Biosens. Bioelectron.*, 24 (2009), p. 1474.
3. M. H. Pournaghi-Azar, E. Alipour, S. Zununi, H. Froohandeh, M. S. Hejazi,

- Biosens. Bioelectron., 24 (2008), p. 524.
4. G. J. Zhang, J. H. Chua, R.-E. Chee, A. Agarwal, S. M. Wong, Biosens. Bioelectron., 24 (2009), p. 2504.
 5. Y. Chen, X. Wang, S. Erramilli, P. Mohanty, A. Kalinowski, Appl. Phys. Lett., 89 (2006), p. 223512.
 6. J. Hahn and C. M. Lieber, Nano Lett., 4 (2004), p. 51.
 7. C.-Y. Hsiao, C. H. Lin, C. H. Hung, C. J. Su, Y. R. Lo, C. C. Lee, H. C. Lin, F. H. Ko, T. Y. Huang, Y. S. Yang, Biosens. Bioelectron., 24 (2009), p. 1223.
 8. H.-S. Lee, K. S. Kim, C.-J. Kim, S. K. Hahn, M.-H. Jo, Biosens. Bioelectron., 24 (2009), p. 1801.
 9. C.-H. Lin, C.-H. Hung, C.-Y. Hsiao, H. C. Lin, F.-H. Ko, Y.-S. Yang, Biosens. Bioelectron., 24 (2009), p. 3019.
 10. L.-E. Wernersson, E. Lind, L. Samuelson, T. Lowgren, J. Ohlsson, Jpn. J. Appl. Phys., 46 (2007), p. 2629.
 11. P. H. Rieger, Electrochemistry, Prentice-Hall, New Jersey, (1987), p. 12.
 12. P. R. Nair, M. A. Alam, Nano Lett., 8 (2008), p. 1281.
 13. H. C. Lin, M. H. Lee, C. J. Su, T. Y. Huang, C. C. Lee, Y. S. Yang, IEEE Electron Device Lett., 26 (2005), p. 643.
 14. X. Duan, C. Niu, V. Sahi, J. Chen, J. W. Parce, S. Empedocles, J. L. Goldman, Nature, 425 (2003), p. 274.
 15. Z. Li, Y. Chen, X. Li, T. I. Kamins, K. Nauka, R. S. Williams, Nano Lett., 4 (2004), p. 245.
 16. E. Stern, J. F. Klemic, D. A. Routenberg, P. N. Wyrembak, D. B. Turner.-Evans, A. D. Hamilton, D. A. LaVan, T. M. Fahmy, M. A. Reed, Nature, 445 (2007), p. 519.
 17. H. Davies, G. R. Bignell, C. Cox, P. Stephens, S. Edkins, S. Clegg, J. Teague, H. Woffendin, M. J. Garnett, W. Bottomley, N. Davis, E. Dicks, R. Ewing, Y. Floyd, K. Gray, S. Hall, R. Hawes, J. Hughes, V. Kosmidou, A. Menzies, C. Mould, A. Parker, C. Stevens, S. Watt, S. Hooper, R. Wilson, H. Jayatilake, B. A. Gusterson, C. Cooper, J. Shipley, D. Hargrave, K. Pritchard.-Jones, N. Maitland, G. Chenevix.-Trench, G. J. Riggins, D. D. Bigner, G. Palmieri, A. Cossu, A. Flanagan, A. Nicholson, J. W. C. Ho, S. Y. Leung, S. T. Yuen, B. L. Weber, H. F. Seigler, T. L. Darrow, H. Paterson, R. Marails, C. J. Marshall, R. Wooster, M. R. Stratton, P. A. Futreal, Nature, 417 (2002), p. 949.
 18. X. Xu, R. M. Quiros, P. Gattuso, K. B. Ain, R. A. Prinz, Cancer Res., 63 (2003), p. 4561.
 19. E. T. Kimura, M. N. Nikiforova, Z. Zhu, J. A. Knauf, Y. E. Nikiforov, J. A. Fagin, Cancer Res., 63 (2003), p. 1454.

20. S. Yoshida, H. Kanno, T. Watanabe, *Anal. Sci.*, 11 (1995), p. 251.
21. L. D. Stefano, A. Vitale, I. Rea, M. Staiano, L. Rotiroti, T. Labella, I. Rendina, V. Aurilia, M. Rossi, A. D'Auria, *Extremophiles*, 12 (2008), p. 69.
22. J. Yakovleva, R. Davidsson, A. Lobanova, M. Bengtsson, S. Eremin, T. Laurell, J. Emneus, *Anal. Chem.*, 74 (2002), p. 2994.
23. D. V. Turutin, T. S. Zatsepin, M. A. Timchenko, E. A. Kubareva, T. S. Oretskaya, *Mol. Biol.*, 36 (2002), p. 705.
24. S. M. Sze, *Physics of Semiconductor Devices*, 2nd ed., John Wiley & Sons, New York, (1981), pp. 454–456.
25. E. Stern, R. Wagner, F. J. Sigworth, R. Breaker, T. M. Fahmy, M. A. Reed, *Nano Lett.*, 7 (2007), p. 3405.
26. M. Bras, V. Dugas, F. Bessueille, J. P. Cloarec, J. R. Martin, M. Cabrera, J. P. Chauvet, E. Souteyrand, M. Garrigues, *Biosens. Bioelectron.*, 20 (2004), p. 797.
27. J.-N. Volle, G. Chambon, A. Sayah, C. Reymond, N. Fasel, M. A. M. Gijis, *Biosens. Bioelectron.*, 19 (2003), p. 457.
28. K.-T. Liao, J.-T. Cheng, C.-L. Li, R.-T. Liu, H.-J. Huang, *Biosens. Bioelectron.*, 24 (2009), p. 1899.
29. H. Im, X.-J. Huang, B. Gu, Y.-K. Choi, *Nature nanotech.*, 2 (2007), p. 430.
30. P. Spies, G.-J. Chen, D. Gygax, *Anal. Biochem.*, 382 (2008), p. 35.
31. L. Tang, G. Zeng, G. Shen, Y. Li, C. Liu, Z. Li, J. Luo, C. Fan, C. Yang, *Biosens. Bioelectron.*, 24 (2009), p. 1474.
32. G. Zheng, F. Patolsky, Y. Cui, W. U. Wang, C. M. Lieber, *Nature Biotech.*, 23 (2005), p. 1294.
33. M. J. Heller, *Annu. Rev. Biomed. Eng.*, 4 (2002), p. 129.
34. H.-K. Liao, C.-L. Wu, J.-C. Chou, W.-Y. Chung, T.-P. Sun, S.-K. Hsiung, *Sens. Actuators, B* 61 (1999), p. 1.
35. L. L. Chi, J. C. Chou, W. Y. Chung, T. P. Sun, S. K. Hsiung, *Mater. Chem. Phys.*, 63 (2000), p. 19.
36. X. Tang, S. Bansaruntip, N. Nakayama, E. Yenilmez, Y.-I. Chang, Q. Wang, *Nano Lett.*, 6 (2006), p. 1632.
37. F. Patolsky, G. Zheng, C. M. Lieber, *Nature Protocols*, 1 (2006), p. 1711.
38. Y. Cheng, P. Xiong, C. S. Yun, G. F. Strouse, J. P. Zheng, R. S. Yang, Z. L. Wang, *Nano Lett.*, 8 (2008), p. 4179.
39. H. Pan, Y.-P. Feng, *ACS Nano*, 2 (2008), p. 2410.
40. H. C. Lin, M. H. Lee, C. J. Su, T. Y. Huang, C. C. Lee, Y. S. Yang, *IEEE Electron Device Lett.*, 26 (2005), p. 643.
41. Y. Wu, Y. Cui, L. Huynh, C. J. Barrelet, D. C. Bell, C. M. Lieber, *Nano Lett.*, 4 (2004), p. 433.

42. Z. Li, Y. Chen, X. Li, T. I. Kamins, K. Nauka, R. S. Williams, *Nano Lett.*, 4 (2004), p. 245.
43. C.-Y. Hsiao, C.-H. Lin, C.-H. Hung, C.-J. Su, Y.-R. Lo, C.-C. Lee, H.-C. Lin, F.-H. Ko, T.-Y. Huang, Y.-S. Yang, *Biosens. Bioelectron.*, 24 (2009), p. 1223.
44. C.-H. Lin, C.-Y. Hsiao, C.-H. Hung, Y.-R. Lo, C.-C. Lee, C.-J. Su, H.-C. Lin, F.-H. Ko, T.-Y. Huang, Y.-S. Yang, *Chem. Commun.*, (2008), p. 5749.
45. C.-H. Lin, C.-H. Hung, C.-Y. Hsiao, H.-C. Lin, F.-H. Ko, Y.-S. Yang, *Biosens. Bioelectron.*, 24 (2009), p. 3019.
46. C. Y. Chang, S. M. Sze, in *ULSI Technology*, McGraw-Hill, New York, (1996), pp. 477–479.
47. F. Patolsky, C. M. Lieber, *Mater. Today*, 8 (2005), p. 20.
48. F. Patolsky, G. Zheng, C. M. Lieber, *Anal. Chem.*, 78 (2006), p. 4260.
49. H. B. El-Serag, A. C. N. Mason, *Engl. J. Med.*, 340 (1999), p. 745.
50. H.-C. Wu, Q. Wang, H.-I. Yang, H. Ahsan, W.-Y. Tsai, L.-Y. Wang, S.-Y. Chen, C.-J. Chen, R. M. Santella, *Cancer Epidemiol. Biomarkers Prev.*, 18 (2009), p. 846.
51. J. M. Llovet, J. Bruix, G. J. Gores, *Hepatology*, 31 (2003), p. 1019.
52. F. Yao, J.-M. Cuo, C.-F. Xu, Y.-L. Lou, B.-X. Xiao, W.-H. Zhou, J. Chen, Y.-R. Hu, Z. Liu, G.-F. Hong, *Clin. Chim. Acta*, 361 (2005), p. 119.
53. Levy, P. D. Greig, S. Gallinger, B. Langer, M. Sherman, *Ann. Surg.*, 234 (2001), p. 206.
54. C. Zhang, Z. Li, Y. Cheng, F. Jia, R. Li, M. Wu, K. Li, L. Wei, *Clin. Cancer Res.*, 13 (2007), p. 944.
55. T. Yamashita, M. Forgues, W. Wang, J. W. Kim, Q. Ye, H. Jia, A. Budhu, K. A. Zanetti, Y. Chen, L.-X. Qin, Z.-Y. Tang, X. W. Wang, *Cancer Res.*, 68 (2008), p. 1451.
56. B. P. Timko, T. Cohen-Karni, G. Yu, Q. Qing, B. Tian, C. M. Lieber, *Nano Lett.*, 9 (2009), p. 914.
57. E. Stern, J. F. Klemic, D. A. Routenberg, P. N. Wyrembak, D. B. Turner-Evans, A. D. Hamilton, D. A. LaVan, T. M. Fahmy, M. A. Reed, *Nature*, 445 (2007), p. 519.
58. F. V. Schiodt, G. Ostapowicz, N. Murray, R. Satyanarana, A. Zamzn, S. Munoz, W. M. Lee, *Liver Transpl.*, 12 (2006), p. 1776.
59. The molecular weight of AFP is ca. 65,000–70,000 Da (Y.-M. Liu, H.-B. Mu, Y.-L. Zheng, C.-Q. Wang, Y.-H. Chen, F.-R. Li, J.-H. Wang, J.-K. Cheng, *J. Chromatogr.*, B855 (2007), p. 280). Therefore, concentrations of 3 and 600 ng mL⁻¹ corresponded to 45 pM and 9 nM, respectively.
60. S. Yachnin, R. Hsu, R. L. Heinrikson, J. B. Miller, *Biochim. Biophys. Acta*, 493

- (1977), p. 418.
62. The units of AFP concentration used in ELISA are IU mL⁻¹, which can be transformed to ng mL⁻¹ by multiplying by a constant of 0.917 (D. B. Everman, C. Shuman, B. Dzolganovski, M. A. O’Riordan, R. Weksberg, N. H. Robin, J. Pediatr., 137 (2000), p. 123). By fitting the calibration curve, the concentrations obtained from ELISA analyses were 28.1 and 6.9 IU mL⁻¹, or 25.8 and 6.3 ng mL⁻¹, respectively, for the infant and adult mice, respectively.
 63. M. De Ioris, L. Brugieres, A. Zimmermann, J. Keeling, P. Brock, R. Maibach, J. Pritchard, L. Shafford, J. Zsiros, P. Czaudzerna, G. Perilongo, Eur. J. Cancer, 44 (2008), p. 545.
 64. M.-H. Chang, Semin. Fetal Neonatal Med., 12 (2007), p. 160.
 65. D. Schweinitz, H. Hecker, G. S. Arndt, D. Harm, Int. J. Cancer, 74 (1997), p. 593.
 66. P. Zhu, D. Tan, Z. Peng, F. Liu, L. Song, Acta Biochim. Biophys. Sin., 39 (2007), p. 265.
 67. S.-J. Zhang, H.-Y. Chen, Z.-X. Chen, X.-Z. Wang, World J. Gastroenterol., 11 (2005), p. 4351.
 68. R. Muroyama, N. Kato, H. Yoshida, M. Otsuka, M. Moriyama, Y. Wang, R.-X. Shao, N. Dharel, Y. Tanaka, M. Ohta, R. Tateishi, S. Shiina, M. Tatsukawa, K. Fukai, F. Imazeki, O. Yokosuka, Y. Shiratori, M. Omata, J. Hepatology, 45 (2006), p. 805. The molecular weight of the 15-mer target DNA employed in our experiment was 4914 Da. Hence, concentrations of 1 fM and 1 pM corresponded to 4.9 fg mL⁻¹ and 4.9 pg mL⁻¹, respectively.
 69. J. Hahm, C. M. Lieber, Nano Lett., 4 (2004), p. 51.
 70. D. L. Nelson, M. M. Cox, in Lehninger Principles of Biochemistry, 4th revised ed., W. H. Freeman, New York, (2004), pp. 395–397.
 71. J. S. Campbell, S. D. Hughes, D. G. Gilbertson, T. E. Palmer, M. S. Holdren, A. C. Haran, M. M. Odell, R. L. Bauer, H.-P. Ren, H. S. Haugen, M. M. Yeh, N. Fausto, Proc. Natl. Acad. Sci. USA, 102 (2005), p. 3389.
 72. B. S. Kang, H. T. Wang, F. Ren, B. P. Gila, C. R. Abernathy, S. J. Pearton, J. W. Johnson, P. Rajagopal, J. C. Roberts, E. L. Piner, K. J. Linthicum, Appl. Phys. Lett., 91 (2007), p. 012110.
 73. Y. Cui, Q. Wei, H. Park, C. M. Lieber, Science, 293 (2001), p. 1289.